# Pre-osteoblastic Cell Response on Porous Ceramic Biomaterials and Nanoparticles for Bone Regeneration

by

CHRYSTALLENI HADJICHARALAMBOUS

This dissertation is submitted to the
UNIVERSITY OF CRETE
for the degree of
DOCTOR OF PHILOSOPHY

Department of Materials Science & Technology
Heraklion, Greece

JUNE 2015

# Pre-osteoblastic Cell Response on Porous Ceramic Biomaterials and Nanoparticles for Bone Regeneration

by

CHRYSTALLENI HADJICHARALAMBOUS

This dissertation is submitted to the
UNIVERSITY OF CRETE
for the degree of
DOCTOR OF PHILOSOPHY

Department of Materials Science & Technology
Heraklion, Greece

JUNE 2015

# Pre-osteoblastic Cell Response on Porous Ceramic Biomaterials and Nanoparticles for Bone Regeneration

This dissertation is submitted to the
UNIVERSITY OF CRETE
for the degree of
DOCTOR OF PHILOSOPHY

| | |
|---|---|
| Thesis author | Chrystalleni Hadjicharalambous |
| Supervisor | Prof. Maria Chatzinikolaidou |
| Thesis committee | Prof. M. Chatzinikolaidou<br>Prof. A. Mitraki<br>Prof. M. Vamvakaki<br>Prof. S. Kulkov<br>Prof. G. Chalepakis<br>Prof. C. Pontikoglou<br>Prof. K. Alpantaki |

Department of Materials Science & Technology
Heraklion, Greece

*Dedicated to Maria, Danae &*
*Nefelie.*

*"It always seems impossible*
*until it's done"*
*– Nelson Madela*

# Summary

Due to common bone defects arising from trauma, tumors, infection or bone diseases, techniques to replace, restore, or regenerate bone have become a major clinical challenge [1]. Ceramic biomaterials (calcium phosphates, zirconia, and alumina) hold a prominent position among the strategies employed to address bone repair, while undergoing a continuous evolution to improve both mechanical and biological properties.

Dense zirconia ($ZrO_2$) and alumina ($Al_2O_3$) based ceramics are widely used for load-bearing applications in bone repair due to their excellent mechanical properties and biocompatibility. Unfortunately, they are often regarded as 'bioinert' materials since no direct bone-material interface is created, which is crucial for implant fixation [2]. However, improved bone integration and long-term stability of the implant, may be achieved by facilitating the initial attachment of osteoblast precursor cells to orthopedic implant surfaces and several studies using diverse materials have demonstrated the importance of surface properties into this matter [3]. In this regard, the introduction of a porous structure is believed to enhance cell migration and proliferation thus enabling bone tissue growth and implant stability, but **the biological properties of macroporous (pore size > 50 nm) zirconia and alumina ceramics remain largely unexplored**. Therefore, investigating interactions between cells and porous ceramics through *in vitro* experimentation, is of great interest, as it may lead to identifying beneficial characteristics for improved biological behavior [4]. Taking into consideration the inherent strong mechanical properties of alumina and zirconia, their porous counterparts may be interesting as scaffolds for load bearing segmental bone defects.

Also, among ceramic biomaterials, calcium phosphates constitute a major class of compounds for synthetic bone substitution materials, due to their chemical similarity to the inorganic matrix of bone. During the last decade, inorganic **nanoparticles based on calcium phosphate are emerging as new bone substitution materials that can be used as growth factor gene delivery systems, promoting the process of bone regeneration locally** [5, 6]. Currently, bone morphogenetic proteins are clinically used for the treatment of long-bone fractures, but their delivery needs improvement. Gene transfer is an improved way of delivering such growth factors, as it is possible to achieve high concentrations locally for an extended period of time.

Consequently, suitable ceramic scaffolds with improved mechanical and biological characteristics, in combination with a bone morphogenetic growth factor delivery system, are integral parts of the strategy to heal large defects in load bearing sites [7].

Since zirconia and alumina ceramics are promising biomaterials for bone regeneration, we first investigated the effect of porosity on cell adhesion and proliferation (Chapter 3). The results from this part of the study indicated that highly porous ceramics exhibit better cell behavior compared to low porosity ceramics and this effect was more pronounced among zirconia rather than alumina ceramics. Therefore we focused on the investigation of the pre-osteoblastic osteogenic response employing highly porous zirconia, alumina as well as their zirconia-alumina composite (Chapter 4). We showed that the zirconia-containing ceramics supported a more pronounced cell response, compared to alumina. To further investigate the effect of chemical composition on cell response, we focused on two formulations of zirconia ceramics, namely the yttria- and the magnesia- stabilized zirconia, and investigated the pre-osteoblastic cell adhesion, proliferation and osteogenic potential on them (Chapter 5). Overall in this thesis, eight ceramic scaffolds of different composition and chemistry were employed, and the biological investigation was carried out using MC3T3-E1 pre-osteoblastic cells and focused on the cell adhesion, proliferation and differentiation potential of the cells within the scaffolds. **The objective was to identify beneficial characteristics of porosity and chemistry for improved biological behavior in these new porous alumina and zirconia scaffolds, which possessed strong mechanical properties similar to cortical bone. Furthermore, the potential of calcium phosphate nanoparticles functionalized with plasmid DNA encoding for bone morphogenetic protein 7 (BMP-7), as a suitable gene delivery system for pre-osteoblasts was investigated.** The investigation focused on transfection efficiency and the induction of a subsequence osteogenic response (Chapter 6).

More specifically, an introduction in bone biology and biomaterial properties is given in Chapter 1. Ceramic biomaterials as well as recent advances of nanoparticles for bone applications are reviewed with emphasis on the materials used in this thesis.
In Chapter 2, the experimental procedures for the *in vitro* biological investigation are described. Information is given on method principle and experimental steps taken for the optimization of various bioanalytical, molecular biology, and microscopic methods used in this study.

Chapters 3, 4 and 5 describe and discuss results on the *in vitro* investigation onto porous alumina and zirconia ceramics. Specifically, Chapter 3 presents and discusses results on the **effect of substrate porosity to the attachment and proliferation of pre-osteoblastic MC3T3-E1 cells on zirconia or alumina ceramics using three porosities** for each composition. Cell proliferation was measured by assessing the cellular metabolic activity whereas Scanning Electron Microscopy (SEM) and fluorescence microscopy were employed to qualitatively support the results and evaluate cell morphology. Cell adhesion and metabolic activity was found comparable among low porosity zirconia or alumina ceramics. As porosity increased, cell response to alumina ceramics was found unaffected. In contrast, cell response to zirconia ceramics was sensitive to changes in porosity, and higher porosity favored better cell spreading and growth, consequently leading to the formation of a uniform extracellular matrix as observed by SEM. Therefore, between the highest porosity materials in this study, cell response on zirconia (50% porosity) was found superior to alumina (61% porosity). **Results showed that an average pore size of ~150 µm and 50% porosity can be considered beneficial to cellular growth on zirconia ceramics**.

In Chapter 4, we focused on ceramics of similar high porosity but different composition; alumina (61% porosity), zirconia (50% porosity) and a composite material synthesized of 80% zirconia-20% alumina (60% porosity). We performed *in vitro* cell-material investigations comparing the adhesion, longer term proliferation (up to 21 days) and differentiation of mouse pre-osteoblasts MC3T3-E1 on the materials. While all three ceramics demonstrate a strong cell attachment, better cell spreading was evidently observed on zirconia-containing substrates. Significantly higher cell growth was quantified on the latter ceramics, revealing an increased alkaline phosphatase activity, higher collagen production and increased calcium mineralization compared to alumina. Hence, these **porous zirconia-containing ceramics elicit superior biological responses over porous alumina of similar porosity**, promoting not only enhanced cell proliferation but also differentiation.

Since two different formulations of zirconia ceramics, namely yttria stabilized zirconia (YSZ) and magnesia stabilized zirconia (MgSZ) are often used in biomedical applications, we investigated potential differences between cell response in porous YSZ and MgSZ in terms of growth and osteogenic response, including gene expression of key osteogenic markers. As presented in Chapter 5, MC3T3-E1 pre-osteoblasts were used to investigate the proliferation, alkaline phosphatase (ALP) activity, collagen secretion and expression profile of four genes involved in bone metabolism of cells on porous ceramics. Scanning electron microscopy and fluorescence microscopy were employed to visualize cell morphology and growth. Pre-osteoblasts adhered well on both ceramics but cell numbers on YSZ were higher. Cells exhibited an increase in ALP activity and collagen deposition after 14 days on both MgSZ and YSZ, with higher levels on YSZ. Real-time quantitative polymerase chain reaction (qPCR) was used to investigate gene expression of osteogenic markers. **Results showed that the expression of bone sialoprotein (*Bsp*) and collagen type I (*col1a1*) were significantly higher on YSZ**. No significant differences were found in their ability to regulate the early gene expression of *Runx2* and *Alp*. Nevertheless, the biomineralized calcium content was similar on both ceramics after 21 days, indicating that **despite chemical differences, both scaffolds direct the pre-osteoblasts towards a mature state capable of mineralizing the extracellular matrix**.

Finally, Chapter 6 concerns with calcium phosphate (CaP) nanoparticles (NPs) and their potential to transfect pre-osteoblastic cells and trigger an osteogenic response via the secretion of hBMP-7. Polyethylenimine-stabilized calcium phosphate nanoparticles loaded with plasmid DNA, which encodes either for bone morphogenetic protein 7 (BMP-7) or for enhanced green fluorescent protein (EGFP) were employed. They were used for the transfection of the pre-osteoblastic cells MC3T3-E1 and showed high transfection efficiency (25%) together with low cytotoxicity. Their potential to induce an osteogenic response by transfection was demonstrated by measuring ALP activity and calcium deposition. The expression of the osteogenic markers *Alp*, *Runx2*, *Col1a1* and *Bsp* was investigated by means of real-time quantitative polymerase chain reaction (qPCR). It was shown that **phBMP-7-loaded nanoparticles can provide a means of transient transfection and localized production of BMP-7 in MC3T3-E1 cells, with a subsequent increase of two osteogenic markers**, specifically alkaline phosphatase activity and calcium matrix bio-mineralization.

In conclusion, this PhD work highlights the potential of macroporous alumina and zirconia to be used in bone repair as non-degradable scaffolds of high mechanical strength. The results bring out differences in the pre-osteoblastic cell response arising from varying porosity or chemistry that would be valuable for future *in vivo* studies.

Also in this study, calcium phosphate nanoparticles are revealed as a non-toxic system for the delivery of nucleic acids in pre-osteoblasts with the ability to induce temporary synthesis of BMP-7 and the potential for a subsequent osteogenic response. The system showed good transfection efficiency and appears promising for future *in vivo* studies. Successful application of nucleic acid delivery for bone regeneration would be a major breakthrough in modern medicine.

# Acknowledgements

My sincerest thanks go to Prof. Maria Chatzinikolaidou for giving me the opportunity to work in her group on the very interesting field of bone biomaterials and osteogenesis research. As one of the very first members of the group, I greatly appreciate the confidence and trust that she has placed in me throughout this thesis, from the development of experimental assays, the handling of samples to experimental planning and execution. Her guidance, encouragement and motivation were indispensable for the completion of my thesis.

For this PhD work, I was fortunate enough to have collaborations with two different research groups who provided the biomaterial samples as well as expert advice. Thank you to Prof. Sergei Kulkov and his group from the Department of Mechanics of Deformed Solids, Tomsk State University, Russia for providing and characterizing the alumina and zirconia ceramic samples. This thesis would not have been possible without their contributions.

Thank you also to Prof. Matthias Epple and his group from the Center for Nanointegration Duisburg-Essen (CeNIDE), University of Duisburg-Essen, Germany, for providing the calcium phosphate nanoparticles. Special thanks to Dr. Viktoriya Sokolova and Dr. Diana Kozlova for the many useful discussions and valuable advice especially regarding the handling of the nanoparticles. I would also like to thank Dr. Oleg Prymark, not only for his contribution during discussions regarding the nanoparticles experiments, but also for his interest and work on the characterization of ceramics, which was a very important aspect in the completion of this investigation.

Then I would like to thank Prof. Anna Mitraki and Assoc. Prof. Maria Vamvakaki, my co-supervisors, for their support and valuable advice throughout this thesis as well as for the use of several of the instruments in their lab.

It would be impossible not to thank Dr. Nadia Katsarou for her expert advice on the setting up of real-time qPCR and the many hours we spent together discussing and troubleshooting experiments. Her contribution was invaluable in the completion of this thesis. Thanks are also due to Prof. J. Vondas and Prof. K. Kalantidis and their groups at the Biology Department, University of Crete, for the use of several of their instruments.

I also greatly acknowledge the contributions of the members of the SEM facility of the Biology Department, and especially Mrs. Alexandra Siakouli for expert assistance with SEM and the use of the fluorescence microscope.

I am grateful that Prof. K. Alpantaki, Prof. G. Chalepakis and Prof. C. Pontikoglou accepted to be members of my thesis committee.

A big thank you also goes to all former and current members of the Biomaterials Lab for all the scientific and non-scientific discussions and the time we spent together. Special thanks to Evi Mygdali for her important contributions, especially in the setting up of qPCR, which I greatly acknowledge.

Finally, I would like to thank my family and friends for being there for me during this long journey!

# Table of Contents

# List of Figures

# List of Tables

# Chapter 1

# 1 Introduction

## 1.1 Bone structure and composition

The adult skeleton has 206 bones which vary in size, shape, composition and physiological role. Bones provide structural support and protection for vital organs, and create an environment for marrow. In addition, bones play a pivotal role in mineral homeostasis, principally of calcium and phosphate ions, but also of sodium and magnesium. There are two types of mineralized osseous tissue or mature bone tissue: cancellous and cortical [1]. Other types of tissue are also found in bones and these include marrow, endosteum, periosteum, nerves, blood vessels and cartilage.

**Cancellous** or **trabecular** bone is found in the marrow space (medullary cavity) of a bone, and is principally an irregular open cell porous network with a sponge-like appearance. The porous structure of cancellous bone makes the overall bone lighter and allows space for bone marrow and blood vessels. Its intricate mesh forms the interior scaffold that helps bone to maintain its shape when exposed to compressive forces. Within its porous structure are **bone marrow stem cells**, essential for the growth of new connective tissue (e.g. in muscle, cartilage, bone and tendons) and hematopoietic stem cells that give rise to red blood cells and white blood cells. Cancellous bone accounts for

20% of total bone mass but has nearly ten times the surface area of compact bone. Varying proportions of space to bone are found in different bones according to the need for strength or flexibility [8].

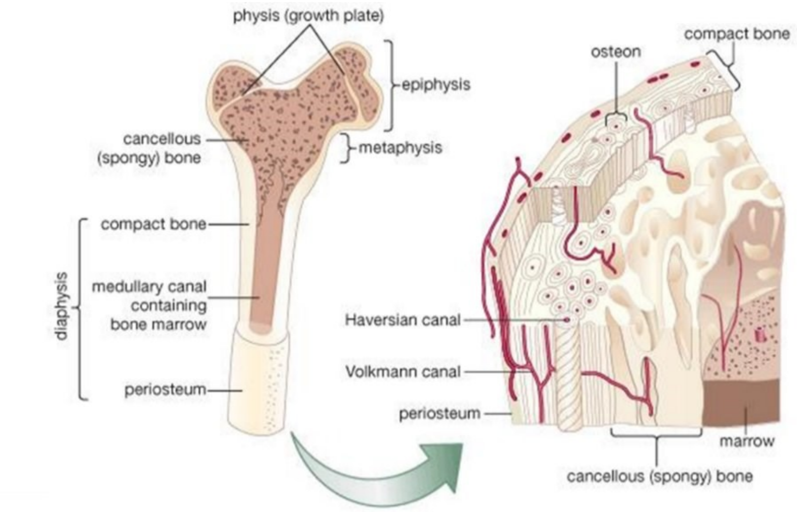

**Figure 1.1. Schematic representation of bone structure.**
Internal structure of a human long bone, with a magnified cross section of the interior. Retrieved from: <http://www.britannica.com/EBchecked/media/66017/Internal-structure-of-a-human-long-bone-with-a-magnified>

Through the action of osteoblasts, new bone matrix is deposited in layers around the trabeculae of cancellous bone, filling the spaces between them until dense bone is formed. Eventually, the bony matrix is solidly filled with organic substance and inorganic salts, leaving only tiny spaces (lacunae) that contain the osteocytes (bone cells). This dense bone is the **cortical** (compact) bone, which makes up 80 percent of the human skeleton. The hard outer layer of cortical bone surrounds cancellous bone, thus giving the bone shape and form. In bones that are principally load bearing, e.g. the femur, the cortical component of the bone is markedly thickened to form a strong shaft [1]. Cortical bone is covered by a periosteum on its outer surface, and an endosteum on its inner surface, which is the boundary between the cortical bone and the cancellous bone (Figure 1.1).

**Bone mineral and matrix:** Bone is a complex, heterogeneous and highly organized mineralized tissue. It consists of cells embedded in an ever-changing mineralized extracellular matrix. Bone composition is often discussed in terms of its chemical constituents and their distributions in the matrix. The amount and characteristics of these constituents change with age, gender, ethnicity, site, disease and drug treatment and define the properties of bone [9].

Bone consists of a mineral phase, whose main constituent is hydroxyapatite ($Ca_{10}(PO_4)_6(OH)_2$), an organic phase (~90% collagen, ~5% non-collagenous proteins and ~2% lipids by weight) and water. The mineral content of bone ranges from 30-98% per dry weight, but most bones have ~60-70% mineral/dry weight depending upon site, species and development. Unlike geological hydroxyapatite in which the molar ration of Ca:P is 1.67, the exact composition in bone may change over time with nutrition, and trace minerals such as magnesium, sodium, potassium and carbonate are also found [9].

The strength of bones depends on the volume of bone matrix and the micro architectural distribution of this volume. In recent years was also recognized that the degree of mineralization of bone tissue (DMB) is an important determinant of bone strength and it influences the mechanical resistance of bones as well as the bone mineral density (BMD) [10].

Collagen, predominantly type I, accounts for the majority of the organic extracellular matrix. Type I collagen is a unique triple helical molecule with the characteristic repeat of glycine-X-Y residues. It consists of two identical and one different amino-acid chains, which are often hydroxylated and glycosylated thus giving rise to a unique crosslinking ability, making the collagen lattice ideal for its functions: providing elasticity to the tissues, stabilizing the extracellular matrix, supporting or templating initial mineral deposition and binding other macromolecules.

Other non-collagenous proteins (NCPs), account for ~5% of the total bone weight. Generally, proteins in the extracellular bone matrix can be divided as: (a) structural proteins (collagen and fibronectin) and (b) proteins with specialized functions, such as regulation of collagen fibril diameter, signaling molecules, growth factors e.g. bone morphogenetic proteins (BMPs), enzymes and proteins with other functions. Today, using proteomics and gene expression profiling, it is known that there are thousands of proteins in the bone matrix, but most are yet to be identified and their functions determined [9].

**Bone cells:** Cortical and cancellous bone is created and re-created by the remodeling action of the two types of bone cells, the osteoblasts and osteoclasts, which have opposite actions and are influenced by numerous factors [11].

**Osteoblasts** are bone forming cells, which are differentiated from mesenchymal stem cells present in bone marrow. They are typically cuboidal and flat in their morphology and are around 20 µm in diameter [3]. Osteoblasts secrete collagen fibrils and other extracellular matrix components forming an unmineralized matrix (osteoid), which they then mineralize with hydroxyapatite crystals to form bone [4]. Osteoblasts become completely embedded in the bone they produce and are then called **osteocytes**, which are no longer able to actively form bone.

**Osteoclasts** are bone resorbing cells, derived from the hematopoietic monocytic cell lineage, which during activity, rest directly on the surface subjected to resorption. The receptor activator of NF-κB (RANK)-RANK ligand (RANKL) mechanism is essential for the differentiation and activation of osteoclasts [12]. They resorb areas of woven bone, which allows it to be remodeled into a highly organized framework of parallel running fibers, orientated in alternate directions dependent on the forces applied to the bone. The harmonized orchestration of osteoblasts and osteoclasts maintains a balance between bone formation and bone resorption, which allows repair of damaged tissue, the adaptation of bone structure to altered loading conditions, as well as control of calcium and phosphate homeostasis [11].

## 1.2 Bone healing and the clinical necessity of biomaterials

Bone has a considerable ability to regenerate following injury and the regenerated bone may be indistinguishable from normal healthy bone. *Osteogenesis*, the formation of bone tissue, is strongly stimulated in injuries such as fractures. It is an active process initiated by mesenchymal stem cells (MSCs) and is tightly regulated to ultimately generate normal vascularized bone structure [13, 14].

Despite its complexity, the process of bone healing occurs in three distinct but overlapping phases: the early inflammatory phase, the repair phase and the remodeling phase. Following an injury, bleeding from adjacent structures causes a hematoma to form around the broken bone ends. This is the early inflammatory phase. Inflammatory cells (macrophages, monocytes, lymphocytes, and polymorphonuclear cells) and fibroblasts enter the site under prostaglandin mediation. Fibroblasts lay down *granulation tissue*, which is composed predominantly of type III collagen. At the same time, ingrowth of vascular tissue, and migration of mesenchymal cells takes place. During the reparative phase, chondroblasts arise from the periosteum at the proximal bone end and produce hyaline cartilage. At the distal bone end, osteoblasts arise from the periosteum and produce woven bone (mainly type I collagen). The fibroblasts within the granulation tissue develop into chondroblasts which also form hyaline cartilage. The two tissues of hyaline cartilage and woven bone form the *fracture callus*, which grows in size to bridge the fracture gap and restore some of the original bone strength. The woven bone followed by the hyaline cartilage are both replaced with lamellar bone in a process known as *bony substitution* and *endochondral ossification* for the two tissues respectively. The lamellar bone begins forming soon after the collagen matrix of either tissue becomes mineralized. At this point, the mineralized matrix is penetrated by osteoblasts and vascular channels which lay down stronger trabecular bone. The final phase is bone remodeling, which is completed by the substitution of trabecular bone by *cortical bone*, in a process where deposition of cortical bone by osteoblasts occurs in resorption pits prepared by osteoclasts [1, 13, 14].

In most clinical situations the healing process can be easily managed with some form of internal or external support. However, a major challenge for today's medicine is the functional restoration of large skeletal bone defects resulting from **trauma** or **bone disease such as osteoporosis, arthritis and cancer**. The biggest problem created by bone disease, especially osteoporosis, is **fractures**, which may be the first visible sign of disease in patients. As an example, over one million fractures occur each year in the United Kingdom, of which 5% to 10% are considered to have problems in healing [15]. In these situations usually a "critical size defect" is identified, which refers to the smallest size intraosseous wound that does not spontaneously heal, but in practice it is rather difficult to define [13]. Osteoporosis and particularly hip fractures have a large economic impact; the direct costs of osteoporotic fractures in the USA in 2005 were estimated to be $19 billion. More than 10 million adults older than 50 years are estimated to have osteoporosis in the USA [16]. In Norway, the incidence of long bone fractures requiring in-hospital treatment for both male and female according to age was studied, showing higher frequency in the senior population [17]. Elsewhere, it is reported that an estimated, 280.000 hip fractures, 700.000 vertebral, and 250.000 wrist fractures occur each year in the USA [1]. In cases of non-union (5% of all fractures), where the bone's regenerative abilities are compromised, surgeons need to intervene to bridge the bone defect. The demand in the surgical market is highlighted by the fact there are around 4.000.000 operations involving bone grafting or bone substitute materials performed around the world annually [1].

Back pain due to degenerative disease is another major condition for individuals and society alike. It is the second most common cause for sick leave. **Spinal surgery** intervention can be effective in tackling this condition. In the USA, 50% of bone graft operations concern spinal fusions [18]. Also, hip and knee replacement operations are on the rise. **Joint replacement surgery** is necessary if the articulation between two bones is extensively diseased or injured beyond repair. The leading reason is osteoarthritis, a disease caused largely by trauma and wear and tear on the body. The surgery replaces a natural joint with an insensate prosthetic implant. Hip and knee replacements are expected to increase dramatically in the next 20 years. Currently, about 10% of primary joint replacements undergo revision surgery.

The regeneration of bone has become a major clinical need in the fields of orthopedic, spinal, cranial, dental and maxillofacial surgery. For example, conditions in the orthopedic surgery where bone grafting is applicable, include gaps at fracture sites, delayed unions and non-unions of fractures, arthrodesis, enhancement of joint replacement prostheses, spinal fusion and to fill the empty screws holes left after bone plate removal [19].

As the population ages, the number of operations performed on bone is expected to increase. Therefore, two important worldwide challenges lay ahead; (1) treatment of the deteriorating health of an aging population and, (2) decrease in healthcare costs to meet the needs of an expanding population [1, 20]. Currently, autografts, allografts, and/or bone graft substitutes are used by surgeons to restore areas of lost bone. Surgical implants are also used alone or in addition to bone grafts to replace the diseased bone. These are discussed in the following section with emphasis on ceramic materials.

## 1.3 Biomaterials for bone regeneration: from biocompatible to bio-instructive

Bone substitute materials can be either of biological or synthetic origin. The conventional treatment approach for bone defects involves the use of biological bone grafts. With a surgical procedure, a patient's own bone, called the '*autograft*' is removed from another site (e.g. hip or ribs) and utilized to fill up the defect. Despite medical advances, the autograft remains the 'gold standard', however the applicability of this approach is limited due to the scarce amount of bone that can be safely harvested and the risk of donor site morbidity, as well as the requirement for additional surgical intervention [1]. Biological graft alternatives to autografts include the *allografts*, which refer to bone from a human donor (cadaveric bone usually obtained from a bone bank). However, the use of allografts is limited by the immunogenicity, risk of disease transmission and inconsistent healing [21].

Because of the above disadvantages, an alternative strategy for bone grafting is required in the form of synthetic materials that can promote bone regeneration. During the last decade, there has been significant progress in basic research which led to an increase in quality of clinically applied bone substitute materials categorized as ceramics, polymers, and composite materials. The scientific focus has been on improving and expanding the biological performance of these materials from a passive role where materials were merely accepted by the body to an active role in which materials instruct their biological surroundings. Consequently, the definition of a biomaterial has evolved from ''*a non-viable material used in a medical device, intended to interact with biological systems*'' to ''*a substance that has been engineered to take a form which, alone or as part of a complex system, is used to direct, by control of interactions with components of living systems, the course of any therapeutic or diagnostic procedure, in human or veterinary medicine*'' [1, 22].

The evolution of biomaterials began with the first generation, which included inert and tolerant biomaterials, such as dense alumina, zirconia and titanium, designed to provide mechanical support without, however, eliciting any specific cellular responses. Since the mechanical properties of these materials proved indispensable for loading bearing applications, the first generation biomaterials are still widely used in hip and knee replacement surgery, as will be discussed below. However, the development of second generation biomaterials that took place in the past decade focused on synthetic biomaterials that encompassed bioactive and osteoconductive properties as well as achieving osteointegration. These bone substitute materials include demineralized bone matrix (DBM) from human tissue banks, ceramics, collagen, bioactive glasses, polymers and composites. Many are currently used as fillers in bone surgery. They can also function as carriers for growth factors and antibiotics, and may be presented as porous scaffolds, blocks, fibers, granules, powders, gels, and sprays, depending on the application.

In view of the development of a new third generation of biomaterials, which will successfully aid bone regeneration, more challenges lie ahead for the fabrication of bone biomaterials which encompass the following characteristics [22]:

(a) Osteoinduction
(b) Angiogenesis
(c) Mechanical stability
(d) Biodegradibility
(e) Handling properties

A suitable synthetic biomaterial may reduce, or in some cases, eliminate the need of bone grafting, thereby avoiding the disadvantages associated with bone grafts. Nevertheless, it is unlikely that one grafting material will eventually be found to optimally resolve all reconstructive challenges in the clinical setting. It is possible that combinations of different materials, improved in their biomechanical and biological performance, will provide new solutions.

There is a large number of bone substitute materials, however, it is beyond the scope of this introduction to give a complete listing. Therefore, in the following section, we present the ceramic materials used in the present thesis. For reasons of convenience, the main properties and definitions for bone substitute materials used throughout the thesis are given in Table 1.1.

**Table 1.1. Definitions of properties relevant to a bone biomaterial.**

| Property | Definition |
|---|---|
| **Biocompatibility** | The ability to perform with an appropriate host response in a specific situation |
| **Bioactivity** | The ability of a material to positively enhance the rate or quality of bone formation |
| **Osteogenesis** | The process of new bone formation |
| **Osteoconduction** | The ability of a material to permit bone growth on its surface or down into pores |
| **Osteoinduction** | The ability to induce new bone formation by stimulating the differentiation or maturation of stem cells into bone-forming cells |
| **Osseo- or osteo-integration** | The direct structural and functional connection between the pre-existing bone and the surface of an implant |

Information from **[13, 22]**

## 1.4 Ceramic biomaterials

Ceramics are usually inorganic compounds involving both metallic and non-metallic elements for which the interatomic bonds are either totally ionic or predominantly ionic with some covalent character. Ceramics can be crystalline or amorphous, in which state they are called glasses. According to D. Williams' recent classification, ceramics are either oxides, phosphates, silicates, nitrides, carbides, titanates or optically active ceramic/metallic nanoparticles [13].

Ceramic materials hold a prominent position among synthetic bone substitute materials. Their well-established biocompatibility, and in certain materials such as calcium phosphates bioactivity and osteoconductive properties, provide ceramics with desirable qualities as implant materials for different applications throughout the body. These applications cover all areas of the skeleton, such as bone fillers, treatment of bone defects, fracture treatment, orthopedics, and cranio-maxillofacial reconstruction. The understanding that not only the mechanical but also the biological properties of ceramic materials can be adjusted in terms of composition, structure and porosity, is leading to a new prospect of tailoring biological interactions at the biomaterial-tissue interface to meet specific applications [4, 22, 23].

Ceramics have been indispensable materials since ancient times and continue to be explored for new applications [24]. Four decades ago, specially designed ceramic materials were applied for the repair, reconstruction, and replacement of diseased or damaged parts of the body, marking a revolution in the use of ceramics. At the same time, the term “bioceramics” emerged, which refers to *biocompatible ceramic materials that are applicable for biomedical or clinical uses*. ‘Bioceramics’ are defined as any ceramic, glass, or glass-ceramic used as a biomaterial, which is a material intended to interface with biological systems, to evaluate, treat, augment, or replace any tissue, organ, or function of the body [4]. Bioceramics include the family of calcium phosphates (e.g., HA ($Ca_{10}(PO_4)_6(OH)_2$) and tricalcium phosphate (TCP) ($Ca_3(PO_4)_2$)), alumina ($Al_2O_3$), partially stabilized zirconia ($ZrO_2$) and bioactive glasses. Their applications can be categorized into three main fields, i.e., orthopaedics, dentistry, and cancer treatment. In orthopedics, bioceramics are used for joint replacement (especially total hip replacement (THR)) as well as defect and fracture repair. Dense solid ceramics of high mechanical strength, such as alumina and zirconia are used in load bearing sites e.g. dental caps and ball heads for THR, whereas the calcium phosphate based ceramics like hydroxyapatite are used as bone graft substitutes for bone regenerative applications [4, 25].

In the following section, we discuss the main characteristics and evolution of alumina and zirconia ceramics in regard to their application as surgical implants to replace the diseased bone. We also discuss the wide use of calcium phosphates as synthetic bone grafts used by surgeons to restore areas of lost bone. Special formulations of calcium phosphates into nanoparticles are very promising as gene delivery systems to aid bone regeneration and are discussed separately in section 1.5. Finally in this section, the mechanical properties of ceramics as well as cell response to ceramic materials is introduced. It is further discussed in the following chapters of this thesis in view of the experimental results.

### 1.4.1 Aluminum oxide (alumina)

Polycrystalline aluminum oxide ($Al_2O_3$) or alumina was the first ceramic material to be used in orthopedic surgery, in the 1970s. At the time, the mechanical properties proved insufficient for reliable quality, especially due to low toughness which created a susceptibility to fracture. The mechanical properties depend on purity level, porosity and grain size. Following improvements in the technology of alumina ceramics, alumina is currently used in the form of α-corundum alumina, of rhombohedral crystal structure and a minimum purity of 99.5%, a density greater than 3.98 g/cm$^3$ and a grain size of 2-5 μm. It is used in highly stressed orthopedic applications, including alumina-alumina bearing surfaces in total hip arthroplasty (THR). Dense alumina is a very hard material (> 2000 Vickers Hardness) and has a high Young's Modulus of 380 GPa, which is nearly double compare to stainless steel. Alumina is highly resistant to corrosion, or degradation and is one of the most inert of biomaterials with respect to physiological fluids. From 2000 until present, improvements have led to the development of a new generation of alumina ceramics such as, Alumina Matrix Composite (AMC) or Alumina-Zirconia composites, which showed dramatically reduced rates of fracture (as low as 0.54 to 0.0% have been reported). More than 100,000 components of AMC have been implanted and no complications have yet been reported [13, 26].

### 1.4.2 Zirconium oxide (zirconia)

Between 1970 and 1990, alumina's brittleness has limited its use to femoral heads with a large diameter (32 mm). Zirconia ceramic was introduced as an alternative to alumina ceramic for femoral heads, since it was harder and more resistant to fracture and therefore could be used to manufacture smaller femoral heads (28 mm diameter). The first generation of zirconia femoral heads became available in 1988 [27]. Research on the use of zirconia ceramics as biomaterials has focused on their use as ball heads for ceramic-on-ceramic hip prostheses, but further developments have resulted in the application of zirconia as dental implants. Zirconia cores for fixed partial dentures (FPD) on anterior and posterior teeth and on implants are now available [28]. Furthermore, since it is a white opaque solid and its color is similar to teeth, it has become attractive for dental crowns; zirconia's color can be modified by the selective use of dopants [13].

Zirconia is a crystalline dioxide of zirconium ($ZrO_2$) and its crystals can be organized in three patterns: monoclinic, cubic and tetragonal. These three phases exist at different temperatures and their stability depends on the presence of some additives. At room temperature zirconia is in an unstable, monoclinic phase. It transforms to a tetragonal structure at 1170 $^0$C and to a cubic phase at 2370 $^0$C. During cooling, the tetragonal-monoclinic transformation takes place with a volume expansion of 3-4%. In pure zirconia, the stresses generated by this expansion could cause cracking and disintegration. By the addition of “stabilizing” oxides, like CaO, MgO, $CeO_2$ and $Y_2O_3$, the tetragonal and cubic phases can be maintained at room temperature. Zirconium dioxide can thereby occur in stabilized and partially stabilized form [13] .

Crucially, the tetragonal phase may transform into the monoclinic form on the application of stress on the zirconia surface and this produces a volumetric change in the crystal, where the stress is applied. This expansion creates a stress field that acts in opposition to the stress filed that is promoting the crack, thereby sealing the crack. More energy, i.e., higher forces, is then necessary for the crack to continue. Though, the crack does not go away, it does not propagate any further at that specific time. As a result, a significant increase in the fracture toughness is produced [13, 29, 30].

According to this toughening mechanism, partially stabilized zirconia is formed (PSZ) with the addition of 8% MgO to zirconia, which allows the formation of a fully cubic structure at 1800 ºC. During cooling, the metastable tetragonal phase forms within the cubic matrix.

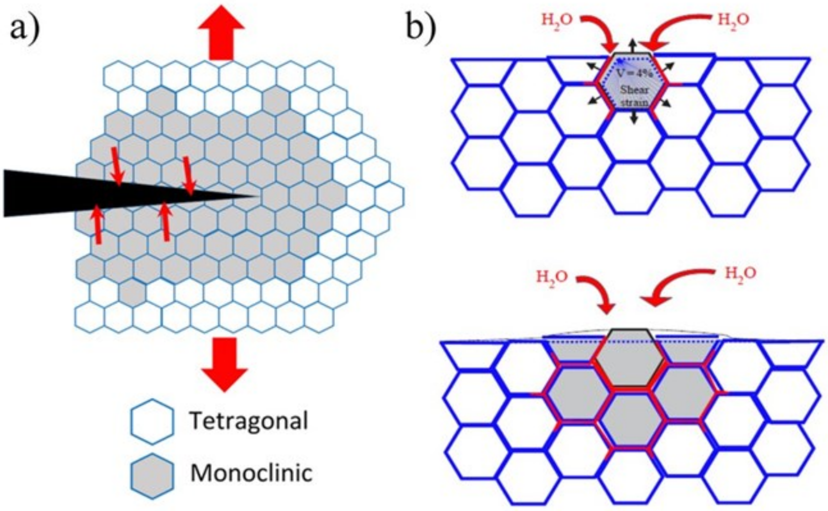

**Figure 1.2. Schematic illustration of (a) the phase transformation mechanism in zirconia ceramics and (b) zirconia ageing.**
(a) The phase transformation mechanism in zirconia ceramics hinders crack propagation through transformation of tetragonal grains to the monoclinic form. (b) Nucleation on a particular grain at the surface, leading to micro-cracking and stresses to the neighbors (top); growth of the transformed zone, leading to extensive micro-cracking and surface roughening (bottom). Red path represents the penetration of water due to micro-cracking around the transformed grains. Image (a) from Palmero *et al*. 2014 [31] and (b) from Chevalier 2006 [29].

$ZrO_2$ stabilized with yttrium oxide or yttria ($Y_2O_3$) has better mechanical properties than other combinations; although its sintering is much more difficult, this is the principal kind of zirconia considered for current medical use [28]. This material, known as tetragonal zirconia polycrystals (TZP or Y-TZP) contains 2-3% $Y_2O_3$ and is constituted solely by submicron crystals of the tetragonal phase.

Zirconia has mechanical properties similar to those of stainless steel and it has been called "ceramic steel". The success of TZP as a biomaterial was due to the combination of high fracture toughness, strength, high wear resistance and excellent biocompatibility. Until 2006, more than 600,000 zirconia femoral heads had been implanted worldwide [29].

However, since TZP exists in a metastable tetragonal phase it can undergo further transformation under different conditions. This unfavorable phase transformation was first reported by Kobayashi *et al*. and is now highly accepted [32]. In fact, it was found that TZP can undergo a low temperature degradation (LTD), also called '*zirconia ageing*', with catastrophic loss of properties (Figure 1.2). In the presence of either water or water vapor at relatively low temperatures, and for an extended period of time, a transformation process can start in isolated grains near the surface, which then passes to neighboring grains as volume expansion occurs. This opens up cracks and allows the ingress of water into the bulk material [13].

Therefore, despite the usefulness of the transformation toughening mechanism, TZP femoral heads are prone to degradation after several years of implantation in the human body, creating an uncertainty over the implants' long term stability. The resistance to ageing varies with microstructure and processing history; some batches of femoral heads received inappropriate treatment leading to a large number of clinical failures in 2001-2002. These failures are now associated to an accelerated ageing in two particular batches of the leader Prozyr® product [29].

Nevertheless, a twelve year follow-up study on ceramic implants of alumina and zirconia showed that the increase in rate of wear in the zirconia group was only evident after eight years and was associated with the altered roughness and roundness which was observed on the retrieved heads. In comparison, during the same 12-year period there was, however, no significant change in the rate of wear in the alumina group, which was found to be much less than the rate of wear of zirconia (0.07 mm/year for alumina and 0.4 mm/year for zirconia after five years of implantation) [27].

During the last decade, the need for 'ageing free' zirconia ceramic biomaterials has led to the development of alumina-zirconia composites, which are discussed below.

### 1.4.3 Alumina-Zirconia composite ceramics

Alumina-zirconia composite ceramics have overcome the limitations of alumina's low toughness and zirconia's ageing effects. These composites exhibit better mechanical properties such as higher hardness (owing to the presence of alumina) and toughness (supported by the presence of zirconia). A good example of Alumina-Zirconia is the Biolox delta®, manufactured by CeramTec AG (Plochingen, Germany), which consists of 80 vol.% $Al_2O_3$, 18.5 vol.% $ZrO_2$ and 1.5 vol.% of mixed oxides ($CrO_2$, $Y_2O_3$ and SrO), which can induce additional toughening mechanisms. Alumina toughened zirconia composites have also been produced. Currently, ZIRALDENT® manufactured by Metoxit AG is the strongest biomedical ceramic known with an alumina content of 25% and over 2000 MPa strength. Apparently, by optimizing the microstructure and the sintering conditions, materials with remarkable mechanical properties are produced [26, 31]. Examples of products using alumina, zirconia and alumina-zirconia ceramics are shown in Figure 1.3.

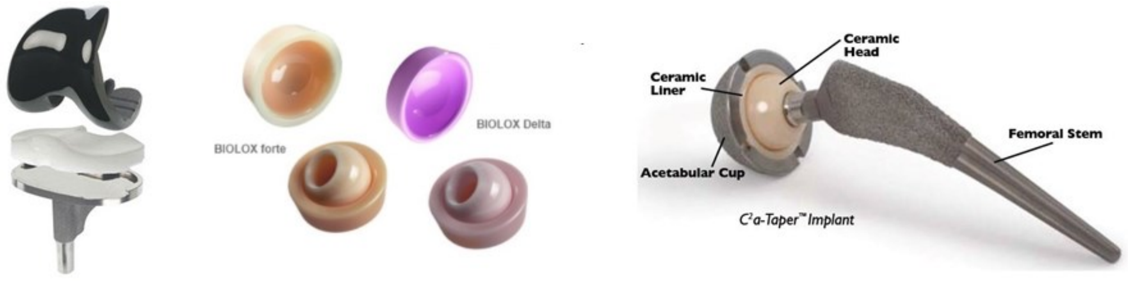

**Figure 1.3. Examples of alumina and zirconia applications in orthopedics.**
(left) zirconium oxide component (shown in grey) in a knee replacement device (Oxinium); (middle) alumina (Biolox forte) and alumina-zirconia (Biolox delta) cups (liners) and.femoral heads for hip replacement prosthesis; (right) the $C^2$ a-Taper (Biomet) complete hip replacement implant showing the position of the ceramic head and liner in the device (Images retrieved from: www.smith-nephew.com/, www.ceramtec.com, www.biomet.co.uk )

### 1.4.4 Calcium phosphates

Calcium phosphates are widely used biomaterials based on their similarities to bone, enamel and dentin. Depending on their chemistry and microstructure they exhibit different degrees of stability/degradation and resorption. Most calcium phosphate ceramics are crystalline and several phases of calcium phosphate ceramics are available with different Ca/P ratios. They can be formulated as solid components or used as cements after *in situ* injection [13].

Hydroxyapatite (HA) $Ca_{10}(PO_4)_6(OH)_2$ has the maximum Ca/P ratio (1.67) and is the most stable of all calcium phosphates and superior in the promotion of early bone regeneration. Even though it is not osteoinductive, it possesses good osteoconductive properties as well as a remarkable ability to bind directly to bone. Is it used as a solid or granular bone substitute and as a coating on orthopedic and dental prostheses. Unlike HA, tricalcium phosphates (TCP), $Ca_3(PO_4)_2$ with a Ca/P ratio of 1.5, are resorbable and are used as bone fillers in either block, granular or powder forms. Neither of these ceramics is clearly superior to the other, but each provides advantages for certain applications [4, 13].

Recently, special formulations of calcium phosphate into nanoparticles are gaining great interest for the development of smart biomaterials. These are discussed separately in section 1.5, page 21.

### 1.4.5 Mechanical properties and porosity

The mechanical properties of ceramic biomaterials will influence their application as implants in the human body. Despite the complexity of forces applied to an implant these are usually rationalized as *tensile forces*, which cause the material to stretch, *compressive forces*, which cause the material to compress, and *shear forces*.

By definition, the ultimate compressive strength of a material is that value of uniaxial compressive stress reached when the material fails completely. The *compressive strength* is usually obtained experimentally when a compressive stress (the force $F$ acting per unit cross-sectional area $A$ or $F/A$) is applied on a cylindrical specimen. Stress is often given the symbol $\sigma$. The application of force results in deformation $\delta l$ which is normalized to the original length $l$, giving the ratio $\delta l/l$ which is the strain $\varepsilon$.

A *stress–strain* curve for a given material is plotted by the instrument and would look similar to the following (Figure 1.4, left):

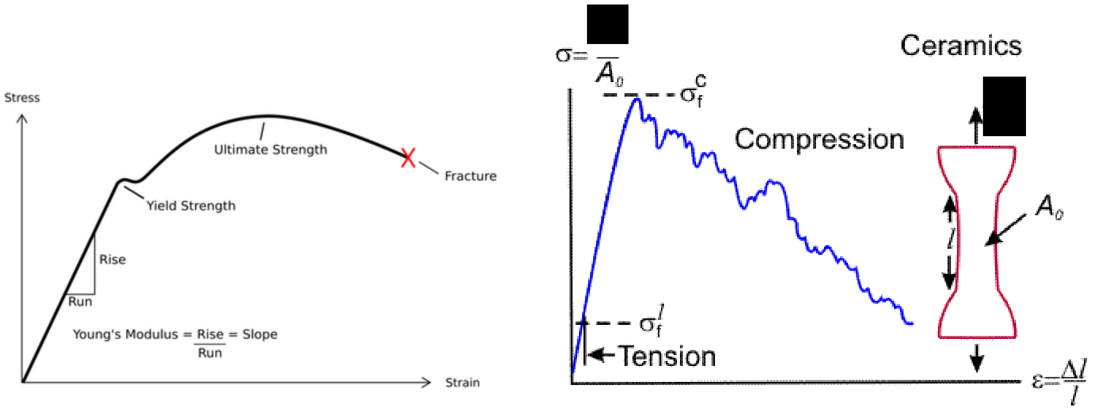

**Figure 1.4. Stress-strain curve of a material.**
(left) A typical stress-strain curve showing elastic deformation of the material in the linear region followed by plastic deformation; (right) a stress-strain curve for a ceramic material.

In the linear region of the stress-strain curve, stress is proportional to strain, and the material undergoes elastic deformation i.e. the deformation is reversible and the atoms will revert to the previous positions when the stress is removed. Hence for this region $\sigma = E. \varepsilon$, and the slope $E$ refers to *elastic modulus* or *Young's modulus*, which is measured in pascals, Pa. A material with a high elastic modulus can be considered to be rigid and a material with a low elastic modulus can be considered to be flexible e.g. alumina has a Young's modulus between 350-400 GPa and cortical bone around 14 GPa.

Ceramics are described as *brittle* since they fracture without any appreciable plastic deformation beyond the ultimate compressive strength point (Figure 1.4, right). The Young's modulus of elasticity of ceramic materials is quite high, and ceramics under compression can withstand a high load. However, the presence of micro-cracks causes the brittle failure of ceramic materials under tension at the application of low stress. The compressive strength of ceramics depends on the total volume of *porosity*. An increase in the void volume results in a reduction of mechanical strength, setting therefore an upper limit in porosity and pore size. The extent to which pore size can be increased while maintaining mechanical requirements is dependent on many factors including the nature of the biomaterial and the processing conditions used in the fabrication.

The effect of porosity on mechanical properties of ceramics has been mainly studied in calcium phophates as bone substitutes [33].

The open porosity, which is the porosity accessible to a liquid (interconnection between pores) can be quantified by mercury intrusion porosimetry or the Archimedes method, whereas pore size can be measured using scanning electron microscopy.

The total porosity of the samples can be calculated by dividing the scaffold density ($\rho_{scaffold}$) by the theoretical material density ($\rho_{material}$) and subtracting the result from one [34, 35]:

$P_{total} = (1-\rho_{scaffold}/\rho_{material}) \times 100$.

The ceramic scaffold density can be determined by dividing the weight by the volume of the scaffold and the material density is the density of the material of which the scaffold is fabricated (the average densities of fully dense polycrystalline zirconia and alumina are 6.05 g/cm$^3$ and 3.96 g/cm$^3$ respectively).

### 1.4.6 Cellular response on ceramics

Understanding how cells interact with a substrate is crucial in the development of functional biomaterials, capable of directing tissue development. Cells are able to interact with their environment through the process of cell signaling, mediated by a number of receptors which are located both on the cell surface (transmembrane) and within the cell cytoplasm (intracellular). The receptors are coded to interact with specific molecules that induce a specific intracellular response, such as cell division (proliferation), cell maturation (differentiation), gene expression, matrix/protein synthesis, or ion channel regulation. Signaling molecules include ions, peptides, proteins or segments of proteins attached on adjacent cells or implant surfaces. Among these, growth factors, such as bone morphogenic proteins (BMPs) reside in bone matrix and have the ability to control tissue formation by acting both mitogenically and morphogenically i.e. stimulating the proliferation and differentiation of osteoprogenitor (mesenchymal) stem cells in the chondro- and osteoblastic direction [23, 36].

Another way in which cells are able to sense their environment is through cell adhesion molecules (CAM) such as integrins and cadherins. Most cellular interactions with the extracellular matrix (ECM) occur via integrins, which are transmembrane proteins that bind specific segments on extracellular matrix proteins, whereas their intracellular component interacts with the cell cytoskeleton, thus enabling cell–matrix adhesion in addition to signal transduction. The arginine–glycine–aspartate (RGD) tripeptide sequence is the minimal structure required for cell binding and is incorporated within the structure of a number of the key noncollagenous proteins (NCPs) of bone matrix (e.g., bone sialoprotein, osteopontin), and in a number of other extra-cellular proteins such as fibronectin and vitronectin [23].

Therefore, bone cell behavior is regulated through a combination of processes involving the exchange of signaling molecules and direct contact with local tissues or implant surfaces. In addition, mechanical forces are believed to regulate both osteoblasts and osteocytes though integrin-mediated cell attachment. Certain proteins, such as fibronectin have been found to alter their conformation, exposing more binding sites, in response to mechanical stress. Consequently, cell-ceramic interactions may be mediated both directly through ion exchange as a result of chemical dissolution and indirectly as a result of the interaction between ceramic surfaces and circulating proteins, and the resulting signaling cascade induced in the surface-adherent cell population.

The morphology of ceramic implants has been long considered and many studies on non-resorbable hydroxyapatite ceramics have demonstrated a greater degree and faster rate of bone ingrowth with increasing porosity [4, 23, 35]. The importance of pore size, porosity and interconnection size, has been recognized, both as a function of structural permeability and mechanics. More recently, the role of the microstructure and pore geometry has been considered with respect to the influence of these parameters on entrapment and recruitment of GFs and matrix proteins [37]. Despite the fact that the optimum ‘type’ of porosity remains in dispute, there is a consensus that a 60% porosity threshold exists (in HA ceramics), below which bone apposition in the porous chambers cannot be expected. Also, a minimum pore size of 100 μm has been reported, but further studies have suggested that pore size is not the controlling factor [23]. In fact, pore interconnectivity, which is often related to both pore size and the extent of porosity, is key to rapid and sustained bone growth [38]. This can be explained by considering the fact that bone is a mineralized tissue that relies heavily on the presence of an internal blood supply to deliver nutrients and oxygen that do not readily diffuse through it. Any new bone formation or repair must always be preceded by the formation of a vascular network, the rapidity and extent of which is strongly influenced by the degree of structural interconnectivity between pores. Thus, both the degree of scaffold porosity and pore interconnectivity are likely to affect the perceived bioactivity of a ceramic biomaterial, as a function of increasing permeability of its structure.

Biological response to biomaterials is greatly affected by chemistry, and implant materials are often classified as inert (or near inert) or bioactive based on this response. For example, metals and dense alumina and zirconia ceramics are near inert. The most common reaction to near-inert materials is the formation of a fibrous encapsulation, where a thin (1-3 μm) fibrous layer is initially adsorbed onto the implant surface, resulting in no direct chemical bond between the implant and the tissue. The fibrous layer isolates the implant from the tissue and eventually thickens, in response to ion release from the implant and as the relative motion between the implant and the tissue increases. This can lead to implant loosening and failure. In contrast, bioactive materials such as HA and other calcium phosphates, are distinct in their ability to participate in dynamic surface exchange, with the physiological environment attaining a degree of chemical equilibrium with the host tissue at the implant interface. No fibrous layer is formed and the material is said to bond directly with tissue [23].

Chemistry influences cell behavior through two principal mechanisms:

i. directly through dissolution and release of ionic products *in vivo* which interact directly on local cells (via ion channels (e.g., Ca) to regulate gene expression or influence cell differentiation), or influence cell behavior by their effect on local pH and
ii. indirectly through the effect of surface chemistry on protein adsorption, growth factor entrapment, and subsequent cell attachment and function.

For example, dense HA is accepted to be osteoconductive, and to directly form a chemical bond with bone. The key to HA bioactivity lies with the influence that its surface charge and ionic specificity has on modulating the population and conformation (and thus potency) of proteins absorbed on its surface and their subsequent mediation of cell attachment and response. Also, on a localized scale, pM or nM concentrations of ionic species may be released from non-resorbable porous HA ceramics which may contribute to an osteoinductive behavior following direct chemical interaction with adjacent cells. HA biomaterials possess surfaces that are suitable for bone ingrowth based on their chemical similarity to the mineral part of bone.

On the other hand, tough and strong ceramics like zirconia and alumina are not capable of creating a biologically adherent interface layer with bone due to the chemically inert nature of these two stable oxides. However, several efforts have been reported to enhance the bioactivity of these ceramics by creating chemically functional groups e.g. Zr-OH on the surface after chemical treatment in $H_3PO_4$, $H_2SO_4$, HCl, and NaOH at high temperatures and for several days. Following treatment, alumina and zirconia were reported to be capable of inducing apatite nucleation in simulated body fluid (a solution with ion concentrations and pH value similar to that of human plasma at body temperature) [39].

## 1.5 Nanoparticles in bone regeneration

The desired biological performance of bone substitute materials has consequently shifted from a passive role where materials were merely accepted by the body to an active role in which materials instruct their biological surroundings. The objective of developing functionalized or so-called smart materials, containing bioactive molecules to directly influence cell behavior  marks the evolution towards a new generation of bio-instructive bone substitute materials that possess inherent biological cues for bone regeneration [22, 40].

In this context, refined materials such as nanoparticles (any feature characterized by dimensions of the order of 100 nm or less, [13]) that are in the same size range as integral parts of natural bone, such as hydroxyapatite crystals or cellular compartments, are promising candidates for local applications. Nanoparticles can penetrate the cell wall and be used for **cell labeling** or **drug delivery or gene therapy via cell transfection**, for a therapeutic purpose [41, 42]. The various potential applications of nanoparticles in bone are given in

Figure 1.5.

To be considered for clinical applications, nanoparticles should fulfil the following criteria: they should be **non-toxic for cells**, i.e., bioinert or biodegradable; they should **effectively carry the molecule of interest**, e.g., labeling agent or drug; and they should **exert their actions specifically on their target**, without evoking side effects in other tissues [41].

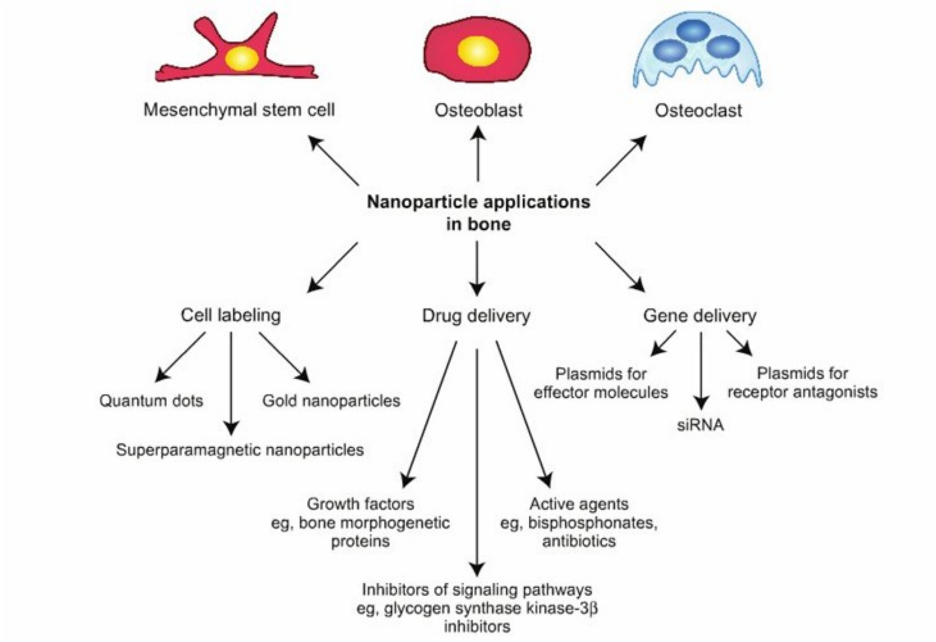

**Figure 1.5. Nanoparticle applications in bone.**
Image from Tautzenberger *et al*. [41].

Diverse nanoparticles, are investigated for different application areas as certain criteria need to be fulfilled. Gene delivery using nanoparticles as carriers is a promising application in bone regeneration because cell transfection potentially allows for a prolonged therapeutic effect compare to pure proteins. The small amounts of DNA needed to trigger protein production are technically easier to produce, result in protein production within the target cells and in the long-term offer the potential of better control over amounts of protein expressed [41, 43]. Below, we discuss the application of nanoparticles in gene delivery which is the focus of our studies.

### 1.5.1 Nanoparticles for gene delivery

Gene therapy via gene delivery (cell transfection) aims to deliver genetic material into the somatic cells of a patient, resulting in a therapeutic effect by either correcting a genetic defect, by overexpressing proteins that are therapeutically useful, or by suppressing the expression of a gene [44]. Because the cellular uptake of naked plasmid DNA is generally low as macromolecules such as RNA and DNA do not passively diffuse through the lipid membrane, it is highly desirable to use effective non-toxic gene carriers. In this regard, gene delivery using nanocarriers may prove an effective tool towards this goal. Currently, various nanoparticle platforms are being explored, based on lipids, cationic polymers and inorganic nanoparticles. These target a number of therapeutic treatments including cancer, neurodegenerative and cardiovascular diseases and regenerative medicine (Figure 1.6) [42, 44-46].

The therapeutic strategies under development are classified as *in vivo* and *ex vivo*. The *in vivo* approach consists of delivering genes directly to the patient, locally or systemically, by direct injection or through controlled release from a scaffold. With this method, it is important to include some cell targeting strategy to avoid transfection in secondary tissues. For example, silencing of the abnormal overexpression of defined genes developed in tumors using siRNA gene delivery, is pursued in cancer research [44].

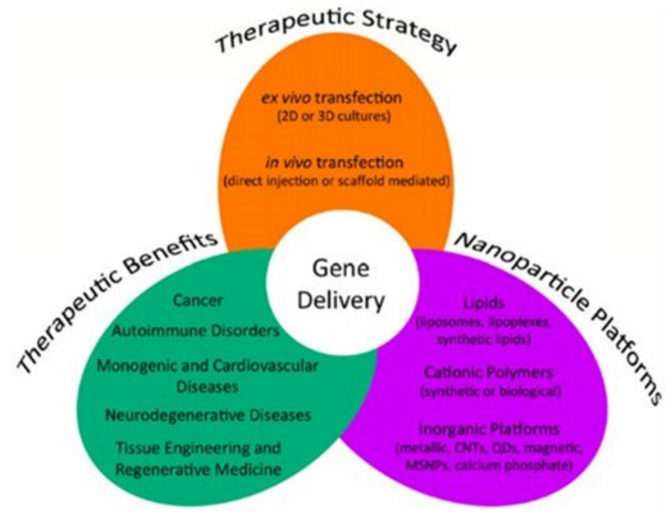

**Figure 1.6. Variables associated with the use of nanoparticles in therapeutic gene delivery applications.**
Image from Ojea-Jiménez *et al.* [44].

The *ex vivo* or cell-mediated gene transfer method is especially suitable for tissue engineering applications. It involves the *in vitro* genetic manipulation of cells e.g. stem cells in cell culture dishes or in 3D environments (such as a matrix or biodegradable scaffold) followed by the reintroduction of the cells into the patient body. After implantation, the transfected cells could recruit the appropriate host cells to migrate in the scaffold area by expressing the delivered genes that perhaps code for growth factors, morphogenic proteins, or cell-type-specific adhesion molecules. Attempts have been made to use the *ex vivo* therapy for bone, cartilage, wound, urothelial, nerve tissue regeneration and for treating diabetes using viral or non-viral vectors and porous polymers as scaffolds for cell transplantation [44, 47].

The size of nanoparticles has been found to have a significant impact on their cellular uptake. Compare to microparticles, nanoparticles have in general higher intracellular uptake. In previous studies, 100 nm size biodegradable polymer nanoparticles showed 2.5-fold and 6-fold greater uptake compared to 1 mm and 10 mm microparticles, respectively [42]. *On average, the size of nanoparticles ranges from 10-200 nm which is comparable to the size of proteins.* In this way, nanoparticles can interact with biomolecules at the cell surface or inside the cell, and deliver genetic material such as DNA, RNA or siRNA into targeted cells for gene expression [48].

Generally, nanoparticle based gene delivery is very promising field for the treatment of bone diseases of different origin-from fractures and osteoporosis to malignant tumors. Nanoparticles feature various modifiable characteristics, such as particle chemistry, and have the potential for functionalization allowing targeting to cells of interest and attachment to certain surfaces. With local application of nanoparticles, easy spatial separation and potentially tunable temporal action could be achieved. In bone, they could find numerous applications with respect to improvement of bone tissue regeneration, enhancement of implant osseointegration and the prevention of infections. They could be used in the form of bioactive implant coatings, cements or for direct bone injections. With regard to bone regeneration, no clinical trials have been initiated, yet [41]. However, several *in vitro* and *in vivo* studies emphasize the great potential of nanoparticle applications in bone. There are as yet few comparisons between the many different variables in nanoparticle gene delivery studies to show which is best for any particular application is. With few exceptions, all of the results appear positive in showing some gene expression and some consequent effect on tissue growth and remodeling [43].

### 1.5.2 Calcium phosphate nanoparticles for gene delivery

Calcium phosphate ceramics have been used in orthopedics for over 30 years because of their excellent biocompatibility. Due to the rapid development of nanotechnology, the potential of calcium phosphate nanoparticles has received considerable attention [49].

An effective gene delivery vehicle needs to provide the protection of nucleic acids from degradation by extracellular nucleases, show target specificity, efficient cell internalization and the release of the nucleic acid in a functional form in the cytoplasm or the nucleus. In addition, it needs to be biocompatible as well as display low immunogenicity and cytotoxicity.

Among the various platforms used for gene delivery, calcium phosphate (CaP) nanoparticles have inherent advantages compared to other transfection systems and display beneficial features specifically for bone applications [46, 50]:

- Excellent **biocompatibility** since CaP can be found throughout the body in the form of amorphous calcium phosphate and crystalline HA, which is the major component of bone and tooth enamel.
- CaP is **non-toxic** for cells (reasonably high but benign concentrations of $Ca^{2+}$ and $PO_4^{3-}$ (1–5 mM) occur in all vertebrates), as well as **biodegradable**.
- CaP nanoparticles can be functionalized to achieve **target specificity**.
- Preparation methods for CaP nanoparticles are **cost-effective** and easy to perform.
- Calcium facilitates the endosomal/lysosomal escape of nanoparticles due to its fusogenic and membranolytic activity.
- Calcium ions enhance the nuclear uptake of DNA through the nuclear pore complex due to the involvement of calcium in intracellular signaling pathways.

The technique of calcium phosphate *in vitro* transfection was originally discovered by Graham and van der Eb in 1973 [51] and is now used as a routine laboratory procedure that relies significantly on $Ca^{2+}$ divalent metal cations, forming ionic complexes with the helical phosphates of DNA [5] (Figure 1.7).

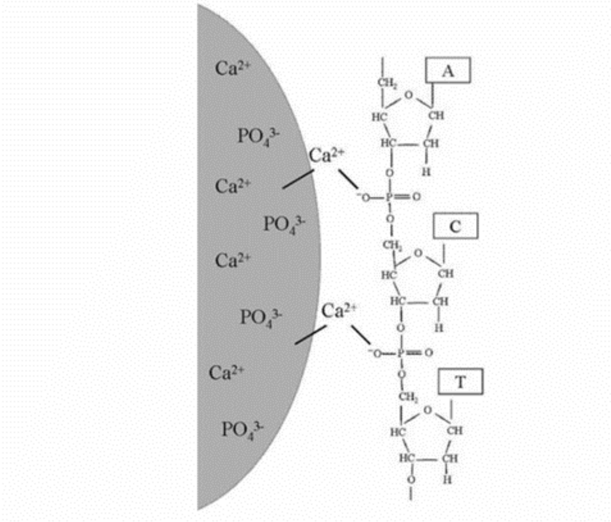

**Figure 1.7. Schematic representation of the interaction between the surface of CaP nanoparticles and nucleic acids**
Image from V. Sokolova *et al.*, 2006, [5].

With this method, amorphous calcium phosphate particles can be formed in a relatively straightforward precipitation reaction that takes place in two steps (Figure 1.8): Calcium chloride solution is mixed with DNA, and a subsequent addition of phosphate-buffered saline solution results in the formation of fine precipitates (nano- and micro- particles) of calcium phosphate with DNA. This dispersion is then added to a cell suspension, and the nanoparticles are taken up by the cells. The calcium phosphate core dissociates in the intracellular environment due to the lowered $Ca^{+2}$ concentration, thus allowing the release of the cargo. The method is simple and inexpensive, but the transfection efficiency is inferior to commercially available transfection agents, which are based on liposomes and polymers [52].

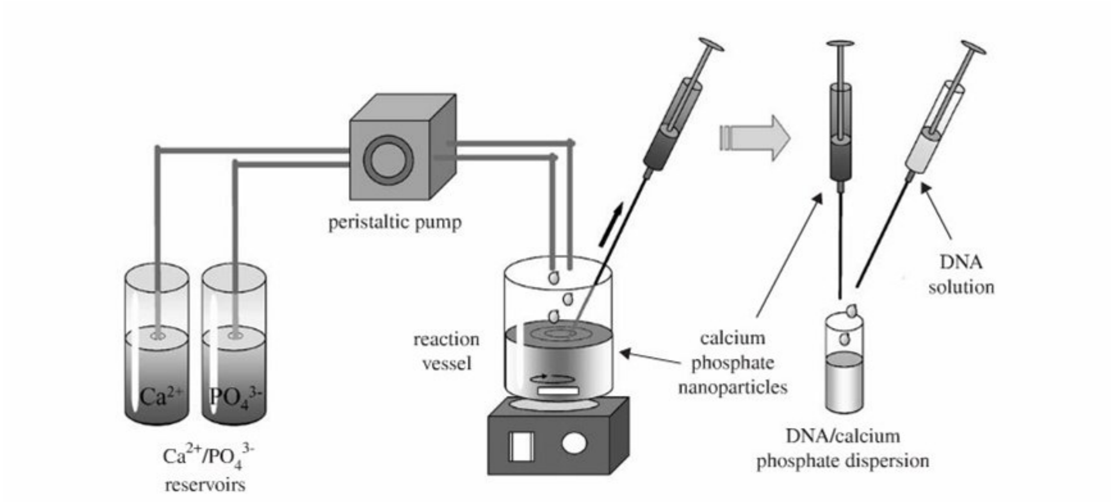

**Figure 1.8. Schematic representation of the set-up used for preparation of calcium phosphate nanoparticles with DNA cargo.**
Image from V. Sokolova *et al*, 2006 [52].

The calcium phosphate nanoparticles prepared by these methods are relatively large (greater than 100 nm) and have significant agglomeration. As a result, the process of cellular uptake is negatively affected, as larger particle precipitates are more difficult to endocytose, leading to decreased transfection efficiency. However, investigations on the physicochemical properties of CaP nanoparticles have identified that key parameters for effective cell transfection are the optimal concentrations of calcium and chloride ions and the formulation of a nanosized non-agglomerated precipitate [53]. Improvements on the synthesis of calcium phosphate nanoparticles basically targeted the formation of smaller precipitate particles easier to endocytose. For example, the self-assembly of a PEG-based block copolymer with calcium phosphate entrapping nucleic acids yielded particles with diameters in the range of hundreds of nanometers. Similarly, lipid-coated calcium phosphate formulations for siRNA delivery have also been developed for controlled disassembly in the acidic environment of the endosomes [44].
Overall, during recent years, several developments have been reported on calcium phosphate particles encapsulating therapeutic nucleic acid and being used for transfection into liver cells, fibroblasts, osteoblasts, tumor cells [52], mesenchymal stem cells [50] and other cells.

During transfection, it is vital that DNA is protected so it can exert its action. Before the DNA successfully enters the nucleus, it has to overcome several physical and chemical barriers, e.g. intracellular degradation in lysosomes [54]. Inside the nucleous, DNA can be digested by nucleases and therefore it needs to be protected from such attacks. In one case, Sokolova *et al*. prepared multi-shell calcium phosphate-DNA nanoparticles and these were used as vectors for EGFP-encoding plasmid DNA. The second layer of calcium phosphate on the surface, protected DNA from degradation within the cell by lysosomes. The transfection efficiency was investigated in various cell lines including T-HUVEC and HeLa cells, and was found significantly higher than that of simple DNA-coated calcium phosphate nanoparticles [52].

It is possible to covalently attach molecules like dyes or antibodies for cell targeting. For instance, calcium phosphate nanoparticles were coated with a shell of silica and covalently functionalized by silanization, either with thiol or with amino groups (D. Kozlova *et al* [6]). Between the calcium phosphate surface and the outer silica shell, biomolecules like nucleic acids (DNA or siRNA) could be incorporated as cargo. Such nanoparticles can be used as cell-specific carriers of biomolecules into cells, e.g. for transfection, gene silencing or cell activation for many applications. Using FITC conjugated nanoparticles, the authors demonstrated the cellular uptake of antibody-coated calcium phosphate nanoparticles in HeLa (epithelial cell line) and MG-63 (osteoblast-like cell line).

### Mechanism of nanoparticle uptake by the cells

The uptake and distribution of different nanoparticle systems in various cell types has been investigated using microscopy analysis and endocytosis-interfering drugs. The results indicated that nanoparticles are internalized efficiently through endocytosis or endocytosis-like processes. Endocytosis begins with invagination of the cell membrane to form an endocytic vesicle enclosing the nanoparticles, continues with endosomal delivery of the nanoparticles inside the cell and maturation of the early endosomes to late endosomes and ends with fusion with lysosomes and distribution to various organelles inside the cell. It is generally distinguished between clathrin-mediated endocytosis, caveolin-mediated endocytosis, clathrin- or caveolin-independent endocytosis and macropinocytosis (Figure 1.9) [42, 55].

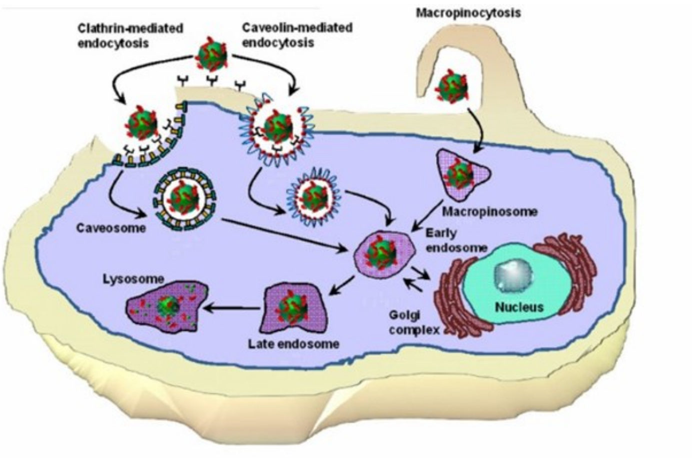

**Figure 1.9. Schematic representation of the different internalization mechanisms for nanoparticles.**
Nanoparticles can be up taken by clathrin-mediated endocytosis, caveolin-mediated endocytosis and micropinocytosis. Image from V. Sokolova *et al*, 2013 [55].

Once the DNA escapes the endosome/lysosome it enters the nucleus where it can be directly transcribed into RNA (transient transfection). Alternatively, it can be integrated into the host chromosome, thus leading to synthesis of the specific protein also in the next generations (stable transfection) [56].

It has been shown that the uptake can be time and concentration dependent [42]. Charge is also another factor affecting nanoparticle uptake. While neutral functional groups on nanoparticles are excellent in preventing nanocarrier–biological interactions, most charged moieties are responsible for active interaction with cells. For example, in the absence of serum, the interaction of cationic liposome-DNA complexes with cells in culture involves many electrostatic interactions between the positively charged complexes and the negatively charged membrane. The internalization of negatively charged gold nanoparticles is believed to occur through non-specific binding and clustering of the particles on the cell membrane, which induces endocytosis [44].

Sokolova *et al*. investigated the mechanism of uptake of fluorescent cationic and anionic calcium phosphate nanoparticles with a diameter of ~120 nm in HeLa cells (human epithelial cervical cancer cells) [55]. Using inhibitors of endocytosis and micropinocytosis in flow cytometry and confocal laser scanning microscopy analysis, they reported that the uptake mechanism of anionic nanoparticles was micropinocytosis. For cationic nanoparticles, the uptake was affected to a lesser extent by interfering drugs, indicating a different uptake mechanism. The nanoparticles were localized in lysosomes after 3 h of incubation.

## 1.6 BMP-7: an osteoinductive member of the Bone Morphogenetic proteins (BMPs) superfamily

For successful bone healing, four prerequisites must be established [1]:

(a) cells with osteogenic potential;
(b) an osteoconductive matrix;
(c) an osteoinductive stimulus;
(d) a mechanically stable environment.

Based on these prerequisites, the standard bone tissue engineering approach is to provide solutions for impaired fracture healing, bone restoration and regeneration through the utilization of *growth factors* (osteoinductive stimulus), *scaffolds* (osteoconductive matrix) and *mesenchymal stem cells* (cells with osteogenic potential) [1].

Bone development and regeneration processes are mediated by several growth factors, including insulin-like growth factor I, transforming growth factor β (TGF-β), acidic fibroblast growth factor, basic fibroblast growth factor and BMPs.

Bone morphogenetic proteins (BMPs) belong to the TGF-β superfamily of paracrine factors that activate heterodimeric receptors with serine/threonine kinase activity. They are involved in numerous mechanisms of organogenesis, notably in skeletogenesis [14]. Their role in bone formation was first shown in 1965 by M. Urist, who made the discovery that demineralized bone could induce new bone formation when implanted in muscle pouches in rabbits [57]. In bone tissue, BMPs are produced by osteoprogenitor cells, osteoblasts, chondrocytes, platelets, and endothelial cells. They are stored in the extracellular matrix during bone formation, where they remain until the matrix is destroyed, either through the natural bone remodeling process or in bone fracture. Upon their release, these molecules act through autocrine and paracrine signaling mechanisms to induce the migration, proliferation and differentiation of osteoprogenitor cells and/or type I collagen synthesis and matrix apposition by mature osteoblasts. They act to initiate bone healing and to maintain the continuous remodeling of bone [41, 43, 45].

Among growth factors, BMPs are known to possess the greatest *in vivo* bone stimulatory capacity and to stimulate the differentiation of MSCs along osteoblastic and chondrogenic lineages and are therefore the most well-known and widely investigated proteins for bone regeneration. BMPs play a regulatory role during embryogenesis and bone and cartilage formation and repair. Over 30 distinct forms of the BMPs exist and the most widely studied are BMP-1 through -7. BMP-2, BMP-4 and BMP-7 are thought to be the most important for bone healing [41, 43, 45]. Their key role in bone healing has led to a growing interest in their potential for use as a biological response modifier, to speed fracture union and bone regeneration in situations where this might not naturally occur [58]. Recombinant human BMP-2 and BMP-7 (also known as osteogenic protein-1, OP-1) have been FDA-approved for clinical use in the regeneration of bone in fracture healing and spine fusion, and have been available since late 2001. Their application at the surgical site has been associated with a delivery system, such as type I collagen and calcium phosphate ceramics to ensure controlled release and avoid systemic diffusion. However, side effects with the use of BMP-2 such as swelling, seroma, and increased cancer risk, have been reported, probably due to high BMP dosage [59]. In a clinical review report, Giannoudis and Tzoudis document the clinical applications and the efficacy of BMP-7 in the United Kingdom in a variety of orthopedic clinical applications, the majority of which included cases of non-union fractures. BMP-7 was administered at the injury site either alone or in combination with autologous bone graft or allograft. According to the study, out of 653 cases, the overall success rate was 82% (535 cases). No local or systemic adverse effects were encountered [58]. This study, supported by the findings of other investigators, confirms the efficacy of BMP-7 as a safe bone-stimulating agent in the clinical setting.

Gene delivery systems using calcium phosphate nanoparticles or polymer/DNA complexes have been investigated for the delivery of BMP-2 *in vitro* and *in vivo* for ectopic bone formation [60, 61]. Also, the effect of BMP-7 on the proliferative and differentiation capacity of osteoprogenitor cells has been reported [62].

BMPs have a dimeric structure, displaying sites for N- and O-glycosylation, which increases the stability and half-life of the protein in the body, in addition to determining the specificity of receptor coupling. They originate from 400- to 500- amino-acid long precursors, which share one signal peptide at the N-terminus, one non-conserved pro-domain among the members of the family, in addition to the mature protein sequence which is located at the C-terminus domain. The mature protein contains from 100 to 140 amino acid residues, with 7 conserved cysteine residues, 6 of which form intramolecular disulfide bridges, while the remaining residues form intermolecular disulfide bridges. This allows for the formation of homodimers, which are indispensable for their biological activity (Figure 1.10) [59, 63].

**Figure 1.10. The dimeric structure of BMP-7.**
Each monomer is represented by one color (blue and orange) and the disulfide bridges are shown (green). Image from Carreira *et al.*, 2014, [59].

The molecular basis of BMP action has been the subject of intensive research activity in recent years leading to a growing understanding of their fundamental action at a cellular level. BMPs act in a time-dependent manner and trigger a cascade of events which lead to chondrogenesis, osteogenesis, and angiogenesis. They control the synthesis of extracellular matrix by the modulation of several genes. A generalized schematic representation of the BMP signaling pathway is shown in Figure 1.11.

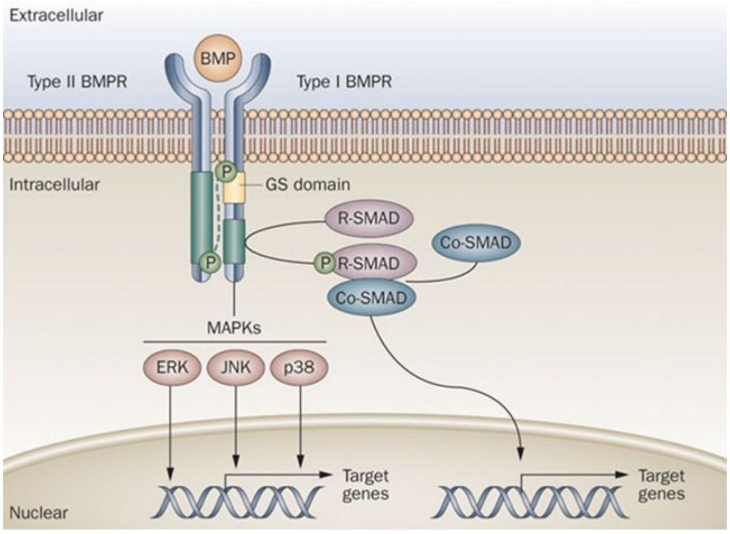

**Figure 1.11. A generalized schematic representation of the BMP signaling pathway.**
Image from Shore et al., 2010, [64]. Abbreviations: BMP, bone morphogenetic protein; BMPR, bone morphogenetic protein receptor; Co-SMAD, common-mediator SMAD; ERK, extracellular signal-regulated kinase; GS domain, glycine–serine domain; JNK, c-Jun N-terminal kinase; MAPK, mitogen-activated protein kinase; R-SMAD, receptor-regulated SMAD.

BMPs initiate signaling from the cell surface by binding type I and type II BMP receptors which span the cell membrane and can activate the Smad cytoplasmic proteins. Upon ligand binding, the BMP heterotetrameric receptor complex activates signaling through type II-receptor-mediated phosphorylation of the type I receptor on the GS domain. Type I receptor phosphorylation is accompanied by decreased binding to the GS domain of proteins that prevent receptor signaling in the absence of ligand binding. Activated type I receptors phosphorylate cytoplasmic signal transduction proteins such as R-SMADs and MAPKs (including JNK, ERK and p38), which, in turn, directly or indirectly regulate the transcription of target genes in the nucleus [64].

# Chapter 2

# 2 Experimental procedures

This Chapter describes the main experimental procedures used for the *in vitro* biological investigation of the interaction between ceramic biomaterials and pre-osteoblastic cells as well as the exploration of cell transfection with DNA-carrying calcium phosphate nanoparticles towards genetic manipulation. It provides information on the **principle and optimization of various bioanalytical, molecular biological, and microscopic methods** used in this study. Further experimental details of all experiments performed in this study are provided in Chapters 3-6. Details on the preparation and characterization of the ceramic materials and the calcium phosphate nanoparticles used in this study are provided in the Appendices I and II.

## 2.1 Ceramic materials

In this study, overall 8 ceramic materials which differed in terms of their porosity (from 19% up to 61%) and composition (alumina, zirconia or alumina/zirconia composite) were investigated (Table 2.1). The fabrication and mechanical characterization of the ceramic samples were performed by the research group of Prof. S. Kulkov at the State University of Tomsk, Russia, whereas the crystallographic phase characterization and chemical composition investigation were performed by Dr. O. Prymak, member of the research group of Prof. M. Epple at the University of Duisburg-Essen, Germany. The exact experimental procedures for the fabrication and characterization are provided in the manuscripts which resulted from this study and a description is also given in Appendix I. Briefly, the ceramic materials were produced by sintering powders. Starting powders of $Al_2O_3$ or $ZrO_2$ stabilized with 3 mol % $Y_2O_3$ or $ZrO_2$ stabilized with 8 mol % MgO (Siberian Enterprise Chemical Group, Russia) were used. Mechanical properties were characterized by compressing tests using the Instron testing systems. X-ray powder diffraction (XRD) was carried out for crystallographic characterization of the ceramic samples. A scanning electron microscope (Philips SEM-515) was used to observe morphology and determine pore size distributions on fracture surfaces of the two ceramic materials and energy dispersive spectrometry (EDS) was used to detect surface elements. Sample porosity was calculated by dividing the scaffold density ($\rho_{scaffold}$) by the theoretical material density ($\rho_{material}$) and subtracting the result from one [34, 35]. Scaffold density was determined by dividing the weight by the volume of the scaffold whereas the material density is the density of the material of which the scaffold is fabricated. The open porosity, which is the porosity accessible to a liquid was measured in water using the Archimedes' principle.

**Table 2.1. Pore sizes and porosities of all (A) zirconia and (B) alumina ceramics used in the thesis.**

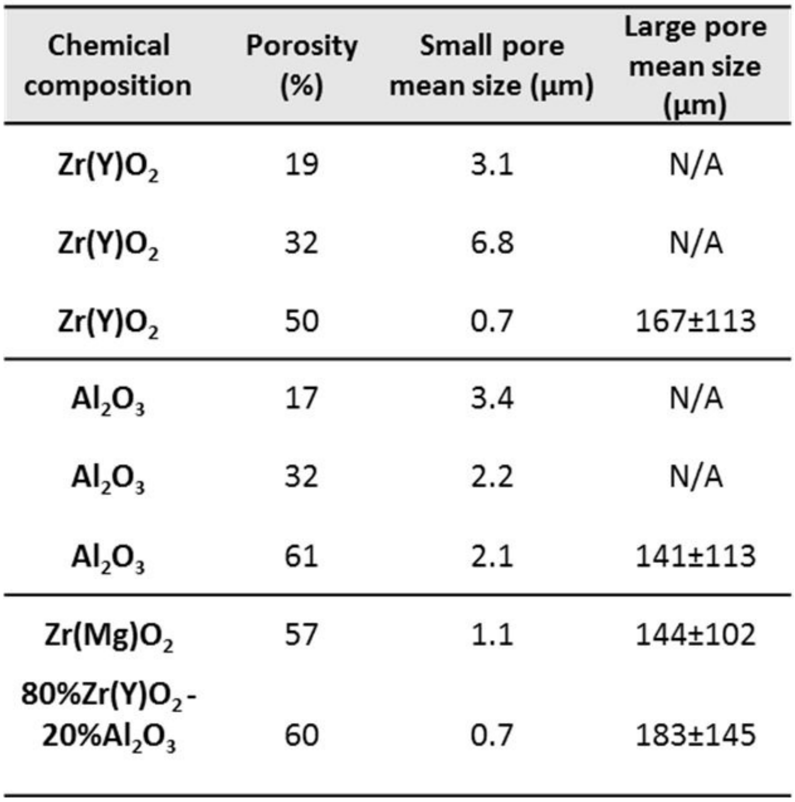

| Chemical composition | Porosity (%) | Small pore mean size (µm) | Large pore mean size (µm) |
|---|---|---|---|
| $Zr(Y)O_2$ | 19 | 3.1 | N/A |
| $Zr(Y)O_2$ | 32 | 6.8 | N/A |
| $Zr(Y)O_2$ | 50 | 0.7 | 167±113 |
| $Al_2O_3$ | 17 | 3.4 | N/A |
| $Al_2O_3$ | 32 | 2.2 | N/A |
| $Al_2O_3$ | 61 | 2.1 | 141±113 |
| $Zr(Mg)O_2$ | 57 | 1.1 | 144±102 |
| $80\%Zr(Y)O_2$-$20\%Al_2O_3$ | 60 | 0.7 | 183±145 |

## 2.2 Calcium phosphate nanoparticles

In this study we investigated the ability of calcium phosphate nanoparticles functionalized with plasmid DNA (CaP-DNA) to transfect MC3T3-E1 pre-osteoblasts and induce an osteogenic response. The nanoparticles were prepared and characterized by the research group of Prof. Matthias Epple at the University of Duisburg-Essen, Germany. The preparation and characterization procedures are provided in the manuscript, and a general description is also given in appendix II.

For their synthesis, briefly, calcium phosphate nanoparticles were precipitated from aqueous solutions of calcium lactate and diammonium hydrogen phosphate, stabilized by polyethyleneimine (PEI) and loaded with DNA (plasmid BMP-7). In order to synthesize CaP/PEI/DNA/$SiO_2$-SH nanoparticles, a layer of silica was added followed by covalent functionalization of silanol groups, leading to a thiol-terminated surface [6]. The synthesis procedure is schematically shown in Figure 2.1.

The presence of the thiol groups open the possibility for a subsequent covalent attachment of other molecules, e.g. of antibodies [6]. To protect the DNA molecules from the attack of nucleases, the surface of calcium phosphate particles was coated with an additional silica shell.

Overall, nanoparticles of three different compositions were used in this study: phBMP-7 functionalized nanoparticles **CaP/PEI/phBMP-7/$SiO_2$-SH**, pEGFP functionalized nanoparticles **CaP/PEI/pEGFP/$SiO_2$-SH** as control for the transfection experiments, and nanoparticles without DNA **CaP/PEI/$SiO_2$-SH**, as control for induction of osteogenesis.

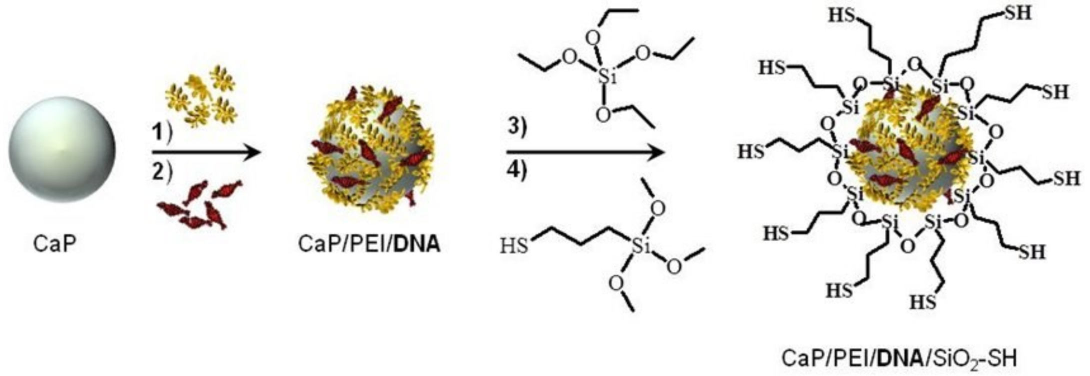

**Figure 2.1. Schematic representation of the synthesis of functionalized calcium phosphate nanoparticles**
(1) Stabilization of nanoparticles with polyethylenimine (PEI) and (2) loading with pDNA (either pEGFP or phBMP-7). (3) Surface modification of DNA-loaded nanoparticles with a silica shell and (4) further functionalization with thiol groups. Calcium phosphate nanoparticles without DNA were obtained by the same preparation route without step 2. Image from D. Kozlova *et al*, 2012 [6].

## 2.3 Cell culture

### 2.3.1 MC3T3-E1 cell line

The understanding of the osteoblast developmental sequence has been greatly facilitated in recent years by the use of the MC3T3-E1 immortalized cell culture system. The

MC3T3-El cell line, derived from newborn murine calvariae, has been reported to display osteoblast-like characteristics after repeated passages and to progress through distinct stages of osteoblast development analogous to *in vivo* bone formation [65, 66].
The undifferentiated pre-osteoblastic cell line MC3T3-E1 is available from ATCC (USA) and DSMZ (Germany). The MC3T3-E1cell line used in this study was obtained from DSMZ (ACC 210, Germany), and has been described to differentiate to osteoblasts and to produce collagen [67]. The cell-line permits independent investigation of undifferentiated osteoblast precursors, osteoblast differentiation, and mature osteoblast function. Under defined culture conditions it can be induced to undergo a developmental sequence leading to the formation of multilayered bone nodules [66]. The presence of ascorbic acid and β-glycerol phosphate is essential for the expression of osteoblast phenotype. The developmental sequence is characterized by an initial phase of active replication of pre-osteoblasts, usually between 1-9 days. As cells attain confluence, they undergo growth arrest. This downregulation of replication is associated with expression of osteoblast characteristics such as the production of alkaline phosphatase and deposition of a collagenous extracellular matrix. After approximately 14 days, mineralization of the extracellular matrix begins, which marks the final phase of osteoblast phenotypic development and leads to eventual formation of multilayered nodules with a bone-like mineralized extracellular matrix. The MC3T3-E1 cell line has become the standard in vitro model of osteogenesis with applications in studies examining including transcriptional regulation, mineralization [68] and tissue engineering [69] [70].

### 2.3.2 Cell culture maintenance

The artificial environment in which the cells are cultured consists of a suitable vessel (culture flasks) or TCPS plates containing a medium that supplies the essential nutrients (amino acids, carbohydrates, vitamins, minerals), growth factors and hormones (if necessary). **Cells are cultured** in an incubator that supplies gases ($CO_2$), and regulates the physicochemical environment (pH, temperature). As most cells, the MC3T3 cells are anchorage dependent and must be cultured while attached to a solid or semi-solid substrate (adherent or monolayer culture). For **subculturing adherent cells**, cells are detached from the surface of the culture flasks by enzymatic means using a dissociation reagent such as trypsin. **For long term storage**, cultured cells are cryopreserved in highly concentrated, low passage seed stocks. This is very important since cell lines in continuous culture are likely to suffer from genetic instability as the passage number increases. Cryopreservation also serves as back-up in cases of microbial contamination of working cultures or equipment failure which can lead to cell culture loss. The best method for cryopreserving cultured cells is storing them in liquid nitrogen in complete medium in the presence of a cryoprotective agent such as dimethylsulfoxide (DMSO). Cryoprotective agents reduce the freezing point of the medium and also allow a slower cooling rate, greatly reducing the risk of ice crystal formation, which can damage cells and cause cell death**.**

**Materials for MC3T3 cell culture:** Minimum essential Eagle's medium (α-MEM), ascorbic acid, β-glycerophosphate, penicillin/streptomycin, fetal bovine serum (FBS), trypsin/EDTA were purchased from Sigma (St. Louis, MO). Tissue Culture Treated Polystyrene (TCPS) plates were obtained from Corning.

**Cryogenic storage of cells:** Seed stocks of the cells at early passages e.g. 4 or 5, were prepared ($10^6$ cells/mL) in 1 mL freezing medium (alpha-MEM with 20% FBS and 10% DMSO) and preserved in cryogenic vials in liquid nitrogen. Before use, cells were quickly thawed in pre-warmed culture media, collected by centrifugation (1200 rpm, 5 min) and re-suspended in fresh, DMSO-free medium before seeding into culture flasks.

**Cell culture maintenance procedure (Figure 2.2):** Cells were cultured in alpha-MEM medium supplemented with 10% fetal bovine serum (FBS) and 1% penicillin/streptomycin (primary medium) and maintained at 37 °C in a humidified atmosphere of 5% $CO_2$ in air. Small flasks (surface area of 25 $cm^2$) were seeded with approximately 2-3 × $10^5$ cells in 8-10 mL culture medium, and large flasks (surface area of 75 $cm^2$) were seeded with approximately 5-6 × $10^5$ cells in 13-15 mL culture medium. Cultures were sub-cultured (1:3) once a week using trypsin/EDTA (1.5 mL for the small and 4.5 mL for the large flasks).

Prior to seeding on the different substrates or TCPS, confluent cells were harvested from culture flasks using trypsin/EDTA and counted on a haemocytometer. Experiments were carried out using cells between passage 5 and 15. The cell seeding procedure onto the different biomaterial substrates is described in Chapters 3 & 4 (for experiments using ceramics) and Chapter 6 (for experiments with nanoparticles).

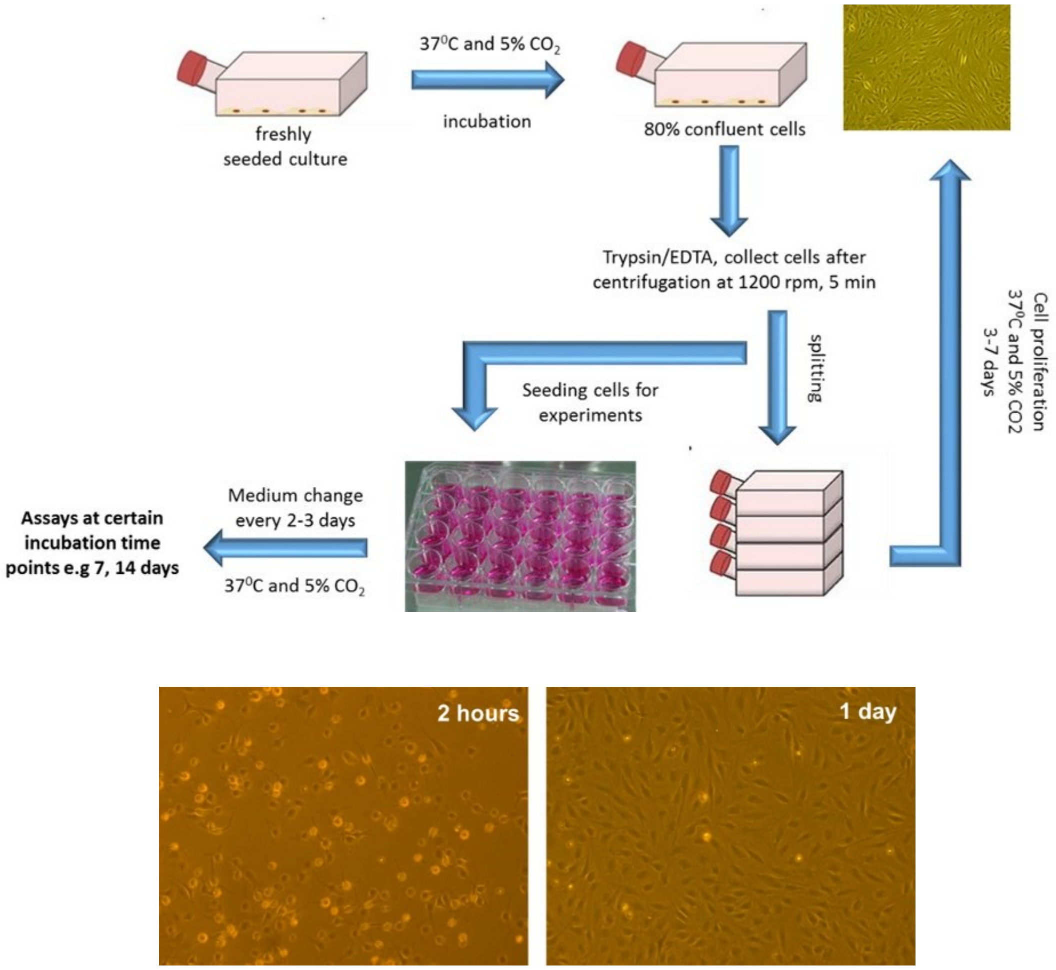

**Figure 2.2. Schematic representation of MC3T3 cell culture maintenance and use for experiments.**
Also, phase contrast microscopy images showing (a) cells adhering on TCPS at 2 hours following seeding (b) fully spread cells covering the surface of TCPS in a monolayer, at one day following seeding (bottom). Magnification at ×10.

## 2.4 *In vitro* biological assays

In vitro biological and osteogenesis assays are routinely used to investigate cell response on biomaterials for bone repair applications as well as to test osteoblastic responses to drugs and hormones. They are performed using primary osteoblasts, osteoblast precursors such as bone marrow-derived mesenchymal stromal cells (BMSCs), or osteoblast cell lines such as the MC3T3-E1 which is the cell-line used throughout this thesis. These cell culture models recapitulate events that occur in bone synthesis allowing the investigation of **cell morphology, viability and proliferation**. Also, cell differentiation is mainly assessed by biochemical methods such as by examining levels of **alkaline phosphatase** activity (an early osteoblast marker), evaluating the assembly of a **collagen (type I)** in the extracellular matrix and the **mineralization of the matrix** which marks the final stage of osteoblast differentiation. Different **markers of osteoblast differentiation** can also be identified and quantified by means of real time quantitative polymerase chain reaction (qPCR). The different assays developed and used in this study are described in this chapter.

### 2.4.1 Cell proliferation assay

The proliferation of MC3T3-E1 pre-osteoblasts was assessed using the PrestoBlue® assay (Invitrogen, CA). PrestoBlue® is a resazurin-based, non-toxic color indicator for viable cells, which is used to assess the metabolic activity of cells (Figure 2.3). Upon its uptake into the cells, the PrestoBlue® reagent becomes reduced to a red product (resorufin), which can be detected spectrophotometrically and provides a measure of cell viability. This assay provides a sensitive and fast tool for assessing cell viability and growth and has the advantage of avoiding the destruction of cells at each assessed time point, since it is a live assay.
(http://www.lifetechnologies.com/uk/en/home/brands/molecular-probes/key-molecular-probes-products/prestoblue-cell-viability-reagent.html, Invitrogen).

For the experiments, cells were removed from the incubator only for the addition of PrestoBlue® reagent at 1:10 diluted in culture media, and were placed back in the incubator for 1h for color development (30 min or 1 hour depending on experiment). They were taken out again for a very short time to evaluate color development at each time point, using a spectrophotometer.

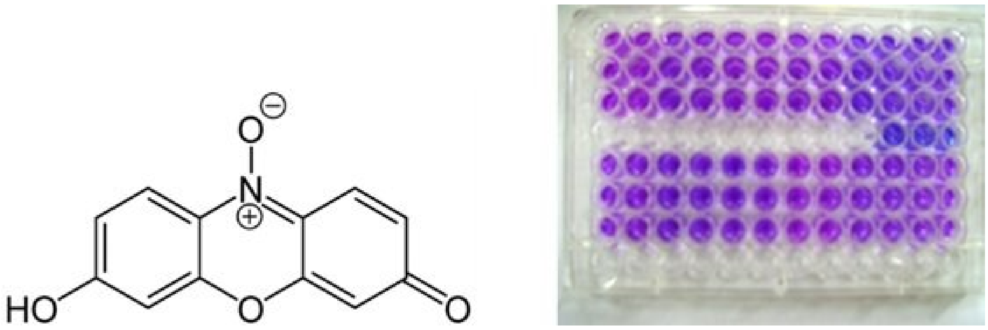

**Figure 2.3. The PrestoBlue® reagent.**
(Left) The chemical structure of PrestoBlue® reagent, a resazurin-based blue dye; (Right) Color change from blue to pink following reduction by the metabolic activity of living cells.

Before assessing how cell growth progresses on the ceramic biomaterials or how transfection with the calcium phosphate nanoparticles affects cellular growth, we performed tests on MC3T3 cells seeded in TCPS plates, to identify the required incubation time of the reagent with the cells that would allow for metabolic activity detection, (between 30 min-2 hours is recommended), without unnecessary longer exposure of live cells to the reagent. As depicted in Figure 2.4, down to approximately 1500 cells/well could be detected in a 96-well plate after 30 min of incubation.

Similar standard curves were prepared for cells seeded in 24- or 6-well plates, either using Abs (570/600 nm) or Fluorescence (544ex/590em) as the mode of detection for the PrestoBlue® reagent color change (not shown). We chose to perform cell proliferation experiments with the minimum 30 min incubation time of cells with the reagent for all experiments, except when cells were directly seeded onto the ceramic materials, where 1 hour incubation times were applied. In this case, we observed that longer incubation time was necessary for color development above background (blank), perhaps because the reagent needed to diffuse inside the porous materials.

| Number of cells/well (x1000) | Abs 570/600nm | | | |
|---|---|---|---|---|
| | 120 min | 90 min | 60 min | 30 min |
| 100 | 1.695 | 1.167 | 0.912 | 0.425 |
| 75 | 1.339 | 1.042 | 0.618 | 0.468 |
| 50 | 0.917 | 0.712 | 0.454 | 0.236 |
| 25 | 0.559 | 0.424 | 0.276 | 0.158 |
| 12.5 | 0.300 | 0.225 | 0.153 | 0.063 |
| 6.25 | 0.152 | 0.117 | 0.084 | 0.046 |
| 3.125 | 0.080 | 0.061 | 0.046 | 0.028 |
| 1.5625 | 0.045 | 0.037 | 0.030 | 0.023 |

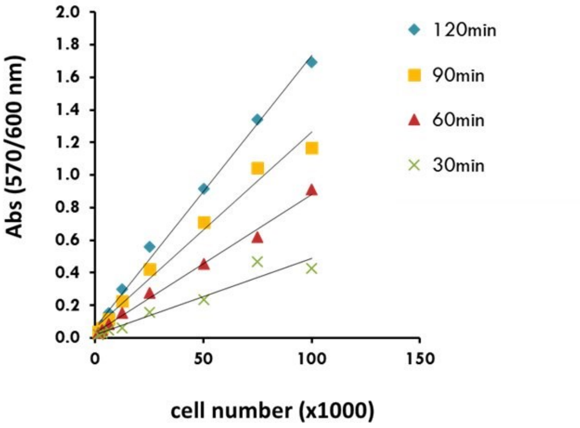

**Figure 2.4. Effect of PrestoBlue® incubation time on signal detection.** Dilutions of MC3T3 cells from 0-100,000 were seeded on TCPS plates and incubated with PrestoBlue® reagent at for 30, 60, 90 or 120 min. The Abs signal increased with incubation time as shown by raw data table (top) and plotted graphs (bottom). Most experiments were performed after 30 or 60 min incubation to avoid overexposure of cells to reagent and the relevant calibration curves were used to express results in cell numbers where necessary. Representative curves for a 96-well plate are shown.

### 2.4.2 Enzyme-Linked Immunosorbent Assay (ELISA)

The enzyme-linked immunosorbent assay (ELISA) is used to determine the presence and concentration of a particular protein in a sample. We have used a sandwich human-BMP7 ELISA to quantify human bone-morphogenetic protein 7 (BMP-7) in MC3T3 culture supernatants following transfection with calcium phosphate nanoparticles carrying plasmid DNA which encoded for hBMP-7. ELISAs were performed in 96-well plates using a hBMP-7 ELISA kit (ab99985) from Abcam (Cambridge, UK). The principle of ELISA is shown in Figure 2.5.

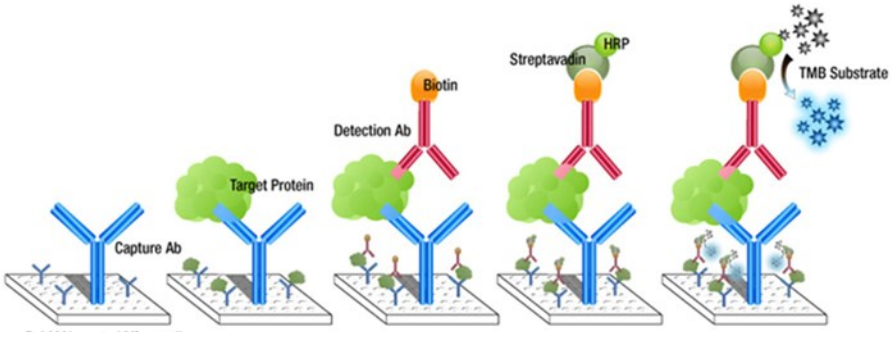

**Figure 2.5. Schematic diagram showing the main steps of a sandwich ELISA.** Image from http://www.epitomics.com/.

During a sandwich ELISA, antigens (hBMP-7 protein) present in the sample attach by specific binding to an immobilized antibody (capture antibody) coated on the plate surface. Then, following washing with a mild detergent solution to remove any proteins or antibodies that are non-specifically bound, a detection antibody (biotinylated anti-human BMP7) is applied over the surface so it can bind to the antigen. After washing away the unbound biotinylated antibody, HRP-conjugated streptavidin is pipetted to the wells and binds to the detection antibody. Then, the enzyme substrate (TMB) is added and the subsequent reaction produces a color change signal, in proportion to the amount of protein (hBMP7) bound. In the final step, the stop solution is added which changes the color (from blue to yellow), and the intensity of the color is measured at 450 nm.

### 2.4.3 Determination of extracellular collagen

Collagen is the major insoluble fibrous protein in the body (making 25% to 35% of the whole-body protein content) and the main component of the extracellular matrix (ECM), forming unique networks in the interstitial spaces between cells. Collagen is found in the form of elongated fibrils of similar structure, mostly in fibrous tissues such as tendons, ligaments and skin. It is also abundant in corneas, cartilage, bones, blood vessels, the gut, intervertebral discs and the dentin in teeth. The fibroblast is the most common cell that creates collagen, but numerous epithelial cells make certain types of collagens, all serving the same purpose, to help tissues withstand stretching [71].

Structurally, the collagen superfamily is highly complex and shows a remarkable diversity in molecular and supramolecular organization, tissue distribution and function. A common feature of all collagens is a triple-helical domain (Figure 2.6), which generally consists of two identical chains ($\alpha_1$) and an additional chain that differs slightly in its chemical composition ($\alpha_2$). The amino acid composition of collagen is atypical for proteins, particularly with respect to its high hydroxyproline content (around 13.5% of its amino acid composition). The most common motifs in the amino acid sequence of collagen are [Glycine-Proline-X]n and [Glycine-X-Hydroxyproline]n, where X is any amino acid other than glycine, proline or hydroxyproline [72].

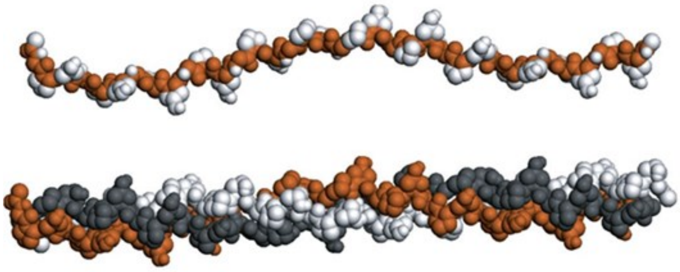

**Figure 2.6. The collagen triple helix.**
The single polypeptide chain folded into a helix with 3.3 residues apart, (top) Space filling model of the collagen triple helix (tropocollagen) (bottom). Image from Molecular Cell Biology, Sixth Edition, 2008.

Fibrillar collagens traditionally have been classified into major (types I, II, and III) and minor (types V and XI) collagen types based on their relative abundance in connective tissues. We now know that the superfamily of collagens includes more than 20 types with at least 38 distinct polypeptide chains, as well as more than 15 additional proteins that have collagen-like domains [72]. However, 80 – 90 % of the collagen in the body consists of types I, II, and III. Among these, collagen type I is the main component of the organic part of bone, also comprising the main type of collagen in the body. The collagen type I molecule contains two $\alpha_1$(I) and one $\alpha_2$(I) chains, forming 300nm long fibrils. The unique properties of each type of collagen are due mainly to segments that interrupt the triple helix and that fold into other kinds of three-dimensional structures [71].

The different types of collagens are expressed in unique spatiotemporal patterns during mammalian development, ultimately providing mechanical strength to skin, bone, and other tissues [73]. It has been shown that aberrations in collagen biosynthesis, or mutations in collagen genes, can result in various bone disorders e.g. certain mutations in the $\alpha_1$(I) or $\alpha_2$(I) genes lead to *osteogenesis imperfecta,* or brittle-bone disease.

In terms of biochemical properties, collagen types can be categorized in two biochemical groups: 1) acid soluble and 2) neutral-salt soluble or extractable collagen. Acid soluble collagen is composed of mature fibers with many intramolecular cross-links, while neutral-salt soluble collagen is thought to be an immature precursor (with fewer cross-links) to mature collagen [74].

Collagen accumulation in the extracellular environment of the cells is a hallmark of osteoblast differentiation. It takes place during an intermediate phase in osteoblast differentiation, and contributes to the formation of extracellular matrix in which mineralization can occur [75]. To investigate if the ceramic biomaterials interfered with collagen production, we quantified levels of secreted collagen in cell culture supernatants. For this purpose, a colorimetric assay was used, based on the observation that the Sirius red dye in acid solution, selectively binds to the [Gly-X-Y]n helical structure of mammalian collagen. The assay was modified from similar assays described for cell culture supernatants [76] as well as from information on the commercially available collagen assay, Sircol Dye assay (Biocolor, UK).

Sirius red staining of collagen has been used for many years. It was first described by Junqueira et al. in 1979 [77] and has since been used to assess collagen in tissue sections as well as cell culture [78]. Sirius Red (also known as Direct Red 80) is a strong anionic dye, which stains collagen by reacting, via its sulphonic acid groups, with basic groups present in the collagen molecule (Figure 2.7). The elongated dye molecules are attached to the collagen fiber in such a way that their long axes are parallel.

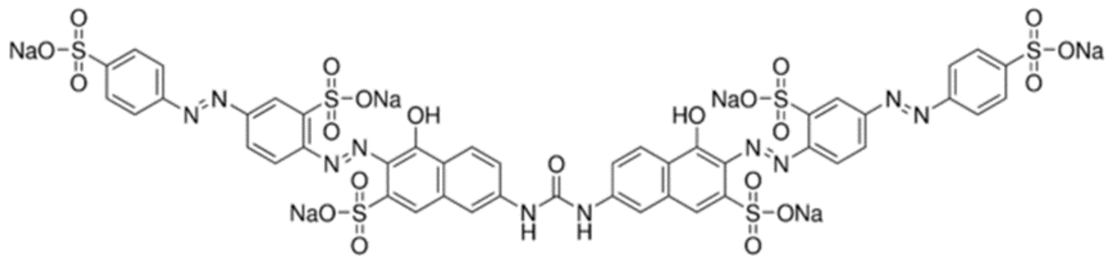

**Figure 2.7. The molecular structure of the Sirius Red dye.**
The elongated dye molecules align parallel to the collagen molecule, interacting with basic groups in the polypeptide chain.

The Sirius Red dye does not discriminate between collagen types, and has been reported to bind strongly to collagen types I and III whereas collagen type IV exhibited only low staining. Thermal denaturation (> $40^0$C) of collagen decreases dye binding. Non-mammalian collagens bind less dye, due in part to lower denaturation temperatures and the reduced occurrence of hydroxyproline residues. Other extracellular materials such as fibronectin, chondroitin sulfate, dermatan sulfate, and amyloid beta were found negative [78].

The colorimetric plate assay based on Sirius Red binding of functional collagen allows for rapid assessment of collagen content in complex protein solutions. However, one major problem with the assay is that it appears to over-estimate the amount of collagen in a sample due to interference from non-collagenous proteins e.g. serum. Therefore, despite being the fastest and simplest colorimetric method for collagen, modifications of the commercial Sircol assay have been suggested [79].

One way to overcome interference from serum in cell culture supernatants is to dilute the supernatant with water so that serum concentration is kept below 5 %, before the assay is performed. Another alternative way would be to selectively remove the bulk of the serum albumin from the test sample by affinity chromatography (Blue-Sepharose CL-6B) or concentrate collagen by salt precipitation (e.g. NaCl 4M) and re-solubilize in acetic acid (0.5M).

In our protocol, we chose to dilute samples down to 2.5 % serum before the assay, and by doing this we have achieved to minimize interference from serum. Blank samples (medium alone) were assayed alongside cell culture supernatants and served as background, deducted from each sample's optical density before concentration could be determined. Briefly, for assessing collagen in cell culture supernatants, the diluted cell culture supernatant sample is solubilized in acetic acid (0.5 M). Following binding of the Sirius Red dye, the collagen-dye complex precipitates, resulting in a colored pellet. The precipitate is solubilized in alkaline solution (0.5 M NaOH) and the collagen content of each duplicate is measured by an optical density analysis at 530 nm (the exact details of the protocol are provided in Chapter 4). The amount of collagen is then calculated based on a linear standard curve constructed from previously known concentrations of type I collagen (Sigma), used as the collagen standard control in the Sirius Red staining procedure. The collagen standard curve is shown in Figure 2.8. Examination of the standard curve, reveals that for samples with collagen concentrations of ~ 8 µg/mL the absorbance reading is too close to the reagent blank value to provide confidence in the collagen value obtained.

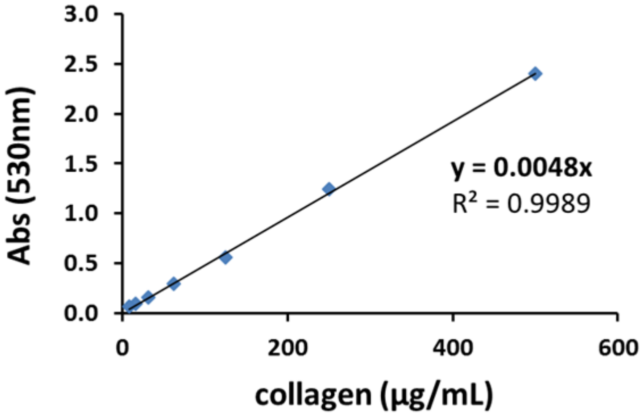

**Figure 2.8. Calibration curve for Sirius Red dye bound by acetic acid soluble type I collagen.**
The graph was prepared using dilutions of the collagen standard (8-500 µg/mL) according to the assay procedure described in Chapter 4.

The diluted analyzed test samples (cell culture supernatants), had collagen concentrations ~ 30-200 µg/mL, therefore the detection limit was not an issue. However, occasionally, we observed high variability in the absorbance readings within the same test sample, therefore it is recommended to analyze each sample at least in duplicates and take at least two absorbance readings for each of the duplicates.

### 2.4.4 Alkaline phosphatase activity assay

Alkaline phosphatase, (ALP) [phosphate-monoester phosphohydrolase (alkaline optimum); EC 3.1.3.1] is a metalloenzyme that exists as several tissue-specific isozymes encoded by separate genes. Humans have four *Alp* genes corresponding to intestinal, placental, placental-like and liver/bone/kidney (tissue nonspecific; TNAP) gene products. Mutations in the *TNAP* gene can lead to Hypophosphatasia, a rare inborn disease that is characterized by defective bone mineralization. On a cellular level, ALPs are membrane bound glycoproteins localized to the outside of the plasma membrane and of the membrane of matrix vesicles. They are attached to the membrane by a glycophosphatidylinositol (GPI) anchor, and are found in membrane microdomains known as rafts [80].

ALPs catalyze the hydrolysis of phosphate esters, $R-O-PO_3$, with little regard to the identity of the 'R' group in a mechanism that involves the formation of a serine phosphate at the active site which reacts with water at alkaline pH to release inorganic phosphate from the enzyme. In general, ALPs are homodimeric enzymes and each catalytic site contains three metal ions, i.e., two Zn and one Mg, necessary for enzymatic activity. The structure of human placental alkaline phosphatase (PLAP), to which TNAP is 74% homologous, is shown in Figure 2.9.

In bone, ALP is highly expressed in mineralized tissue cells and its role as a marker for osteogenic activity has been consistently solidified by numerous reports [80]. Thus, in osteogenesis studies, measurement of increased ALP expression either enzymatically, histochemically or at the mRNA level is considered as a reliable indication of the osteoblastic phenotype and a good predictor of tissue mineralization. While, it is less clear why ALP levels are elevated in mineralized tissue, the enzyme appears to act to increase the local concentration of inorganic phosphate (a concept known as the 'booster hypothesis') and simultaneously to decrease the concentration of extracellular pyrophosphate, an inhibitor of mineral formation.

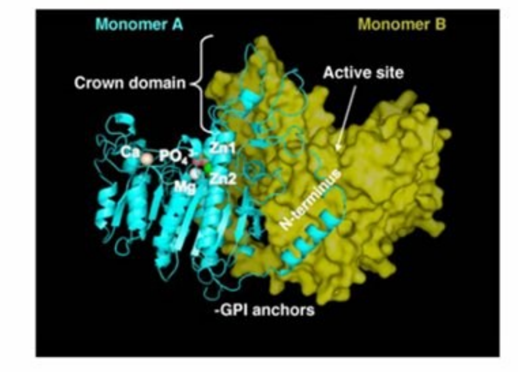

**Figure 2.9. Three dimensional structure of placental ALP.**
Monomer A is shown in ribbon representation and in cyan, while monomer B is shown in surface representation in yellow. Indicated are the active site metals, the crown domain and the amino terminal arm. The relative location of the GPI anchor is also indicated. Image from [81].

As ALP is one of the early markers of osteoblast differentiation, we monitored ALP levels in whole cell lysates during the course of the experiements using a biochemical assay. The assay uses *p*-nitrophenyl phosphate (pNPP) as a phosphatase substrate which turns yellow ($\lambda_{max}$= 405 nm) when dephosphorylated by ALP (Figure 2.10).

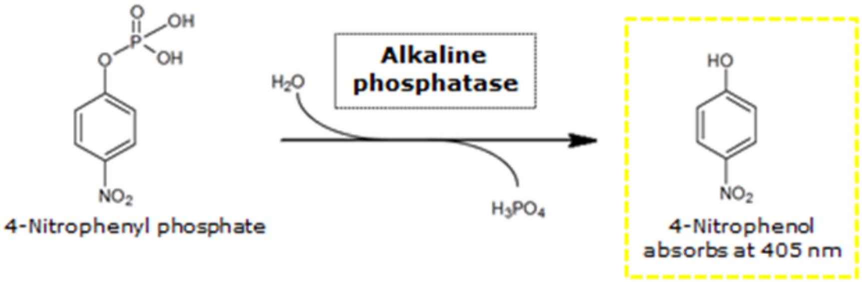

**Figure 2.10. Alkaline phosphatase catalysis of *p*-nitrophenyl phosphate.**
A yellow product is released, which can be directly related to enzyme activity in the test samples.

The method we used was optimized for MC3T3 cells used in this study, based on several protocols reported in literature. Briefly, cells are washed in PBS and lysed using 0.1% Triton X-100 followed by freezing and thawing cycles. The ALP substrate in alkaline solution is added to the cell lysate and the mixture is incubated at 37 °C for 1 hour, for the enzymatic reaction to take place. After stopping the reaction with 1N NaOH, the color change was measured spectrophotometrically. A calibration curve constructed of known concentrations of *p*-nitrophenol was used to correlate Abs readings to product concentration. ALP activity for each well was calculated using the equation [units = nmol *p*-nitrophenol/min]. Finally, ALP levels were normalized to cellular protein levels (Bradford assay) at the end of the experiment and expressed as specific activity. Details of the assay are given in Chapter 4.

### 2.4.5 Calcium biomineralization assay

Alizarin Red is an organic dye used which was used in a biochemical assay to determine, either qualitatively by microscopy or quantitatively by colorimetry, the presence of calcific deposition by MC3T3 pre-osteoblastic cells. Alizarin Red S (ARS) staining has been used for decades to evaluate calcium-rich deposits by cells in culture [82]. It has been used in studies involving bone growth, osteoporosis, bone marrow, calcium deposits in the vascular system, cellular signaling, gene expression, tissue engineering, and mesenchymal stem cells. Alizarin Red staining is considered a marker of matrix mineralization which marks a crucial step towards the formation of calcified extracellular matrix in bone formation. Free (ionic) calcium forms precipitates with alizarin, and tissues containing calcium stain red immediately when immersed in alizarin. Thus, both pure calcium and calcium in bones and other tissues can be stained. After staining, the dye can be extracted from the stained monolayer and assayed. Extraction is performed with either acetic acid or cetylpyridinium chloride (CPC) and the color in measured spectrophotometrically. The chemical structure of alizarin red (1, 2-dihydroxyanthraquinone) is shown in Figure 2.11. It can be viewed as being derived from anthraquinone by replacement of two neighboring hydrogen atoms (H) by hydroxyl groups (-OH). As a chelating agent, it forms an orange-red precipitate with calcium.

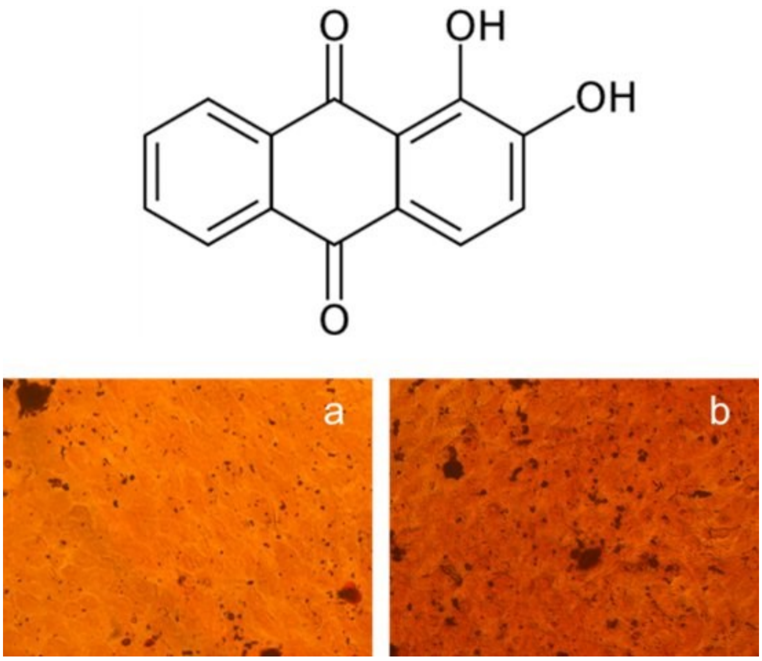

**Figure 2.11. Alizarin Red S for detection of calcium mineralization.**
The molecular structure of Alizarin Red S or 1,2-dihydroxyanthraquinone (Top). More stained mineral appears in MC3T3 cells following treatment with osteogenic medium (a) than untreated cells (b) after 21 days of culture (Bottom). Magnification × 10.

The color and intensity of ARS depends on the cell source as well as culture conditions e.g. it has been reported that hMSCs treated with osteogenic substrate and dexamethasone produced significantly more stained mineral than untreated cells [83]. Similarly we have observed that generally MC3T3 pre-osteoblastic cells produce more stained mineral under osteogenic conditions (in the absence of dexamethasone) than untreated cells, as shown in Figure 2.11.

### 2.4.6 Quantitative real time PCR (qPCR)

Polymerase chain reaction (PCR) is a biochemical method for exponentially amplifying specific DNA sequences from relatively small amounts of starting material by *in vitro* DNA synthesis. This technology mimics DNA replication, using thermophilic T*aq* DNA polymerase as the key enzyme and was developed by Katy Mullis at Cetus Corporation in Emery Ville, California in 1985. Since then, it has been automated and takes place in a thermal cycler machine. The steps involved in PCR are:

1. **Melting of the target DNA:** denaturing of the DNA duplex at a high temperature (at 95 °C) to yield single stranded DNA.
2. **Annealing:** primers anneal to the single stranded target DNA sequence (at ~ 55 °C).
3. **Elongation or extension:** DNA polymerase extends the primers by adding dNTPs to the phosphate backbone.

These steps complete one PCR cycle, and the cycle repeats until a sufficient DNA concentration is reached (Figure 2.12). After 21 cycles, one molecule of DNA can be amplified to over a one million copies.

Unlike in standard PCR, where the product of the reaction is detected at its end, quantitative, or real time, PCR (qPCR) has the advantage of detecting the amount of DNA formed after each cycle. Real-time quantitative qPCR is a powerful technique capable of accurately quantitating mRNA expression levels over a large dynamic range and is the most widely used method for studying quantitative gene expression [84]

DNA detection is achieved with either:

1. fluorescent dyes that intercalate with any double-stranded DNA. The fluorescent signal of the intercalated dye is several orders of magnitude higher than that of unbound dye. The most common fluorophore used is SYBR® Green.
2. fluorescently-tagged oligonucleotide probes which permit detection only after hybridisation of the probe with its complementary sequence to quantify messenger RNA (mRNA).

The advent of quantitative real-time qPCR techniques for the measurement of gene expression has allowed the accurate determination of the expression levels of target genes in cells and tissues. qPCR is used for the detection of differential expression of genes between different tissue types or between normal and disease states and can provide leads for novel therapeutic approaches for disease treatment. It is also useful for the investigation of viral load, pathogen detection, as well as numerous other applications.
In our experiments, qPCR was used to study gene expression of MC3T3 cells cultured on ceramic biomaterials and following transfection with DNA-carrying calcium phosphate nanoparticles.

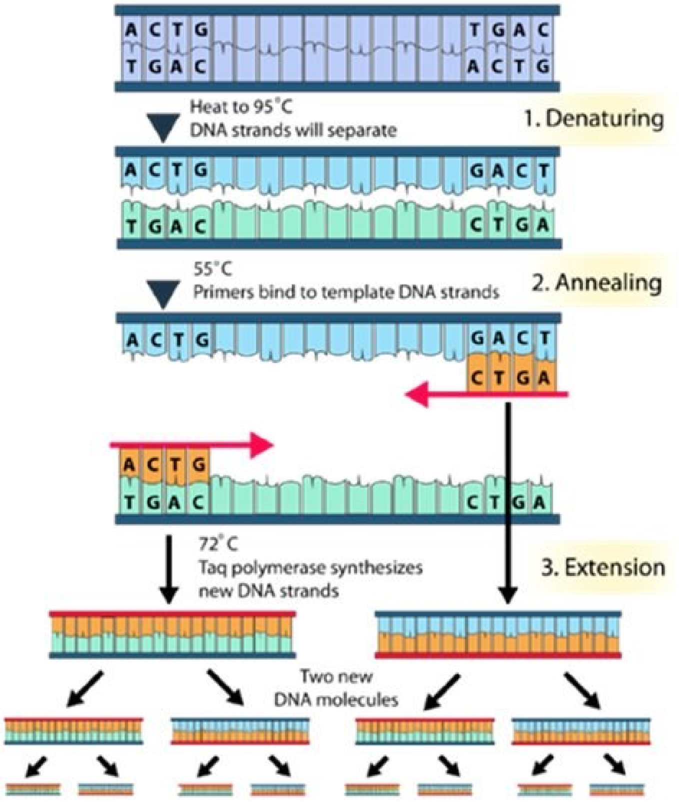

**Figure 2.12. The principle of DNA amplification in PCR.**
DNA polymerase uses the DNA target amplicon as a template to synthesize more DNA copies. Image reproduced from:
http://scienceinfoworld.blogspot.co.uk/2012/11/polymerase-chain-reaction-pcr.html

Plasmid constructs for each target gene were prepared to serve as reference standards, and the detection was achieved using SYBR Green dye as the fluorescent double-stranded DNA (dsDNA) binding dye. As the PCR reaction proceeds, at each round of amplification SYBR® Green dye binds to dsDNA as it polymerizes, resulting in an increase in the level of fluorescence at the end of each extension step. The quantity of dsDNA product in the reaction is proportional to the amount of fluorescence.

The necessary steps taken for setting up and running qPCR experiments are described in the following paragraphs.

### Primer design and specificity control for qPCR

The primer nucleotides sequences for qPCR for the mus musculus species, were designed using the online **NCBI tool Primer BLAST** (http://www.ncbi.nlm.nih.gov/nuccore/) in addition to references in previously published work [62, 68]. Primer pair specificity was checked using the Reference Sequence (Refseq) mRNA sequence from the organism (mus musculus) and the Mega 5 free software for manual sequence alignment. Overall the aim was to obtain primers which did not bind to other mus musculus DNA sequences other than the gene of interest, have low self-complementarity in order to decrease the possibility of primer-dimer formation and have an amplicon size < 200 bp for efficient amplification in real-time RT-PCR. Also, we aimed for a minimum of 57 °C and a maximum of 63 °C melting temperatures, with a maximum difference of 3 °C in the Tm's of the two primers. The selected genes and their primer nucleotide sequences are shown in Table 2.2.

In order to check the specificity of the designed primers, total RNA from MC3T3 cell cultures (grown in osteogenic media so as to enhance expression of osteogenic markers) was extracted with the phenol containing reagent Trizol® according to the manufacturer (Life technologies), and was used to prepare first strand cDNA templates using Superscript II reverse transcriptase (Invitrogen) and the reverse primer of each primer set (Table 2.2).

PCR amplification was carried out using *Taq* DNA Polymerase and the size of the PCR amplicons was confirmed on 2% agarose gel electrophoresis as shown in Figure 2.13.

**Table 2.2. Oligonucleotide Sequences of forward and reverse Primers (Mus musculus) used for real-time PCR**

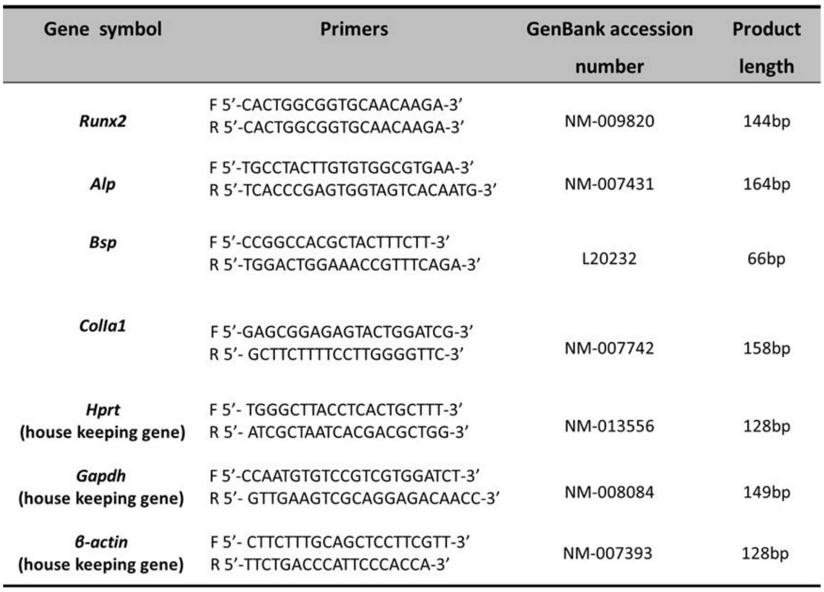

| Gene symbol | Primers | GenBank accession number | Product length |
|---|---|---|---|
| ***Runx2*** | F 5'-CACTGGCGGTGCAACAAGA-3'<br>R 5'-CACTGGCGGTGCAACAAGA-3' | NM-009820 | 144bp |
| ***Alp*** | F 5'-TGCCTACTTGTGTGGCGTGAA-3'<br>R 5'-TCACCCGAGTGGTAGTCACAATG-3' | NM-007431 | 164bp |
| ***Bsp*** | F 5'-CCGGCCACGCTACTTTCTT-3'<br>R 5'-TGGACTGGAAACCGTTTCAGA-3' | L20232 | 66bp |
| ***Colla1*** | F 5'-GAGCGGAGAGTACTGGATCG-3'<br>R 5'- GCTTCTTTTCCTTGGGGTTC-3' | NM-007742 | 158bp |
| ***Hprt***<br>**(house keeping gene)** | F 5'- TGGGCTTACCTCACTGCTTT-3'<br>R 5'- ATCGCTAATCACGACGCTGG-3' | NM-013556 | 128bp |
| ***Gapdh***<br>**(house keeping gene)** | F 5'-CCAATGTGTCCGTCGTGGATCT-3'<br>R 5'- GTTGAAGTCGCAGGAGACAACC-3' | NM-008084 | 149bp |
| ***β-actin***<br>**(house keeping gene)** | F 5'- CTTCTTTGCAGCTCCTTCGTT-3'<br>R 5'-TTCTGACCCATTCCCACCA-3' | NM-007393 | 128bp |

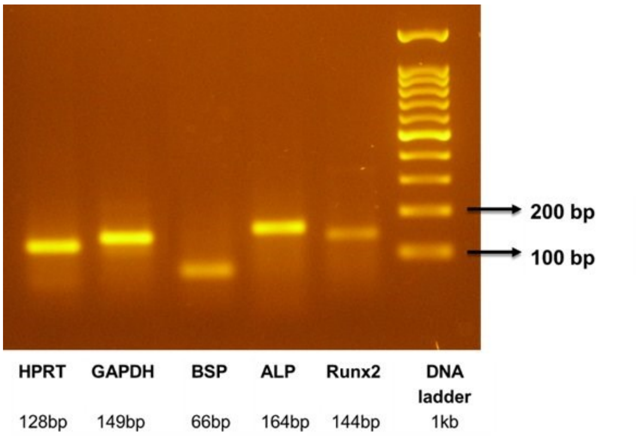

**Figure 2.13. The expected size of the PCR amplicons/products for each gene was confirmed on 2% agarose gel electrophoresis stained with ethidium bromide.**

### Construction of plasmid standards for qPCR

Following the confirmation of primer specificity and product length, plasmid constructs with the pGEM-Teasy vector (3015bp) (Promega, USA), depicted in Figure 2.14, were prepared to serve as external homologous DNA standards of known concentrations and to produce standard curves for each specific gene target as well as the housekeeping genes. The plasmid constructs carrying the PCR amplicons for the specific gene targets were designed using the Vector NTI software (Life Technologies) and are shown in Figure 2.15-Figure 2.17.

Using the Vector NTI software, as well as the online tool NEB cutter (http://nc2.neb.com/NEBcutter2/), we have examined the available restriction enzymes' sites on the DNA sequence of each product. The EcoRI restriction enzyme which cleaves the plasmid before and after the DNA insert sequence was chosen as the most appropriate, to confirm the product length of each target gene using agarose gel electrophoresis, following incubation of the plasmid with the enzyme and its cleavage, according to the manufacturer (New England Biolabs, USA).

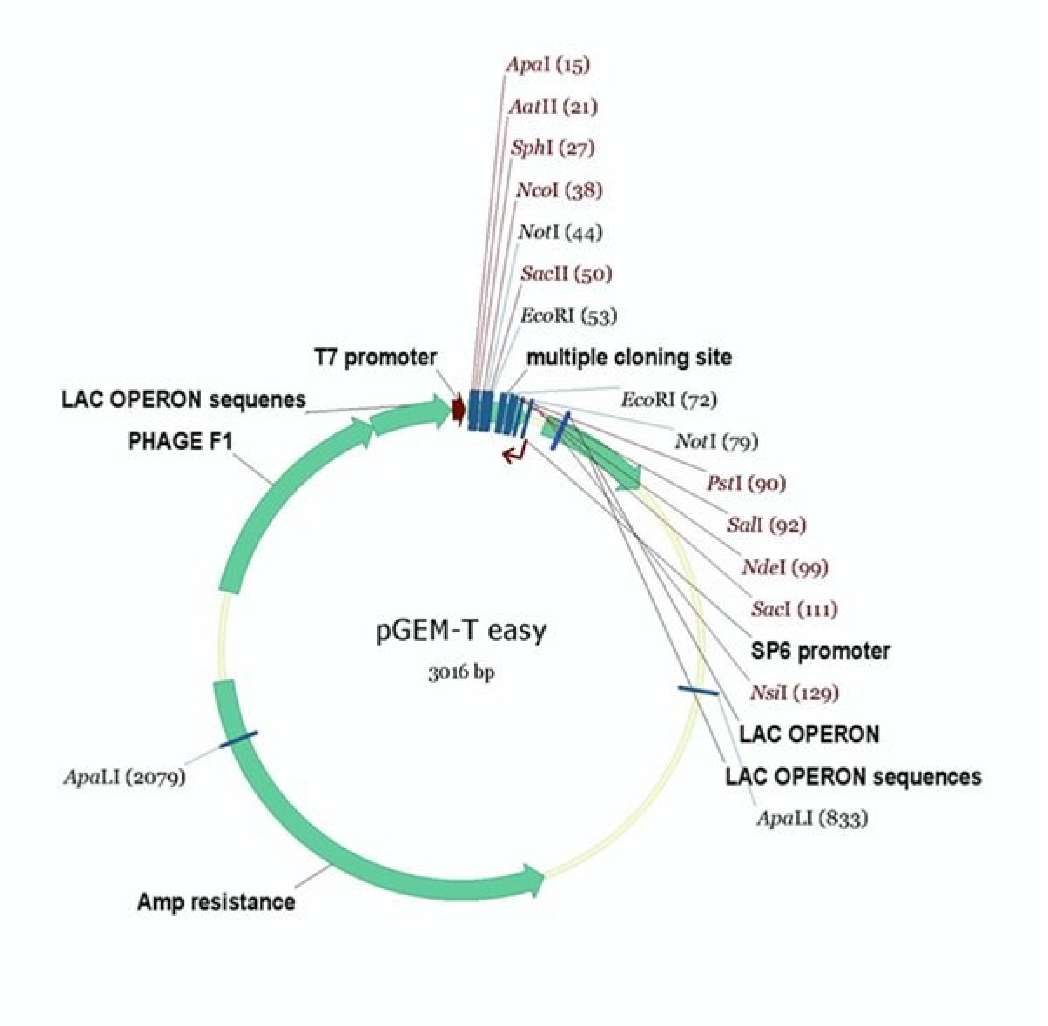

**Figure 2.14. The pGEM®-T Easy vector.**
The map shows some reference sequences, the multiple cloning site in which insert DNA is cloned, as well as the several restriction enzyme sites available.

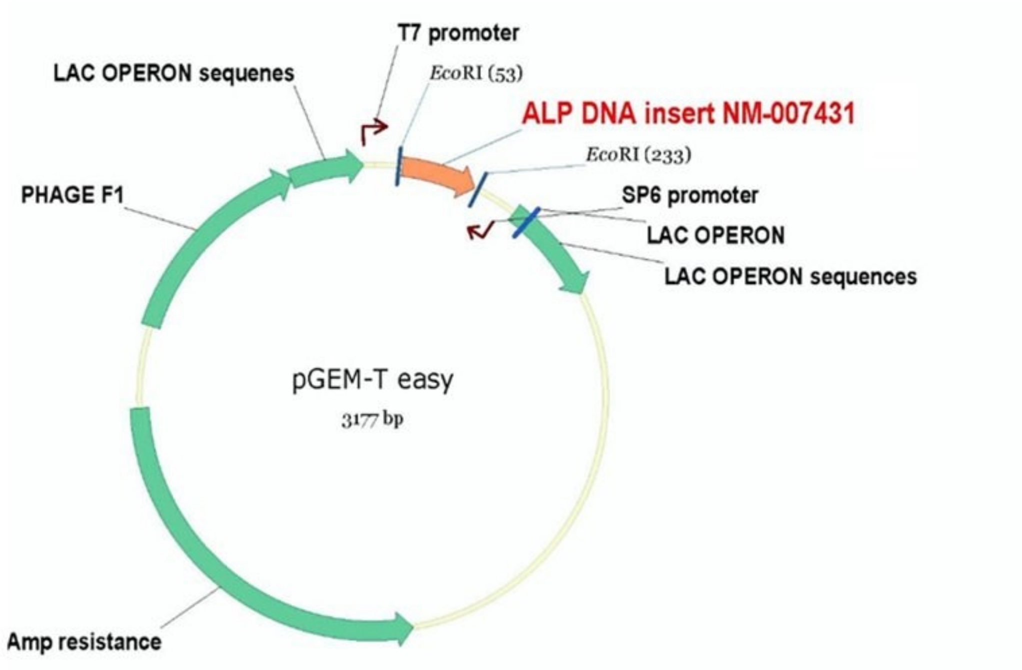

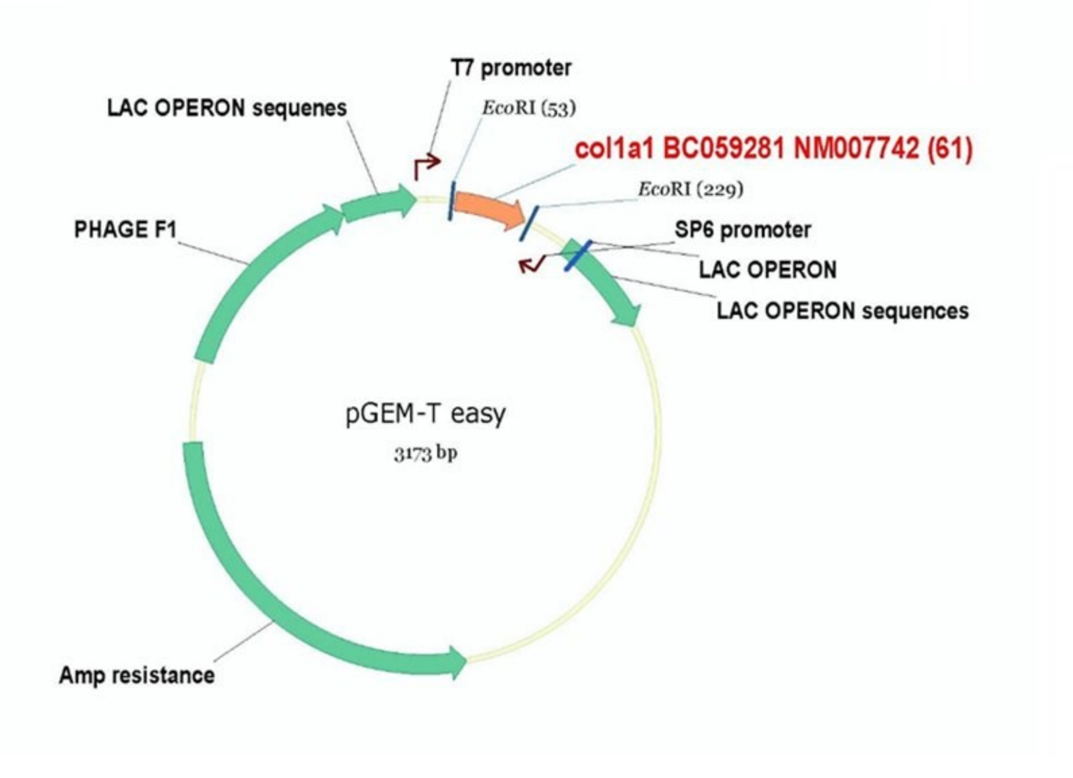

**Figure 2.15. The pGEM®-T Easy vector map showing the ligation of mus musculus (top) *Alp* or (bottom) *ColIα1*, PCR products into the plasmid's multiple cloning site.**

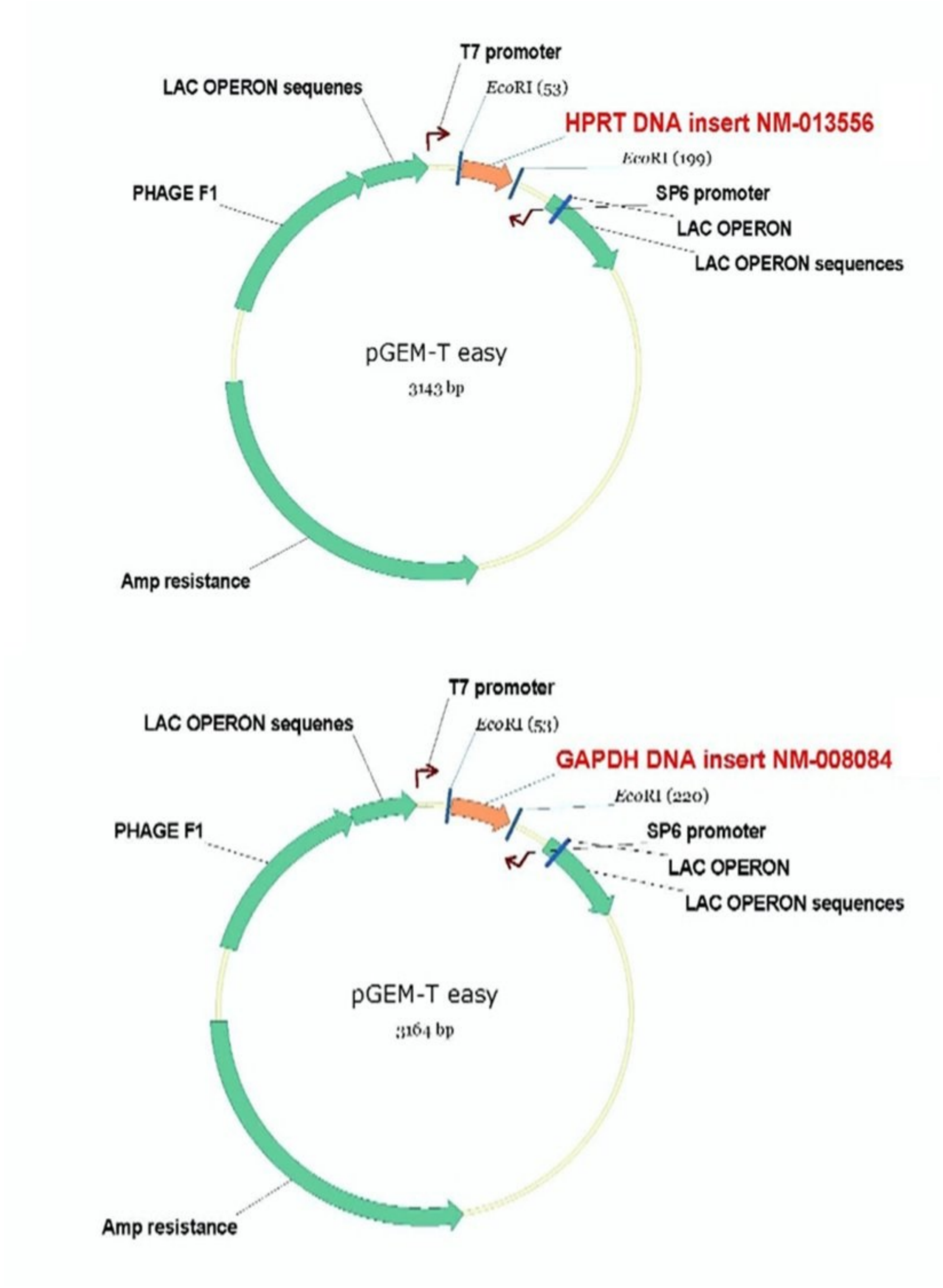

**Figure 2.16. The pGEM®-T Easy vector map showing the ligation of mus musculus (top) *Hprt* or (bottom) *Gapdh*, PCR products into the plasmid's multiple cloning site.**

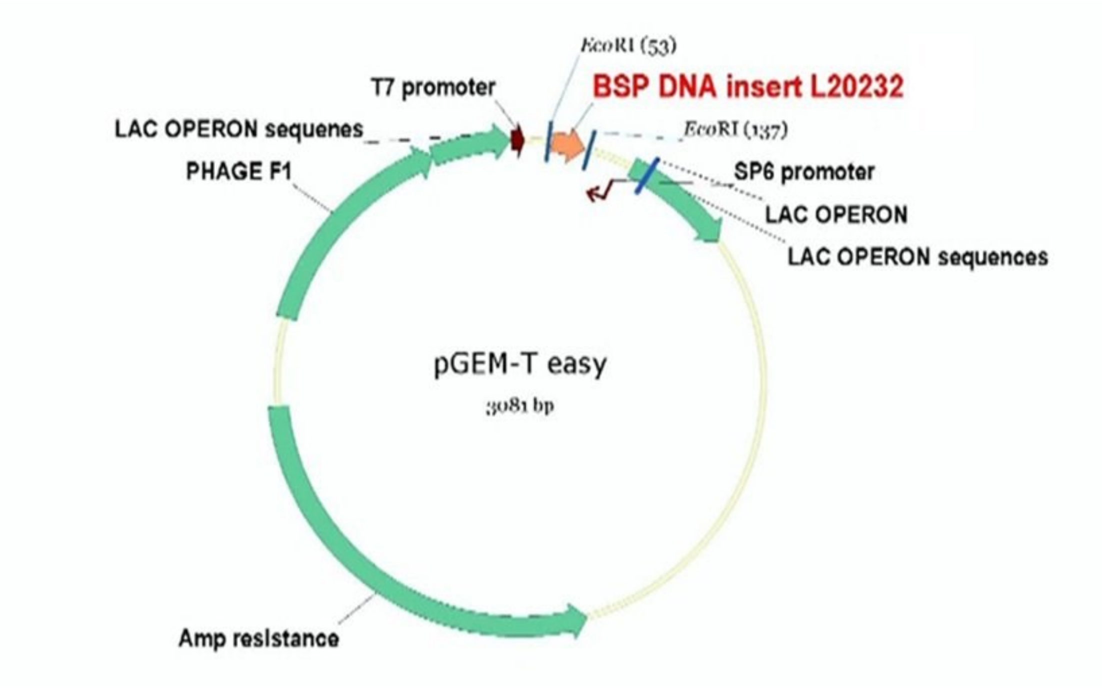

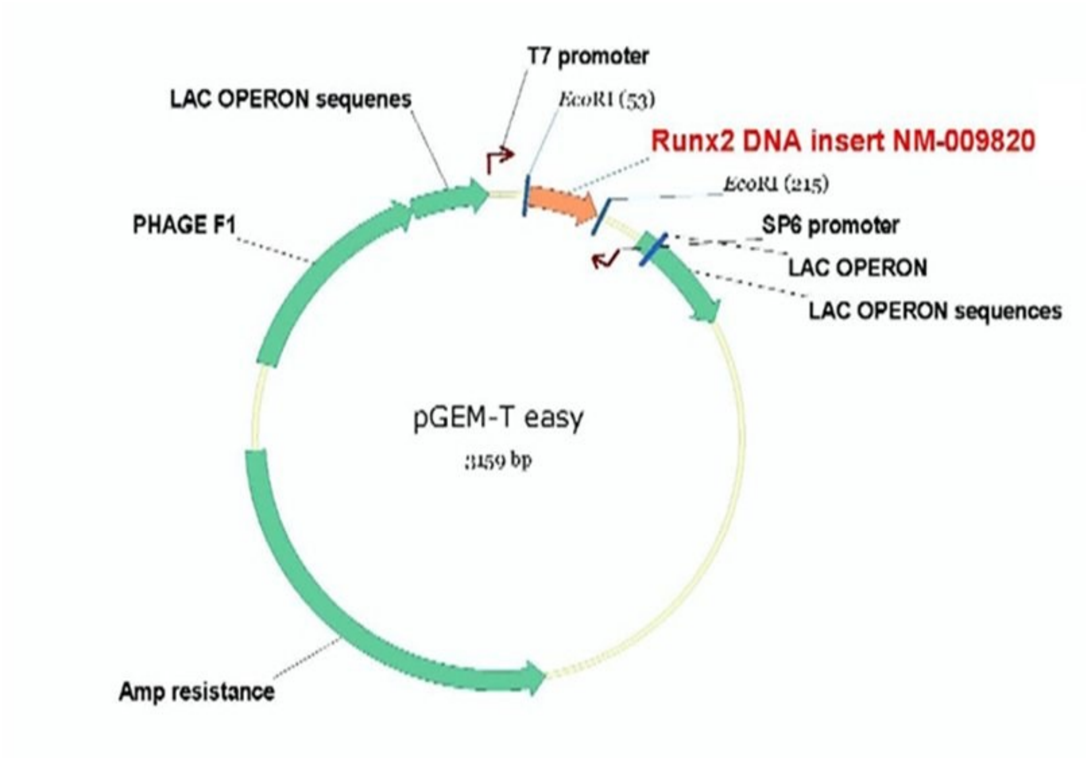

**Figure 2.17. The pGEM®-T Easy vector map showing the ligation of mus musculus (top) *Bsp* or (bottom) *Runx2*, PCR products into the plasmid's multiple cloning site.**

The experimental procedure which led to the construction of the different plasmid standards for qPCR is summarized below:

The PCR amplicons prepared as described above, were purified after extraction from agarose gels using the Nucleospin Gel and PCR Clean-up kit (Macherey-Nagel, Germany) and cloned into the pGEM-Teasy vector (3015bp) system according to the manufacturer (Promega, USA).

Reference plasmids were propagated in *Escherichia coli* DH5a or Mach1 (kindly provided by the laboratories of Prof. Kalandidis and Prof. Mitraki, Crete) and positive clones were randomly picked based on blue/white selection. *E. coli* cells transformed with an insert-containing plasmid produce white colonies, while those containing empty or re-ligated vector generally produce blue colonies. This happens as only in the absence of insert, are bacteria capable of producing functional β-galactosidase which cleaves the substrate X-Gal (5-bromo-4-chloro-3-indolyl-β-D-galactopyranoside), creating blue colonies when grown on indicator plates containing IPTG and X-Gal.

Plasmid DNA was isolated from 3-4 ml of overnight bacterial cultures using the Nucleospin Plasmid Miniprep kit (Macherey-Nagel) to avoid contamination by bacterial RNA that may occur with a non-column-based plasmid isolation method (home-made miniprep protocols have also been tested).

The presence of the correct insert in all plasmid samples was confirmed with 2% agarose gel electrophoresis, following enzymatic digestion with the EcoRI restriction endonucleases (New England Biolabs) and is shown in Figure 2.18. All enzymatic reactions were carried with 2.5 U of corresponding enzyme at 37°C for 30 min. Different ligation ratios were tested in order to achieve successful cloning of all PCR products.

Two plasmid clones from each gene were sequenced (CEMIA, Greece) and the results were confirmed to be the expected following alignment of the DNA sequences with BLAST:

http://blast.ncbi.nlm.nih.gov/Blast.cgi?PAGE_TYPE=BlastSearch&BLAST_SPEC=blast2seq&LINK_LOC=align2seq.

Finally, the optical density at $OD_{260}$ was measured in triplicates using the NanoDrop ND2000 spectrophotometer (ThermoScientific, USA). Plasmid DNA was prepared in dilution series ($10^{-2}$ up to $10^{-8}$M) for qPCR, and stored at −80°C.

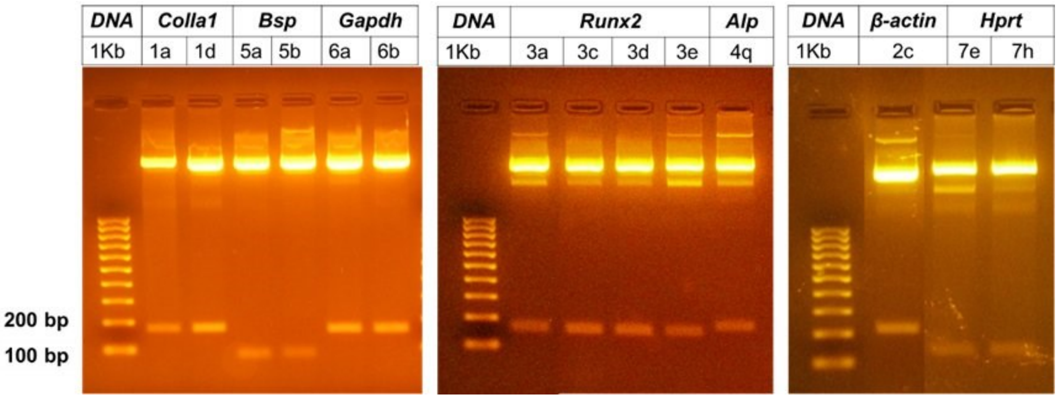

**Figure 2.18. Verification of DNA inserts in plasmids by agarose gel electrophoresis.**
The presence of the expected DNA inserts in plasmids isolated from various clones (shown in numbers e.g. 1a, 1d etc.) from selected *E. coli* colonies after transformation was confirmed with 2% agarose gel electrophoresis, following enzymatic digestion with the EcoRI restriction endonuclease.

### RNA extraction and quantitative real-time PCR (qPCR)

In order to assess gene expression, total RNA from MC3T3 cells under investigation was extracted using the Nucleospin RNA isolation kit (Macherey-Nagel, Germany) according to the manufacturer's protocol. Total RNA quantity and purity were determined by UV spectrometry at 260 and 280 nm using a NanoDrop2000 spectrophotometer (Thermo Scientific, USA), whereas its integrity was assessed on a denaturing 1% agarose gel electrophoresis. The image if Figure 2.19 shows total RNA from various MC3T3 cell samples after electrophoresis. Intact total RNA has a sharp, clear 28S and 18S rRNA bands in eukaryotic samples. The 28S rRNA band should be approximately twice as intense as the 18S rRNA band. This 2:1 ratio (28S:18S) is a good indication that the RNA is completely intact.

Partially degraded RNA will have a smeared appearance, will lack the sharp rRNA bands, or will not exhibit the 2:1 ratio of high quality RNA. Completely degraded RNA will appear as a very low molecular weight smear. When Trizol was used to extract RNA from cells grown on ceramic biomaterials or following transfection with the nanoparticles in this study, we observed that it was not possible to obtain intact RNA (data not shown). We speculate that this was due to the fact that divalent cationic e.g. calcium or zirconia and magnesium in these samples, formed complexes with the negatively charged nucleic acids upon cell lysis, and prevented RNA isolation using non-column purification with Trizol. Cationic $Ca^{2+}$ and other divalent metal ions such as $Mg^{2+}$, $Ba^{2+}$ and $Mn^{2+}$ are known to form ionic complexes with helical phosphates [85]. Therefore, we performed all RNA isolation procedures using the Nucleospin RNA isolation kit, which resulted in high quality RNA samples, necessary for qPCR.

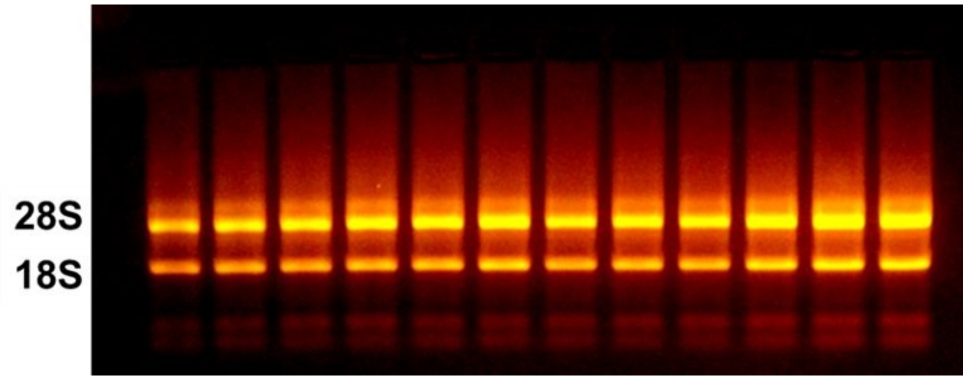

**Figure 2.19. Integrity of RNA isolated from cell cultures treated under different conditions.**
One µg of total RNA extracted from different cell samples were run on a 1% denaturing agarose gel. The 18S and 28S ribosomal RNA bands are clearly visible, confirming that the RNA samples are intact.

Real-time quantitative polymerase chain reaction (qPCR) analysis was performed on a CFX Connect Bio-Rad real-time PCR system (Bio-Rad, USA) using KAPA SYBR green Fast Master Mix (KAPA Biosystems, USA) on selected markers (Table 2.2). Amplification profiles for PCR were optimized for primer sets. For *Runx2* and *Bsp* the real-time PCR reaction was run at 95 °C for 3 min followed by 45 amplification cycles at 95 °C for 10 s and 60 °C for 34 s. For all other targets the reaction was run at 95 °C for 3 min followed by 45 amplification cycles at 95 °C for 10 s, 56 °C for 20 s and 60 °C for 20 s. The run was completed with the dissociation curve beginning at 65 °C for 5 s and increasing to 95 °C with 0.5°C increments.

**Data acquisition**

qPCR is widely accepted as the *gold standard* for the analysis of gene expression. Analysis of qPCR data is a crucial part of the entire experiment and this has led to the development of a plethora of analysis methods, recently reviewed by Pabingera *et al.* [86]. Following a high-quality qPCR run, the data needs to be correctly analyzed to get biological meaningful results. As depicted in Figure 2.20, fluorescence exponentially increases as the DNA template is amplified. After a few cycles of qPCR, the fluorescence signal surpasses a threshold level above background fluorescence, and begins to increase exponentially. Eventually the fluorescence signal levels off as the detector becomes saturated. At this point, fluorescence is no longer related to the starting template copy number.

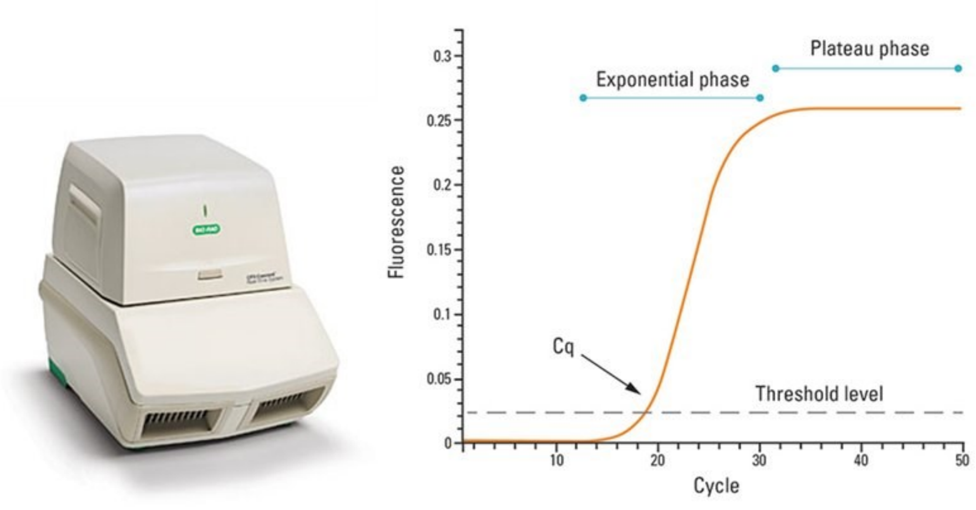

**Figure 2.20. The CFX Connect Bio-Rad real-time PCR system and the data generated during a qPCR run.**
Data show an exponential increase of fluorescence related to the initial DNA amount. Threshold Level: the point at which fluorescence emitted from PCR product formation is significant from background fluorescence. Exponential Phase: the fluorescence increases exponentially as the DNA target sequence is amplified. Plateau Phase: the fluorescence signal levels off.
Images from http://www.thermoscientificbio.com and www.bio-rad.com.

The raw fluorescence values generated in a qPCR run can be used to calculate the **quantification cycle (Cq)** and evaluate the optimization of the assay, as described:
The Cq value, previously known as the threshold cycle (Ct) or crossing point (Cp), is the metric value used for analyzing qPCR results. In general, the Cq value represents the number of cycles needed to reach a set threshold fluorescence signal level and it is determined mainly by the amount of template present in the sample at the start of the amplification cycle. If a large amount of template is present, then relatively few amplification cycles will be required to give a fluorescence signal above background and therefore the reaction will have a low or early Cq. Contrary, if a small amount of template

is present at the start of the reaction, several amplification cycles will be necessary to give a fluorescence signal above background and the reaction will have a high or late Cq value. In order to analyze qPCR data, a baseline is initially subtracted from the raw data, based on the raw fluorescence values. Then, a fluorescence threshold value is chosen so that it captures data during the exponential phase, when reaction efficiency is still stable and hence the results are most reliable. The threshold value is kept constant for all samples analyzed in a run. Using the determined logarithmic Cq value, quantification of nucleic acids can be performed either indirectly by **absolute quantification** (interpolation to standard curves or digital PCR to create linear values) or directly by **relative quantification** (comparative Cq method). Finally, the quantification results can be tested for statistical significant differences and presented in a graphical way [86].

For accurate quantification it is absolutely essential to have an **optimized qPCR** reaction. In order to determine whether a qPCR assay is optimized, serial dilutions of the template (either test cDNA or plasmid DNA with known concentration) are assayed and a standard curve is constructed by plotting the log of concentrations or dilutions of the template against the Cq values obtained during amplification of each dilution.

Ideally, the amplification curves of the diluted template will be evenly spaced. If perfect doubling occurs with each cycle, the spacing is determined by the equation $2^n$ = dilution factor, where n is the difference between the Cq values (number of cycles at the threshold level) of the curves. Therefore for a 10-fold serial dilution, $2^n = 10$, and $n=3.3$ which means that the curves will be separated by 3.3 cycles. Evenly spaced curves will produce a linear standard curve.

The equation of the linear regression line along with the coefficient of determination ($R^2$) can be used to determine whether the qPCR is optimized. An optimized qPCR should have:

- Linear standard curve ($R^2 > 0.980$)
- High amplification efficiency (90-105%)

The **amplification efficiency** is a measure of the overall performance of a real-time PCR assay. It is the rate at which a PCR amplicon (the PCR product generated from a DNA or cDNA template) is generated and is commonly measured as a percentage value. If a particular PCR amplicon doubles in quantity during the geometric phase of its PCR amplification then the PCR assay is said to have 100% efficiency. The amplification efficiency is calculated from the slope of the standard curve using the formula

$$E = 10^{-1/\text{slope}}$$

A 2-fold increase (doubling) in the amount of PCR product translates to a reaction efficiency E of 2. Using the above equation,

$2 = 10^{-1/\text{slope}}$ indicates that the optimal slope of the standard curve will be -3.3, the same as the ideal spacing of the fluorescent curves described above.

To convert E into a percentage as is normally expressed:

$$\% \text{ Efficiency} = (E-1) \times 100\%$$

Therefore, for an ideal reaction where E = 2,

$$\% \text{ Efficiency} = (2-1) \times 100\% = 100\%$$

This translates to a 2-fold increase in the amplicon copy number, or 100% of the template was amplified.

In our experiments, we used 10-fold serial dilutions of the plasmid constructs for each gene as DNA template to generate standard curves and assess the optimization of each qPCR assay. Representative amplification curves, their corresponding standard curves and amplification efficiencies are shown in Figure 2.21 below.

(A)

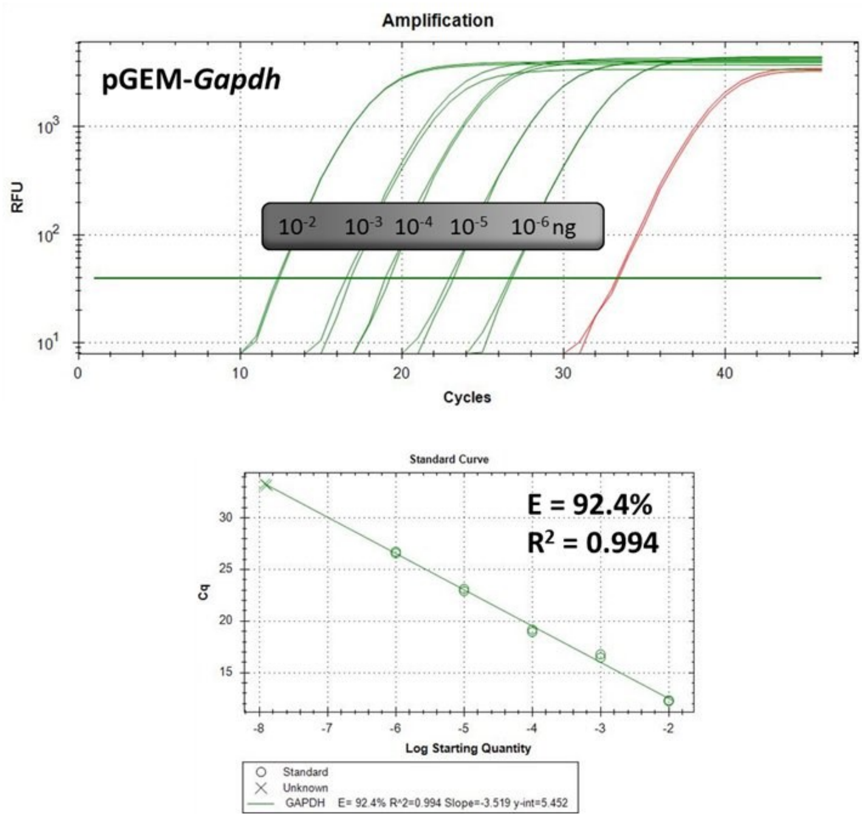
Amplification
pGEM-*Gapdh*
RFU
$10^3$
$10^2$
$10^1$
$10^{-2}$ $10^{-3}$ $10^{-4}$ $10^{-5}$ $10^{-6}$ ng
0
10
20
30
40
Cycles
Standard Curve
E = 92.4%
$R^2$ = 0.994
Cq
30
25
20
15
-8
-7
-6
-5
-4
-3
-2
Log Starting Quantity
Standard
Unknown
GAPDH E= 92.4% R^2=0.994 Slope=-3.519 y-int=5.452

(B)

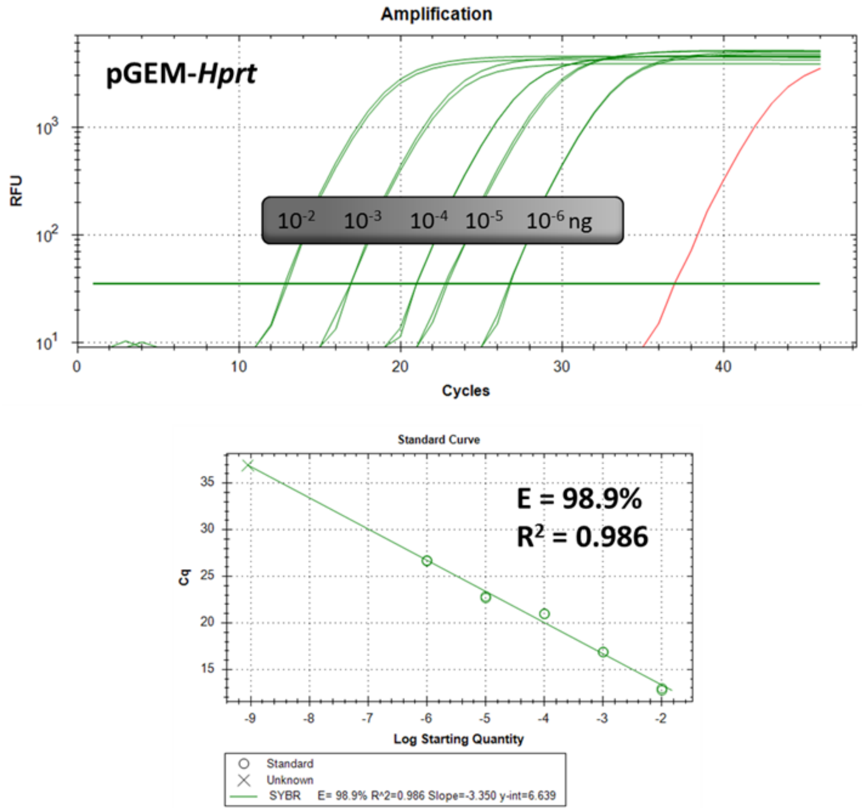
Amplification
pGEM-*Hprt*
RFU
$10^3$
$10^2$
$10^1$
$10^{-2}$ $10^{-3}$ $10^{-4}$ $10^{-5}$ $10^{-6}$ ng
0
10
20
30
40
Cycles
Standard Curve
E = 98.9%
$R^2$ = 0.986
Cq
35
30
25
20
15
-9
-8
-7
-6
-5
-4
-3
-2
Log Starting Quantity
Standard
Unknown
SYBR E= 98.9% R^2=0.986 Slope=-3.350 y-int=6.639

(C)

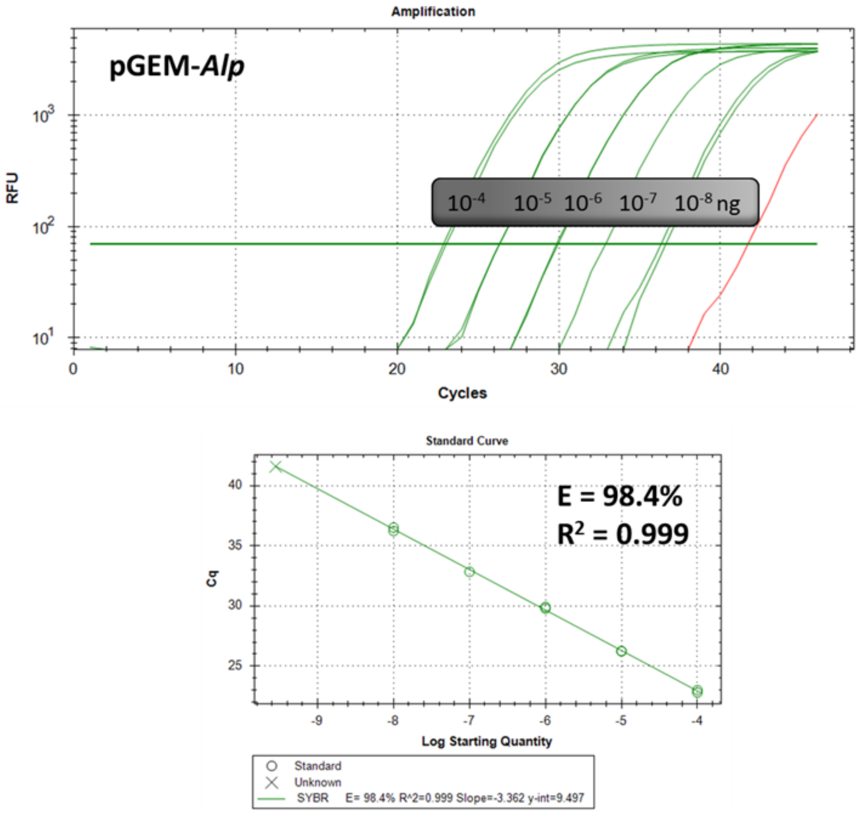

**Figure 2.21. Generating standard curves to assess qPCR reaction optimization.** (A) pGEM-*Gapdh*, (B) pGEM-*Hprt*, (C) pGEM-*Alp*. Standard curves were generated for all target genes using a 10-fold dilution of plasmid DNA templates constructed as described previously. Each dilution was assayed in duplicate (green curves) and water was used as a negative control (red curves). Amplification curves of the dilution series as well as standard curves with the Cq plotted against the log of the starting quantity of template for each dilution. The amplification efficiencies as well as the $R^2$ values of the regression lines are shown.

### qPCR of test samples

Test template samples (cDNA prepared from reverse transcription of total RNA isolated from cultures treated under different conditions, as described in Chapters 5 and 6) were analyzed alongside plasmid DNA standards.

It is important to make sure that the range of plasmid DNA template concentrations used for the standard curve, encompasses the entire range of template concentrations of the test samples to demonstrate that results from the test samples are within the linear range of the standard curve. With this in consideration, we found that a cDNA template dilution of **1:15** (in water) for the test samples would result in sufficient amount of template for detection within the linear range of the standard curves. An example is shown in Figure

2.22, where the amplification curves of test samples falls within the standard curve constructed for the *Hprt* gene.

No reverse transcriptase controls (no-RT) i.e. test RNA samples where the reverse transcription step was omitted, were used to monitor genomic DNA contamination in the cDNA target samples. As shown below, no-RT samples are expected to have high Cq values, comparable to the negative (or no template) control. The negative control monitors contamination and primer-dimer formation that could produce false positive results.

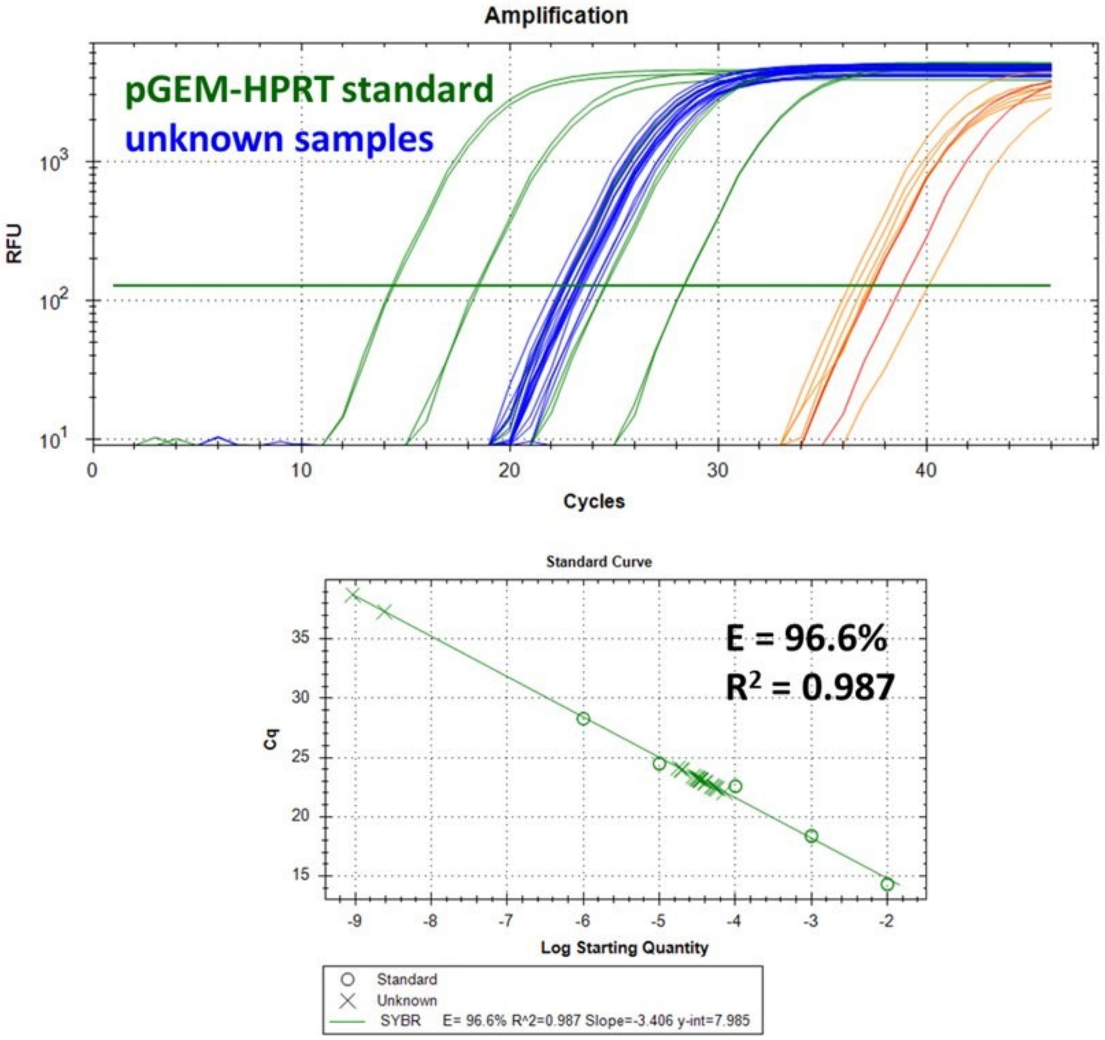

**Figure 2.22. Amplification curves of test samples.**
The amplification curves of several test template samples at 1:15 dilution were generated alongside serial dilutions of plasmid pGEM-*Hprt* and appear to be within the dynamic range of the assay. No-RT and negative controls were used to monitor contamination.

### Selection of housekeeping genes for qPCR

An important aspect of qPCR is selecting appropriate controls or normalization factors to account for any differences in starting cDNA quantities between samples during expression studies. Quantitative gene expression data are often normalized to the expression levels of control or so-called "housekeeping" genes. Housekeeping genes are genes involved in basic functions needed for the sustenance of the cell and an inherent assumption in their use is that expression of these genes remains constant in the cells or tissues under investigation. Although exceptions to this assumption are well documented, housekeeping genes are of value in fully characterized systems [87].

Glyceraldehyde-3-phosphate dehydrogenase (*Gapdh*) is one of the most commonly used housekeeping genes used in comparisons of gene expression data and has been widely used in the investigation of gene expression in the MC3T3 cell line [88]. The hypoxanthine phosphoribosyl transferase (*Hprt*) gene has also been used for gene expression normalization in differentiation studies using the MC3T3 cells [89]. Therefore, for the accurate normalization of quantitative gene expression data in differentiating osteoblasts, we implemented the use of BestKeeper [90] an algorithm that determines the suitability of genes to function as housekeepers by assessing expression stabilities (http://www.gene-quantification.de/bestkeeper.html). We evaluated the expression stabilities of *Gapdh* and *Hprt* genes in MC3T3 cells and found that both genes were suitable to be used as genes for normalization.

### Data analysis: relative quantification with the standard curve method

The standard curve design is a reliable and simple alternative to the PCR-efficiency based calculations in relative real time PCR [91]. It is possible to use the standard curve method to obtain relative rather than absolute quantification if preferred (http://strategy.gene-quantification.info/).

Using the standard curve method, for all test samples, target quantity is determined from the standard curve and divided by the target quantity of the calibrator (untreated control). All sample quantities are therefore expressed as an n-fold difference relative to the calibrator. By using the same stock DNA to prepare standard curves for multiple plates, the relative quantities determined can be compared across the plates.

For normalization to an endogenous reference (housekeeping gene), standard curves are prepared for both the target and the housekeeping gene. For each test sample, the amount

of target and reference is determined from the appropriate standard curve. Then, the target amount is divided by the reference amount to obtain a normalized target value.
Then, each of the normalized target values is divided by the calibrator (untreated control) normalized target value to generate the relative expression levels.
Using plasmid DNA standard curves for relative quantification of RNA has the advantage of achieving high amplification efficiencies in the qPCR reaction.
One drawback is that it assumes that the reverse transcription efficiency of the target is the same in all samples, but the exact value of this efficiency need not be known. Also, it is important that stock plasmid DNA be accurately diluted, but the units used to express this dilution are irrelevant.

In our study, it was important to determine changes in the mRNA level of different osteogenic genes afflicted by the ceramic materials or the nanoparticles, in relation to a control (cells cultured in TCPS). Therefore, **relative quantification of RNA** was chosen.
In this study, qPCR data were analyzed with the **Bio-Rad CFX manager software version 3.0**. Expression of target genes was calculated using the ΔΔCq (where Cq is the threshold cycle) method, after normalization to hypoxanthine phosphoribosyltransferase (*Hprt*) as a housekeeping gene.
We observed that indirect calculation of relevant normalized quantities using the standard curves, as described above, yielded the same results possibly since the software takes into account the efficiency calculated from the standard curves. Results are discussed in Chapters 5 and 6.

# 2.5 Microscopy methods

## 2.5.1 Scanning Electron Microscopy

Adhesion and morphology of MC3T3-E1 cells on the biomaterials were assessed by scanning electron microscopy (SEM). A **scanning electron microscope** (**SEM**) is microscope that uses electrons instead of light to produce images of a sample by scanning it with a focused beam of electrons. The electrons interact with atoms in the sample, producing various signals that can be detected and used to obtain information about the sample's surface topography and composition. Magnification in a SEM can be controlled over a range of up to **6 orders of magnitude from about 10 to 500,000 times** whereas a modern light microscope can achieve a magnification of 1000 times. Resolution can be better than 1 nm with SEM.

The principle behind SEM is schematically shown if Figure 2.23. A heated tungsten filament is used as the electron emission source and the electron beam generated is focused on the sample by a series of electromagnetic lenses. The electrons interact and excite the atoms of the sample's surface, thereby emitting secondary electrons. By scanning the sample in a raster pattern (line by line) and detecting the secondary electrons, an image displaying the topography of the surface is created.

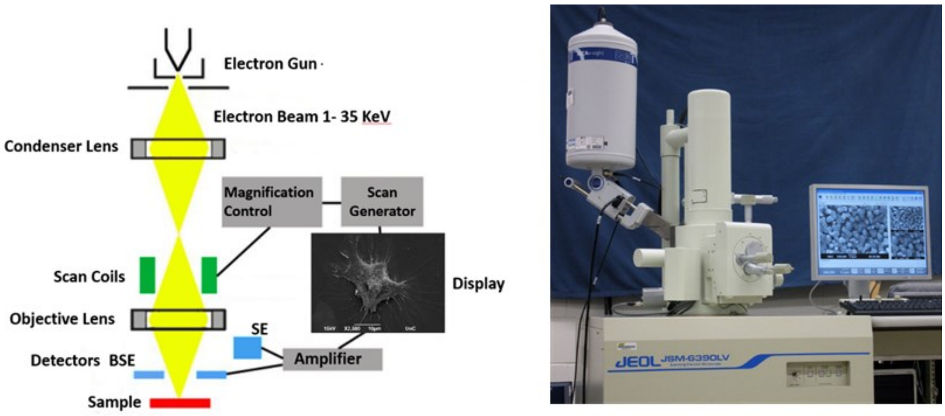

**Figure 2.23. Scanning electron microscope.**
(left) Schematic diagram of a SEM; (right) The JEOL JSM-6390 LV system used in this study. Images adapted from http://zenofstem.com/.

For SEM, a specimen is normally required to be completely dry, since the specimen chamber is at high vacuum. Therefore, unlike hard and dry materials which can be examined with little further treatment, living cells and tissues usually require chemical fixation to preserve and stabilize their structure.

Fixation of all cell samples in this work was performed by incubation in a solution of glutaraldehyde, a buffered chemical fixative, followed by post fixation with osmium tetroxide. The fixed cell specimens were then dehydrated. Because air-drying causes collapse and shrinkage, dehydration was achieved by replacement of water in the cells with ethanol as an organic solvent, followed by replacement of ethanol in turn with liquid carbon dioxide (a transitional fluid) by critical point drying. The carbon dioxide was finally removed while in a supercritical state, so that no gas–liquid interface remains within the sample during drying. The dry specimens were sputter-coated with gold to achieve sample conductivity, and mounted on a specimen stub using an electrically conductive double-sided adhesive tape, before examination in the microscope. All SEM observations were performed using a JEOL JSM-6390 LV shown in Figure 2.23.

### 2.5.2 Optical and Fluorescence Microscopy

Optical microscopy was used routinely in order to monitor cell culture growth, count cells and calculate suitable concentrations for seeding and splitting and to identify possible culture contamination.

The optical or light microscope, uses visible light and a system of lenses to magnify images of small samples. It consists of a light source, the ocular lens, the objectives, a moving stage to focus to the specimen, a diaphragm, a condenser lens and a stage where the sample is placed (Figure 2.24). Charge-coupled device (CCD) cameras allow the capture of digital images whereas digital microscopes use a CCD camera to examine a sample, showing the resulting image directly on a computer screen without the need for eyepieces.

When fluorescence is used instead of visible light, the optical microscope is referred to as a fluorescence microscope. In this case, the specimen is illuminated with light of a specific wavelength which is absorbed by the fluorophores of the labelled sample, causing them to emit light of longer wavelengths. A spectral emission filter is used to separate the illumination light from the much weaker emitted fluorescence. Fluorescence microscopes require a light source (xenon or mercury lamp) or high-power LEDs and lasers), an excitation filter, a dichroic mirror and the emission filter to match the spectral excitation and emission characteristics of the fluorophore used to label the specimen. When the excitation of the fluorophore and detection of the fluorescence are done through the same light path (i.e. through the objective), the microscope is referred to as epifluorescence.

Fluorescence microscopy is very useful when studying non-transparent samples such as in the case of ceramic materials used in this study. The cells on the ceramic materials were stained with a fluorescence dye, carboxyfluorescein succinimidyl ester (CFSE), which allowed for the observation of live cells using an excitation filter at 496 nm and an emission filter at 516 nm.

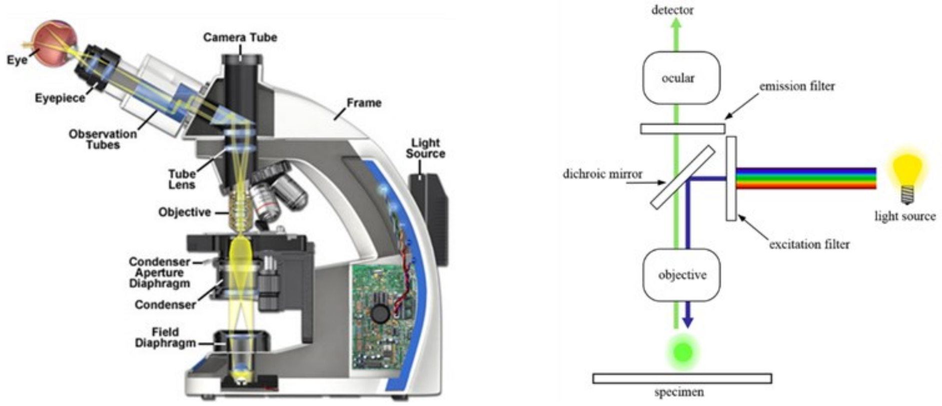

**Figure 2.24. Optical and fluorescence microscopes.**
(left) Schematic diagram showing the components of an optical microscope; (right) Schematic diagram of a fluorescence microscope. Images reproduced from http://zeiss-campus.magnet.fsu.edu/.

CFSE is a cell-permeant dye which crosses the plasma membrane and covalently binds inside cells. Specifically, **the succinimidyl ester group reacts with intracellular lysine residues and other amine sources forming fluorescent conjugates that are well retained inside living cells causing them to fluoresce green** [92]. Due to this covalent coupling reaction fluorescent CFSE can be retained within cells for long periods and also, due to this stable linkage, once incorporated within cells the dye is not transferred to adjacent cells (Figure 2.25).

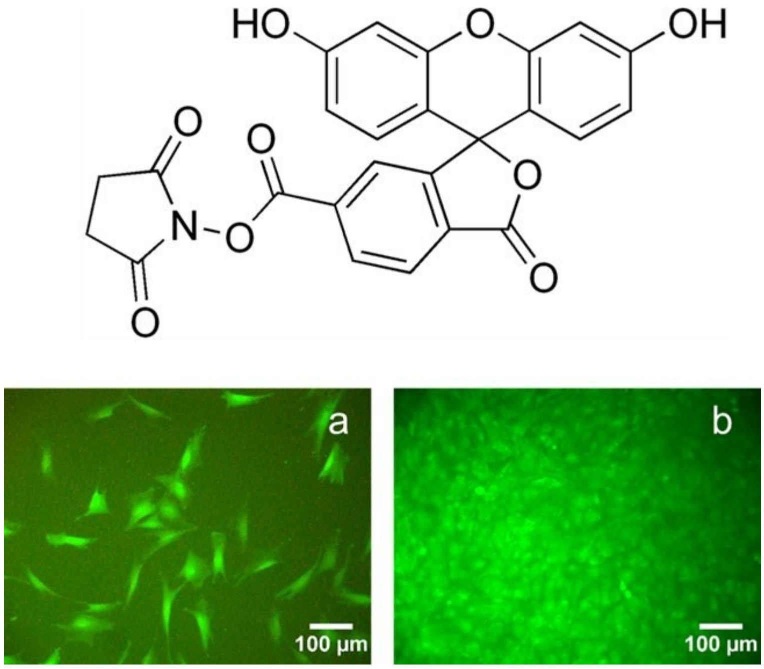

**Figure 2.25. The carboxyfluorescein succinimidyl ester (CFSE).**
The molecular structure of CFSE (top). Living MC3T3 cells were stained with 20 µM CFSE and visualized using fluorescence microscopy; cells on day 1 (left) and day 7 (right) after seeding on TCPS plates, are shown (bottom).

# Chapter 3

# 3 Effect of porosity on the adhesion and proliferation of pre-osteoblasts on alumina and zirconia ceramics

Chapter based on:
A porosity effect on the adhesion and proliferation of pre-osteoblasts on alumina and zirconia ceramics

*Chrystalleni Hadjicharalambous*[1], *Oleg Prymak*[2], *Kateryna Loza*[2], *Sergey Kulkov*[3] *and Maria Chatzinikolaidou*[1,4]

[1]Dept. of Materials Science and Technology, University of Crete, Heraklion, Greece
[2]Inorganic Chemistry, Center for Nanointegration Duisburg-Essen (CeNIDE), University of Duisburg-Essen, Essen, Germany
[3]Tomsk State University and ISPMS RAS, Tomsk, 634021, Russia
[4]IESL-FORTH, Heraklion, Greece

*Manuscript to be submitted*

# 3.1 Introduction

Previous studies on hydroxyapatite ceramics [4, 23] as well as metallic scaffolds of titanium [93] and tantalum [94] have shown that material bioactivity is affected by the degree of scaffold porosity. An explanation for this is that effective circulation of fluid and transportation of nutrients through a porous structure, favors cell migration and proliferation and leads to better bonding with host tissues. The formation of pores in ceramics broadens their possible applications as they can also be used to deliver biomolecules such as bone morphogenetic proteins (BMPs), with sustained release profiles in the human body [4]. Within non-resorbable hydroxyapatite (HA) scaffolds, a porosity threshold of around 60% exists, below which sustainable bone integration cannot be expected [23]. Also, a pore size of 100 μm is often considered as a minimum requirement for healthy ingrowth in porous HA but 300 μm is the optimum size for osteoconduction [4].

Such detailed information is not available for either zirconia or alumina ceramics. However, previous *in vivo* experiments indicated that macroporous (pore size >50 nm) alumina allowed the apposition of physiological bone tissue, unlike dense alumina implants which were surrounded by fibrous tissue [95]. Other studies have shown that porous alumina coatings improved the mechanical properties of titanium implants while the pores could be impregnated with bioactive materials, providing a good surface for osteoblastic growth [96, 97]. Similarly, a series of studies investigated the use of highly porous zirconia (84-87% porosity) as a substrate for hydroxyapatite coating, which resulted in a strong and bioactive scaffold with good bone regeneration demonstrated *in vivo* [98]. It was suggested that the presence of zirconia enhanced the overall osteoconductivity of the scaffold as well as improving its mechanical properties. From these studies, it is proposed that even a bio-inert ceramic can be used as a matrix for tissue growth, if it has a suitable architecture and pore characteristics, and therefore further research in this regard is important.

The objective of this study was to investigate the effect of zirconia and alumina ceramic substrate porosity on cellular adhesion and proliferation. Ceramics of three different porosities produced by sintering and characterized regarding porosity, pore size and phase composition, were employed for the investigation. The impact of porosity was investigated using MC3T3-E1 pre-osteoblasts, by analyzing the metabolic activity of the cells with the PrestoBlue assay as well as evaluating their morphology on the different substrates by scanning electron microscopy.

## 3.2 Materials and methods

### 3.2.1 Ceramic fabrication and characterization

Alumina and zirconia ceramics of three different porosities (A, B, and C from smaller to larger porosity), were used for the experiments. These were prepared using sintering techniques, from starting powders of $Al_2O_3$ or $ZrO_2$ stabilized with 3 mol % $Y_2O_3$. They were characterized in terms of porosity, pore size and mechanical properties by the group of Prof. Kulkov at Tomsk State University. Crystallographic characterization by X-ray powder diffraction (XRD) was carried out by Dr Oleg Prymark at the University of Essen. These procedures are briefly described in Appendix I, whereas more details are given in the relevant manuscript.

### 3.2.2 Cell culture and materials

Minimum essential Eagle's medium (α-MEM), penicillin/streptomycin, fetal bovine serum (FBS) and trypsin/EDTA, were purchased from Sigma (St. Louis, MO). PrestoBlue reagent for cell viability was purchased from Invitrogen Life Technologies (Carlsbad, CA). Cell culture plates were obtained from Corning.

The MC3T3-E1 murine pre-osteoblastic cell line was used for this study [99]. Cells were cultured in alpha-MEM medium supplemented with 10% fetal bovine serum (FBS) and 1% penicillin/streptomycin (primary medium) and maintained at 37 $^0$C in a humidified atmosphere of 5% $CO_2$ in air. Cultures were sub-cultured once a week using trypsin/EDTA. Prior to seeding on samples, confluent cells were harvested using trypsin/EDTA and counted on a haemocytometer. Experiments were carried out using cells between passage 6 and 15 (further details are given in Chapter 2, section 2.3.2, page 38).

### 3.2.3 Cell culture on porous ceramics

The zirconia and alumina samples were ultrasonically cleaned in 100% ethanol for 20 min, sterilized (in a steam autoclave at 123 °C for 2 h) according to standard laboratory procedures, and then placed in a dry oven at 110 °C for 4 h. Following sterilization, ceramic disks were placed into 24-well plates (Costar, Corning Inc.) and seeded with $5 \times 10^4$ cells (in approximately 30 µL suspension in primary medium). Plates were incubated in standard culture conditions (37 °C, 5% $CO_2$ and wet atmosphere) for 30 min to allow for initial cell adhesion and then 500 µL of culture medium was added into each well. The medium was replaced with fresh medium every 2 days.

### 3.2.4 Cell proliferation assay

Cell growth and proliferation of MC3T3-E1 pre-osteoblasts was assessed using the PrestoBlue assay (Invitrogen, CA) after 2, 4 and 8 days of culture. PrestoBlue assay is dependent on the cellular reduction of a blue colored, cell permeant, resazurin-based compound by viable cells to a red product, which can be detected spectrophotometrically and provides a measure of cell viability. Before assessing cell growth on the ceramic materials, we performed tests on MC3T3 cells cultured on tissue culture treated polystyrene (TCPS), to confirm that their growth over time is not affected by the assay reagent or incubation conditions (see Chapter 2, Cell proliferation assay, section 2.4.1, p. 41). Ceramic disks were transferred to an empty plate immediately before assaying, to avoid including cells that have possibly fallen off the ceramic disks and therefore would not allow for an accurate comparison.

At each time point the medium was removed, and PrestoBlue® reagent was added directly to the wells (diluted 1:10 in medium) to cover the ceramic samples. Samples were incubated with PrestoBlue® at 37 $^0$C for 60 min. In order to measure the fluorescence of the colored medium without the interference of the ceramic disks, aliquots of 200 µL were transferred to a black 96-well plate and the fluorescence (544ex/590em) was measured using a spectrophotometer (SpectraMax M2, Molecular Devices Inc, CA). All values were corrected for background fluorescence of reagent with substrate that had not been exposed to cells (blank). The remaining PrestoBlue® reagent was removed from the wells and replaced with fresh culture medium, before further incubation of the plates.

For each ceramic surface, three replicates were used (n=3). Data from three independent experiments were averaged as mean values ± standard error of the mean (SEM) for each time point and sample. Statistical analysis was performed using ANOVA (GraphPad Prism 5 software) to evaluate the differences among ceramic samples. A p value of $<0.05$ was considered significant.

### 3.2.5 Scanning electron microscopy

The morphology of adherent MC3T3-E1 cells was assessed by scanning electron microscopy (SEM). Cells ($5 \times 10^4$ cells/sample) were cultured on alumina and zirconia substrates for 1 or 10 days as described above, rinsed in 0.2 M sodium cacodylate buffer and fixed in 2% gluteraldehyde and 2% paraformaldehyde for 1 h, at 4 °C. Cells were then post fixed in 1% osmium tetroxide for 30 min at 4°C and dehydrated through a series of increasing concentrations of ethanol (from 30 to 100%) and dried by applying critical drying with $CO_2$ at 33°C and 73Atm (Baltec CPD 030). Samples were sputter coated with a 20 nm thick layer of gold (Baltec SCD 050) and observed under a scanning electron microscope (JEOL JSM-6390 LV) with an accelerating voltage of 15 kV.

## 3.3 Results

### 3.3.1 Ceramic sample characterization

The ceramic samples of different porosities were characterized by X-ray powder diffraction and the chemical composition was verified with energy dispersive spectrometry (EDS) analysis. Briefly, all alumina ceramics consisted only of rhombohedral $Al_2O_3$ phase (corundum), whereas the yttria stabilized zirconia ceramics were a two phase system consisting of monoclinic $ZrO_2$ and tetragonal phase in approximately equal amounts. Pore sizes and porosities are shown in Table 3.1. Further details regarding the characterization of ceramic substrates are given in the relevant manuscript.

**Table 3.1. Pore sizes and porosities of zirconia and alumina ceramics.**

| Sample | Chemical composition | Porosity (%) | Small pore mean size (µm) | Large pore mean size (µm) |
|---|---|---|---|---|
| **Zr-A** | $Zr(Y)O_2$ | 19 | 3.1 | N/A |
| **Zr-B** | $Zr(Y)O_2$ | 32 | 6.8 | N/A |
| **Zr-C** | $Zr(Y)O_2$ | 50 | 0.7 | 167±113 |
| **Al-A** | $Al_2O_3$ | 17 | 3.4 | N/A |
| **Al-B** | $Al_2O_3$ | 32 | 2.2 | N/A |
| **Al-C** | $Al_2O_3$ | 61 | 2.1 | 141±113 |

### 3.3.2 Cell metabolic activity

The PrestoBlue assay was used to quantitatively determine the proliferation of viable MC3T3 cells on porous zirconia and alumina substrates. A comparison of the cellular metabolic activity on the different samples after 2, 4 and 8 days of culture is depicted in Figure 3.1. Pre-osteoblasts displayed similar metabolic activities on Al-A, Al-B, Zr-A and Zr-B porous ceramics, regardless of chemistry or porosity, and no significant differences between these substrates were observed. Among zirconia substrates, cell densities were found significantly higher on the highest porosity sample Zr-C for all culture time points. Among alumina, improved metabolic activity was measured on Al-C, but this was not significantly higher than on Al-A or Al-B samples.

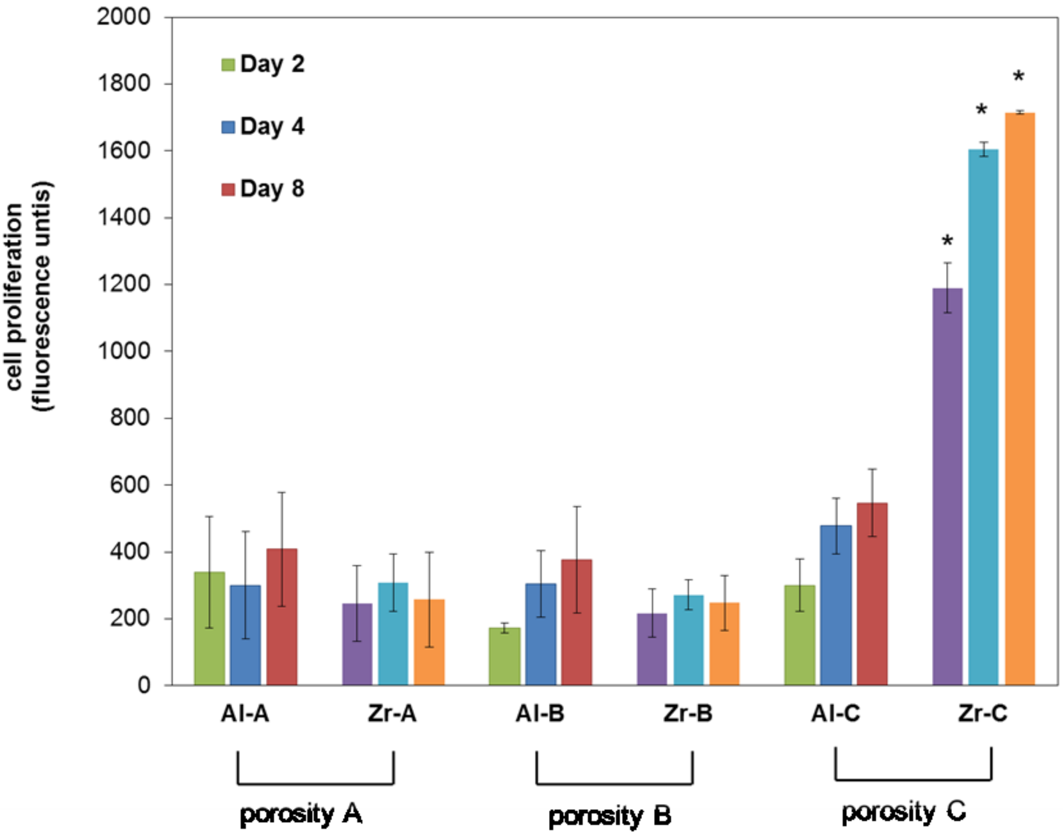

**Figure 3.1. Effect of porosity on cell proliferation inside alumina and zirconia porous ceramics.**
Cell proliferation by PrestoBlue assay, for 17% (Al-A), 32% (Al-B) and 61% (Al-C) porous alumina and 19% (Zr-A), 32% (Zr-B) and 50% (Zr-C) porous zirconia substrates up to 8 days of culture. The metabolic activity of pre-osteoblasts on the highest porosity (50%) zirconia samples was significantly higher (about 3-fold) compare to other samples at all-time points. (*$p < 0.05$, $n = 9$).

## 3.3.3 Cellular attachment and morphology

The morphological appearance of pre-osteoblasts on the different porous alumina and zirconia ceramic substrates was investigated by scanning electron microscopy. Figure 3.2 shows the morphologies of the cells on samples after 1 day of culture. The results showed that cellular appearance and density strongly depended on the substrate. Between zirconia and alumina, cell adhesion morphology was more flattened on zirconia.

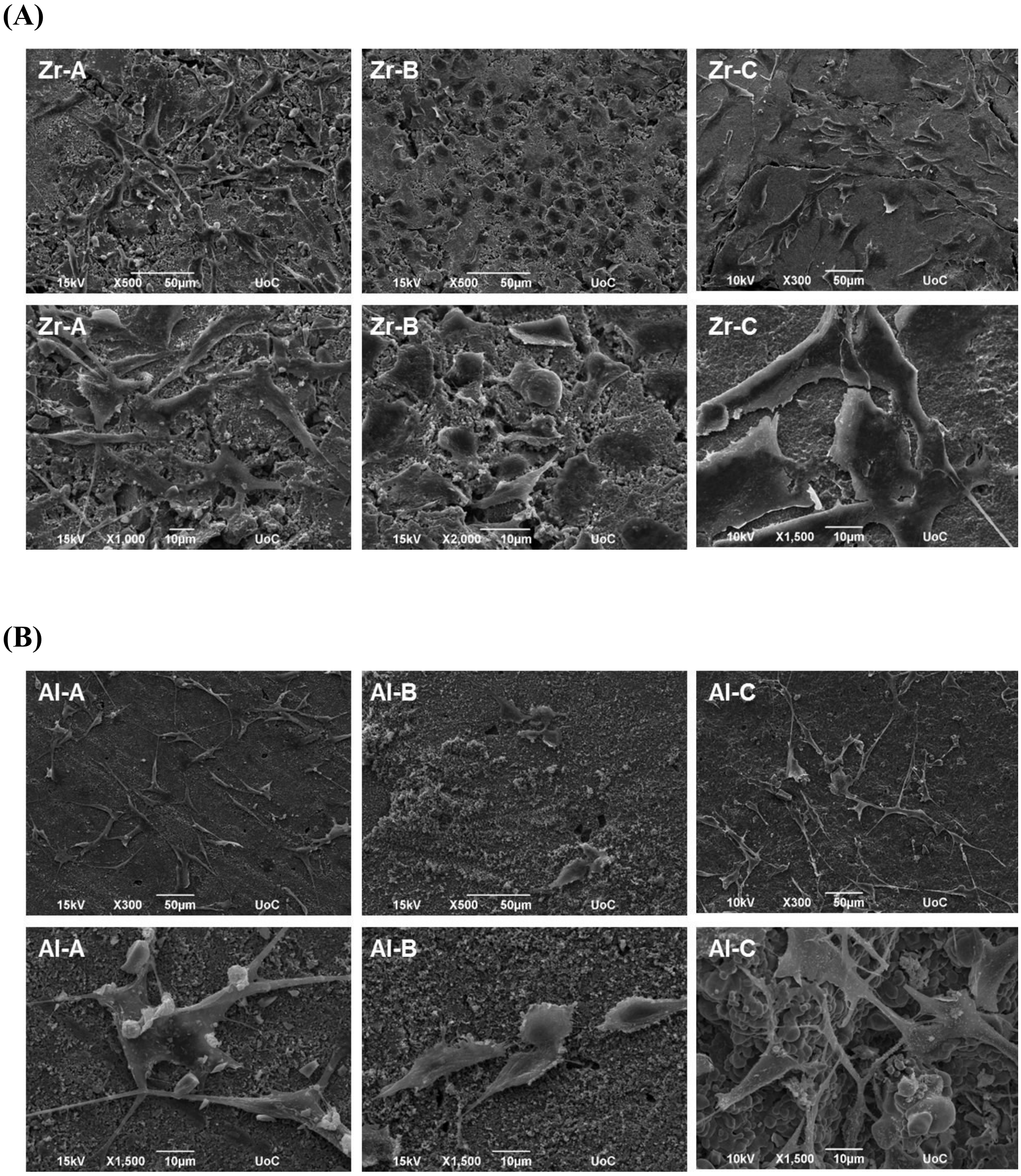

**Figure 3.2. Scanning electron microscopy (SEM) images showing cell morphology of MC3T3 cells after day 1, on alumina and zirconia ceramics of increasing porosity.**

(A) zirconia of 19% (Zr-A), 32% (Zr-B) and 50% (Zr-C) porosities or (B) alumina of 17% (Al-A), 32% (Al-B) and 61% (Al-C) porosities. Increasing porosity resulted in better cell spreading on zirconia but not on alumina ceramics, where cells mostly displayed a long and spindled morphology. Original magnifications are ×500 or ×300 for upper and ×1000 to ×2000 for lower images.

Specifically, cells adherent on Zr-A or Al-A, were found to exhibit branched morphology characterized by long spindle-like cellular extensions, attaching to the sub-micrometer features of the ceramics as well as nearby cells. In contrast, cells cultured on either 32%

porous zirconia (Zr-B) or 32% porous alumina (Al-B) appeared small and round-shaped with under-developed filopodia, whereas cell density appeared to be higher on Zr-B. A further increase in the porosity of zirconia ceramics resulted in a profound effect on cell adhesion, with cells exhibiting flattened morphology and very good membrane spreading on the 50% porous zirconia (Zr-C) substrate (Figure 3.2, A). Interestingly, increasing porosity in alumina ceramics to 61% (Al-C) had no evident impact on cell morphology, as cell spreading on the substrates was limited and spindled morphology was dominant.

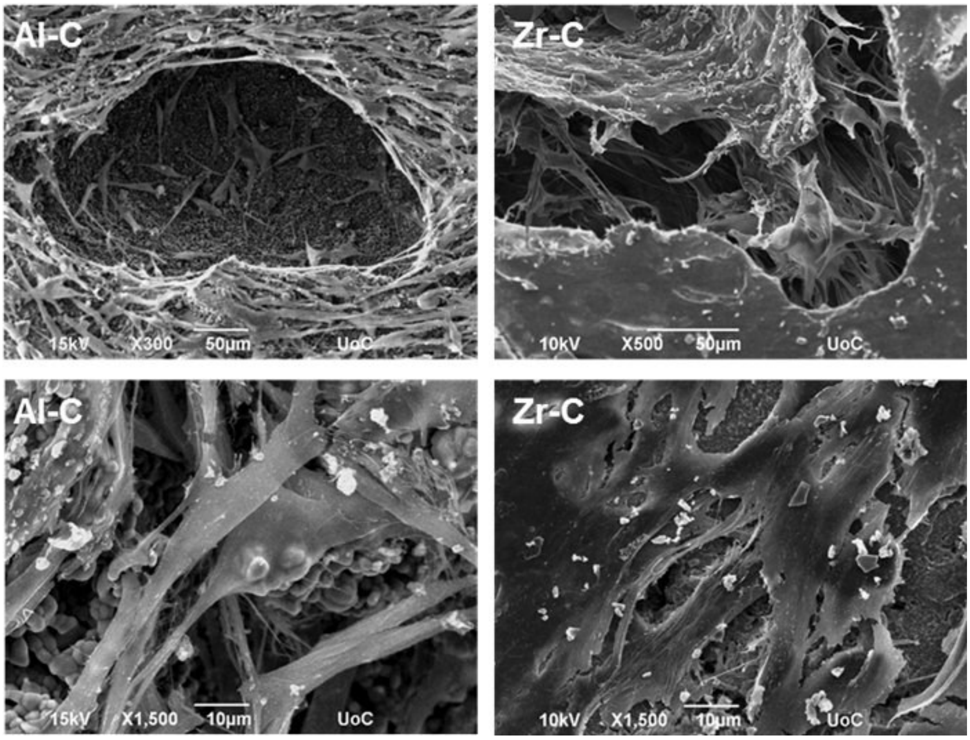

**Figure 3.3. Scanning electron microscopy (SEM) images showing cell morphology of MC3T3 cells after 10 days, on 50% porous zirconia (Zr-C) or 61% porous alumina (Al-C) ceramics.**
A smoother, denser multilayer spreading over pore openings, was observed on zirconia. Original magnifications are ×500, ×300 for upper and ×1500 for lower images.

Cellular growth and the formation of extracellular matrix, as observed by SEM was assessed on the Al-C and Zr-C ceramic samples after 10 days of culture. As shown in Figure 3.3, proliferation of the MC3T3 pre-osteoblastic cells had taken place on both Al-C and Zr-C samples. However, cells on Zr-C, had formed a dense layer that could also bridge large pore openings, unlike cells cultured on Al-C. In addition, the cell matrix on

Zr-C appeared more uniform as individual cells could not always be identified, contrary to cells on Al-C which maintained their initial spindle-shaped morphology and were easily distinguished.

## 3.4 Discussion

In recent years, it has been recognized that biomaterial porosity greatly influences cellular behavior both at the proliferative but also at the differentiation stage [4, 33, 35]. Therefore, it has been suggested that by simply adapting surface properties to the desired cell behavior, we may open up the possibility of controlling cell behaviors, thereby improving implant performance. [100].

The present *in vitro* cell-material interaction study clearly indicates that *porosity is an important parameter regarding cell adhesion and growth on ceramic materials, as assessed qualitatively by SEM and quantitatively using the PrestoBlue® assay*. Enhanced cellular response in terms of adhesion density and proliferation of pre-osteoblasts, was observed when the porosity of zirconia was increased from 19% to 50%, with the simultaneous introduction of pores of approximately 55-280 μm (average size 150 μm), which, are presumed to have a positive impact on cell growth [4].

Cell adhesion and proliferation also depend on material chemistry [23]. In this study, alumina and zirconia ceramics did not exhibit significant differences in cellular growth or adhesion, when porosity was low (samples with A and B porosities). Though material chemistry can be a determinant factor in cell-material interactions, metal oxides such as alumina and zirconia are generally considered bioinert. Their particles (at 2 μm size) have been reported not to be toxic to osteoblasts [101], whereas their ionic forms of $Zr^{+4}$ and $Al^{+3}$ exhibit low to medium toxicity, but such ionic forms are present only at low pH [102].

In a previous report, Lohmann [103] observed higher osteoblast proliferation in the presence of zirconia particles than in the presence of alumina, an effect that the authors found to be related to the higher reactive surface of the alumina particles, which were significantly smaller than the zirconia ones. However, in our study we used sintered ceramics in which alumina particles on the material surface were larger than zirconia particles for all porosities, as shown by SEM. We have found that chemical composition or surface topography differences (due to larger crystallite size in alumina ceramics) alone are not sufficient to induce a differential pre-osteoblast adhesion and growth among these ceramics (porosities A and B) ceramics.

On the other hand, we found that the introduction of larger pores was critical to significantly enhance both cell adhesion and proliferation in zirconia ceramics. This resulted in higher interconnection between the smaller pores inside the Zr-C sample and, as a consequence, better circulation of nutrient medium for the cells. The increased total surface of interconnected pores (small and large) in the Zr-C ceramic provided better conditions for a significantly higher cell adhesion and growth within Zr-C. Similarly, a recent study [104] reported better pre-osteoblast spreading and growth on a porous zirconia scaffold (pores between 200-400 µm) not only in comparison to a non-porous zirconia disk. In fact, the authors showed that cell spreading on porous zirconia was better compared to spreading on a porous zirconia scaffold coated with hydroxyapatite, thus highlighting the importance of substrate architecture in cell behavior.

In this study, we observed better cell adhesion and spreading followed by greater osteoblast proliferation on zirconia (50% porosity) than on alumina (61% porosity) porous scaffolds of similar pore size (porosity C). More flattened cell adhesion on Zr-C than on Al-C on day 1, was followed by the formation of a smoother, more uniform extracellular matrix on Zr-C, as incubation time progressed. The transformation of a cell from spherical to spread-out shape, is important for cell survival [105] and initial cell adhesion is essential to subsequent proliferation [106]. A fully spread, flat cell morphology, was reported to be better with respect to cell proliferation and differentiation [107]. The initially observed flatter cell morphology on Zr-C, may serve as a possible explanation as to why Zr-C elicits higher proliferation versus Al-C. Also, according to the SEM micrographs of the ceramic samples, a greater number of large and deep pores was observed on the surface of Zr-C scaffolds in comparison to Al-C (qualitative observation), which may have contributed to the differences in cell proliferation observed between the highest porosity alumina and zirconia scaffolds.

In the following chapters we further explore the differences in biological response between the highest alumina and zirconia materials by investigating the induction of an osteogenic response in these materials. The effect of chemical composition is analyzed by including a similar porosity alumina/zirconia composite material in the study, as presented in Chapter 4 and a magnesia stabilized zirconia ceramic, as presented in Chapter 5.

# Chapter 4

# 4 *In vitro* biological response on porous ceramics: a comparison between alumina, zirconia and alumina-zirconia composite

Chapter based on:

Porous alumina, zirconia and alumina/zirconia for bone repair: Fabrication, mechanical and *in vitro* biological response

*Chrystalleni Hadjicharalambous*[1], *Ales Buyakov*[3], *Svetlana Buyakova*[3], *Sergey Kulkov*[3] *and Maria Chatzinikolaidou*[1,2]

[1]University of Crete, Dept. of Materials Science and Technology, 71003 Heraklion, Greece
[2]IESL-FORTH, 71110 Heraklion, Greece
[3]Tomsk State University and ISPMS RAS, 2/4 Academicheskii ave. Tomsk, 634021, Russia

*Published, Biomed. Mater. 10 (2015) 025012.*

# 4.1 Introduction

Ceramic materials such as zirconia ($ZrO_2$) and alumina ($Al_2O_3$) are used worldwide for bone repair, due to their biocompatibility and high mechanical strength, which renders them suitable for load-bearing and wear-resistant applications [101]. Nevertheless, alumina brittleness can lead to fracture and zirconia is prone to aging via hydrothermal degradation in the presence of water [30, 108]. To overcome potential zirconia ceramic implant failures, associated with low temperature degradation of the material during long term implantation in the human body, new composite ceramics with improved properties have been developed [29]. Advanced alumina/zirconia composites are currently considered primary candidates for load-bearing parts in artificial hip and knee prostheses, since they benefit from zirconia transformation toughening without the major drawback of aging. They also promise higher strength and fracture resistance for improved reliability and lifetime of orthopedic implants [2, 101, 109].

However, the clinical success of a new ceramic material lies not only on its mechanical properties but also on events that happen largely at the tissue-material interface and determine its integration into the bone [36]. There is a great body of literature associating the enhancement of the initial attachment of osteoblasts or their precursors onto biomaterial surfaces with better bone-implant integration [106, 110]. As this process is largely controlled by material chemistry [23], alumina-zirconia composites offer new ground for investigation of cell-material interactions and may lead to unexpected biological responses.

On the other hand, the bioactivity of ceramics is also highly dependent on the degree of scaffold porosity [4, 23]. In Chapter 3, we have shown that increasing porosity in zirconia, favors cell adhesion morphology as well as growth.

However, increasing porosity compromises the scaffold's mechanical properties and this issue must be considered in order to achieve a balance between the desired mechanical and biological functions, depending on the application. For instance, porosity and pore size are different in cortical bone (pores of 1 to 100 μm and volumetric porosity from 5 to 10%), than in trabecular bone (pores of 200 to 400 μm and volumetric porosity 70 to 90%) [111]. It has been suggested that bimodal-pore ceramics which possess pores of two distinctive size ranges could have superior mechanical properties and have good prospects to be used for biomedical applications [4]. In this context, strong and bimodal-pore zirconia/alumina composites could be advantageous regarding both mechanical properties and biological behavior.

Currently, reports on the interaction of different zirconia/alumina composites with biological systems are limited, but results on dense or foam structures indicate that such materials may be viable substrates for cell growth and differentiation [101, 112-115]. Roualdes *et al*. demonstrated that a zirconia/alumina composite in its dense form did not have deleterious effect on cell morphology, proliferation and ECM formation [101]. In another study conducted by He *et al*., osteoblastic cells were reported to proliferate and differentiate on zirconia toughened alumina ceramic foams which exhibited mechanical properties similar to cancellous bone [114]. *In vitro*, a dense zirconia/alumina composite was found to be comparable to titanium as a viable substrate for growth and differentiation of human osteoblasts [115].

In this chapter, we employed ceramic scaffolds of similar porosity but different chemistry and sought to investigate the extent of cellular response they are able to elicit *in vitro*. Specifically, we focused on the alumina and yttria-stabilized zirconia ceramics which were shown to support cell proliferation in Chapter 3, and compared these against a zirconia-alumina composite (80wt% $Zr(Y)O_2$–20 wt% $Al_2O_3$). For ease of comparison, samples are referred to as A-61 and Z-50 and ZA-60, respectively. We compared the morphology, the long term cellular proliferation (up to 21 days of culture) and osteogenic differentiation of MC3T3 pre-osteoblasts on these materials. Cell viability and proliferation were assessed based on the redox potential of living cells, while cell adhesion and morphology were observed by SEM. Alkaline phosphatase (ALP) activity, collagen production and calcium mineralization were employed for the assessment of the osteogenic response of pre-osteoblastic cells onto the porous ceramic samples.

# 4.2 Materials and methods

## 4.2.1 Fabrication and characterization of porous ceramics

The porous ceramic samples were produced by sintering whereas porosity was determined by the Archimedes method. Pore size distribution was measured by scanning electron microscopy (SEM). Mechanical properties are characterized by compression tests.

Details of the fabrication and characterization procedures are given in Appendix I.

## 4.2.2 Cell culture on porous ceramics for proliferation and differentiation assays

**Materials for these experiments included:** Minimum essential Eagle's medium (α-MEM), ascorbic acid, β-glycerophosphate, penicillin/streptomycin, fetal bovine serum (FBS), trypsin/EDTA, collagen type I, direct red 80, Alizarin Red S, cetylpyridinium chloride (CPC) and p-nitrophenyl phosphate were purchased from Sigma (St. Louis, MO). PrestoBlue® reagent for cell viability and the carboxyfluorescein diacetate succinimidyl ester (CFSE) cell proliferation kit were purchased from Invitrogen Life Technologies (Carlsbad, CA). Cell culture plates were obtained from Corning.

MC3T3-E1 (osteoblast-like) cells were cultured in alpha-MEM medium as described in Chapter 3, section 3.2.2, page 79.

**Cell seeding and culture on ceramics:** The round ceramic disks, 12 mm in size, were ultrasonically cleaned in 100% ethanol for 20 min, sterilized (in a steam autoclave at 123 °C for 2 h) according to standard laboratory procedures, and then placed in a dry oven at 110 °C overnight. Following sterilization, the disks were placed into 12-well plates (Costar, Corning Inc.) and seeded with cells. One hundred thousand cells were seeded on each ceramic sample for proliferation studies and $2 \times 10^5$ cells suspended in 50 μL primary medium were used for the differentiation experiments. Plates were incubated in standard culture conditions (37 °C, 5% $CO_2$ and wet atmosphere) for 30 min to allow for initial cell adhesion and then additional culture medium (900 μL) was added into each well to cover the disks. For the differentiation experiments, primary medium was replaced with osteogenic medium (primary medium supplemented with 10 mM sodium glycerophosphate and 50 µg/mL ascorbic acid) on day 2 after cell seeding. The medium was changed every 2 days. For the controls, cells were seeded directly on tissue culture treated polystyrene (TCPS) plates and treated likewise the ceramic substrates.

### 4.2.3 Cell proliferation assay

Cell metabolic activity and proliferation of MC3T3-E1 pre-osteoblasts were assessed using the PrestoBlue® assay (Invitrogen, CA). At each time point (1, 2, 4, 7, 14 and 21 days of culture), PrestoBlue® reagent was added directly to the wells (1:10), incubated at 37 °C for 60 min and cell growth was assayed as described in Chapter 3, section 3.2.4, page 80. All ceramic and TCPS control samples were analyzed in triplicates.

Cell numbers were calculated by correlating the PrestoBlue® fluorescence values to a standard curve. Growth curves were plotted and the growth rates (from day 1 until day 8) of MC3T3-E1 cells were analyzed using an online calculator (Roth 2006, available from http://www.doubling-time.com/compute.php).

### 4.2.4 Fluorescent living cell staining

Examination of live cells and cell metabolic activity (esterase activity) on the materials was performed with fluorescent staining of living cells with carboxyfluorescein diacetate succinimidyl ester (CFSE). Pre-osteoblasts ($1 \times 10^5$) were cultured on ceramics (two disks for each ceramic composition and time point) for 1 or 7 days, the medium was removed and the cells were washed once with PBS, pH 7.4. Cells were then stained for 15 min with 20 µM CFSE dye in PBS and viewed by fluorescence microscopy (496ex/516em).

### 4.2.5 Cell morphology

Adhesion and morphology of MC3T3-E1 cells onto the ceramic substrates after 1 or 10 days of culture were assessed by scanning electron microscopy (SEM), as described in Chapter 3, section 3.2.5, page 81. For each ceramic composition, two disks were used for the 1 day incubation, and one disk for the 10 days incubation.

## 4.2.6 Alkaline phosphatase (ALP) activity and total protein

Alkaline phosphatase levels, indicating osteoblast differentiation were determined using an enzymatic activity assay. At different time points (7, 14, 21 days) during the differentiation experiments, the medium of each well was collected, and stored at -20 °C for collagen determination (see section 4.2.7, below). Cells were harvested by trypsin-EDTA, collected by centrifugation and rinsed with phosphate buffered saline (PBS, pH 7.4) before being lysed with 100 µL of lysis buffer (0.1% Triton x-100, 50 mM Tris-HCl, 50 mM phenylmethylsulfonyl fluoride (PMSF), pH 10) and 2 × freeze/thaw cycles at -20 °C/room temperature. After thawing, aliquots of lysed cells were used for measurement of protein content and ALP activity.

One hundred µL of freshly prepared assay buffer (2 mg/mL p-nitrophenyl-phosphate (pNPP) substrate in 50 mM Tris-HCl, pH 10 and 2 mM $MgCl_2$) were added to a diluted aliquot (100 µL) of cell lysate in a 96-well plate and incubated at 37 °C for 60 min. The reaction was stopped with the addition of 50 µL 1N NaOH. The color change was measured by spectrophotometry at 405 nm and was correlated to equivalent amounts of *p*-nitrophenol generated, using a calibration curve constructed of known concentrations of *p*-nitrophenol. ALP activity for each well was calculated using the equation [units = nmol *p*-nitrophenol/min]. ALP levels were normalized to cellular protein levels at the end of the experiment and expressed as specific activity.

Protein was determined using the Bradford assay (Applichem, Germany). This method is based on the shift of absorbance maximum of the dye Coomassie Blue G-250, which occurs when the dye binds to proteins. The dye (200 µL) was added to aliquots (20 µL) of cell lysate and the absorbance was measured using a plate reader at 595 nm. Protein concentration was calculated by correlating the reading to a standard curve. All ceramic and TCPS control samples were analyzed in triplicates.

## 4.2.7 Extracellular collagen assay

Total soluble collagen contents in the culture medium were assessed by a modified Sirius Red Dye assay [76]. Briefly, 100 µl diluted cell culture medium supernatants at various time points of culture, were pipetted into 2 mL tubes and stained with 1 mL 0.1% Sirius Red Dye (Sigma) in acetic acid for 30 min (medium which had not been exposed to cells was used as blank). Thereafter, the dye-collagen complex was precipitated by centrifugation (15 min at 15,000 × g) and washed once with 0.1 N HCl to remove all non-bound dye. The stained material was dissolved in 100 µL 0.5 N NaOH and aliquots of 200 µL were transferred to 96-well microtiter plates. The absorbance was measured with a SpectraMax plate reader at 530 nm. Collagen concentrations were calculated by correlating the reading to a standard curve constructed after staining known concentrations of type I collagen with the Sirius Red Dye assay. All samples were analyzed in triplicates.

### 4.2.8 Alizarin Red staining

Calcium-rich deposits representing the final stage of mineralization were stained by Alizarin Red S and quantified by dye extraction. $2 \times 10^5$ MC3T3-E1 cells/disk were cultured in osteogenic media for 14 days as described above. Then, cells were washed with PBS twice and fixed in 4% (v/v) paraformaldehyde (Sigma-Aldrich) for 20 min, washed three times with excess $dH_2O$ and stained with 800 µL of 2% (w/v) ARS (pH 4.1) for 20 min. The wells were washed six times with $dH_2O$ to remove excess stain. To quantify mineralization, 800 µL 10% (w/v) cetylpyridinium chloride (CPC) in 10 mM sodium phosphate (pH 7.0) was added to the wells for 1 h under shaking. Aliquots (200 µL) of the dye extract were transferred to a 96-well plate and read in duplicates at 550 nm. All values were corrected for background absorbance of stained substrates without cells (blank).

The Alizarin Red stain released into solution was expressed as units of Alizarin Red (1 unit is equivalent to 1 unit optical density at 550 nm). Values were normalized to cell numbers, measured with the PrestoBlue® assay, immediately before Alizarin Red S staining. This was achieved by correlating the fluorescence values of the reagent incubated with the substrates to a standard curve constructed of known numbers of cells. Following the PrestoBlue® assay, all substrates were carefully rinsed twice with PBS to remove the reagent, before staining with Alizarin Red could begin. Ceramic samples and controls were analyzed in triplicates.

### 4.2.9 Statistical analysis

Cellular proliferation, collagen, alkaline phosphatase and Alizarin Red staining results are presented as mean values ± standard error to the mean (SEM). Statistical analysis was performed using ANOVA (GraphPad Prism 5 software) followed by Bonferroni posttests to evaluate the differences among ceramic chemical compositions as well as the control tissue culture treated polystyrene surface at each time point. A p value of $<0.05$ was considered significant.

## 4.3 Results

### 4.3.1 Morphology and mechanical properties of the porous ceramics

The microstructure of sintered alumina, zirconia and zirconia/alumina composite ceramics investigated by SEM is depicted in Figure 4.1. Regarding the morphology, irrespective of chemistry, all samples showed large irregular cavities and small mostly spherical micropores. Based on measurements of SEM images (conducted by the group of Prof. Kulkov, Tomsk University), two distinctive pore sizes of 0.7-2.1 µm (small) and 141-183 µm (large) were identified in the ceramics as indicated in Table 4.1, suggesting a bimodal distribution. The open pore volumes of alumina, zirconia and zirconia/alumina composite were found to be between 84-96% of the total volume porosity, indicating good pore interconnectivity. The mechanical data showed lower compressive strength as well as lower elastic modulus for porous A-61 and higher for Z-50 and ZA-60.

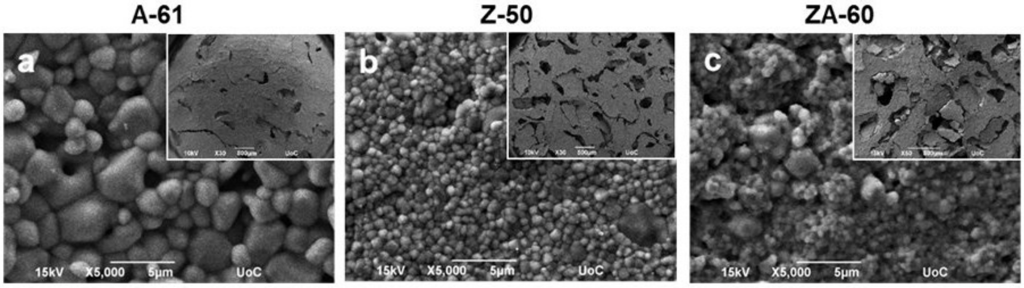

**Figure 4.1. SEM micrographs depicting the microstructure of (a) A-61, (b) Z-50 and (c) ZA-60 with a magnification of × 5000.**
Scale bars represent 5 µm. Insets show an overview of the produced ceramic samples (A-61 and Z-50 at × 30, and ZA-60 at × 50 magnification). Scale bars represent 500 µm.

**Table 4.1. Pore sizes, porosities and mechanical properties of porous ceramics**

| Sample ID | Chemical composition | Total Porosity (%) | Open Porosity (%) | Small pore mean size (µm) | Large pore mean size (µm) | Compressive strength (MPa) | Young's modulus (GPa) |
|---|---|---|---|---|---|---|---|
| A-61 | $Al_2O_3$ | 61 | 55 | 2.1±1.0 | 141±113 | 60 ± 10 | 3 ± 1 |
| Z-50 | $Zr(Y)O_2$ | 50 | 42 | 0.7±0.28 | 167±113 | 210 ± 30 | 10 ± 3 |
| ZA-60 | 80%$Zr(Y)O_2$ - 20%$Al_2O_3$ | 60 | 58 | 0.7±0.39 | 183±145 | 240 ± 30 | 7.5 ± 3 |

The phase composition of the produced samples was investigated by XRD (see Appendix I for more details).

## 4.3.2 Cell proliferation and growth rate on the different substrates

The viability and growth of cells on the ceramic materials was quantitatively determined by the colorimetric PrestoBlue® assay up to 21 days of culture and growth curves were plotted (Figure 4.2). On day 1 following cell seeding, the number of viable cells (indicated by fluorescence units) on TCPS was the highest, followed by Z-50 and ZA-60 with similar values, which were significantly increased when compared to the A-61 substrate. For the whole incubation period, cell numbers were greater on the control tissue culture treated polystyrene TCPS than on the ceramic materials, in agreement with previous reports

[101]. However, as shown in the growth curves, a higher growth rate was calculated on the ceramic materials than on TCPS. Among the porous ceramics, Z-50 supported the highest cell growth, followed closely by ZA-60 composite. As a result, after 21 days of culture, the number of metabolically active cells on these materials was comparable to TCPS.

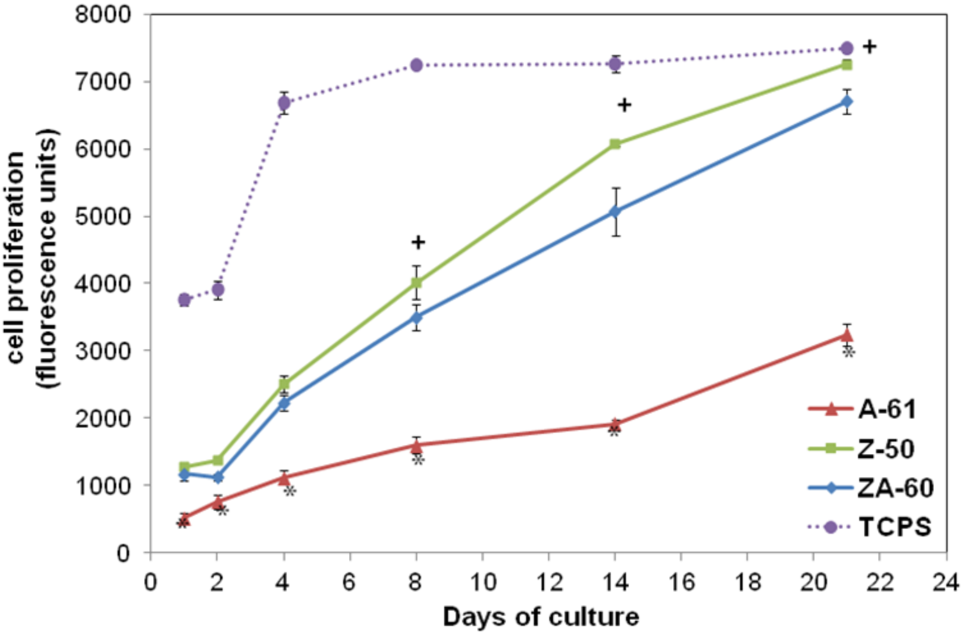

| Substrate | Growth rate (f) |
|---|---|
| A-61 | 0,13 |
| Z-50 | 0,16 |
| ZA-60 | 0,16 |
| TCPS | 0,08 |

**Figure 4.2. Growth curves of MC3T3 cells cultured on porous alumina, zirconia and alumina/zirconia composite materials as well as control TCPS.**
Data are expressed as mean of triplicate samples ± SEM, of two independent experiments (n=6). Among the ceramic substrates, highest growth is observed on Z-50 with $+p < 0.05$ vs. ZA-60; lowest growth is measured on A-61 with $*p < 0.001$ vs. all other materials.

## 4.3.3 Cell metabolic activity: living cell staining

Cells cultured on ceramic substrates and stained with CFSE for live cell observation are shown in Figure 4.3. On day 1, living cells were stained in green color and showed adhesion on all three ceramic materials (Figure 4.3 a,b,c). Cells appeared to have adhered either on the surface or inside large pores and therefore could not be simultaneously depicted in a fluorescence microscopy image. Higher cell density and a normal polygonal morphology were evident on Z-50 and ZA-60 substrates, whereas fewer cells could be visualized on the A-61 substrate. Despite initial differences, after 7 days of culture, cells had significantly proliferated on all three materials (Figure 4.3 d,e,f).

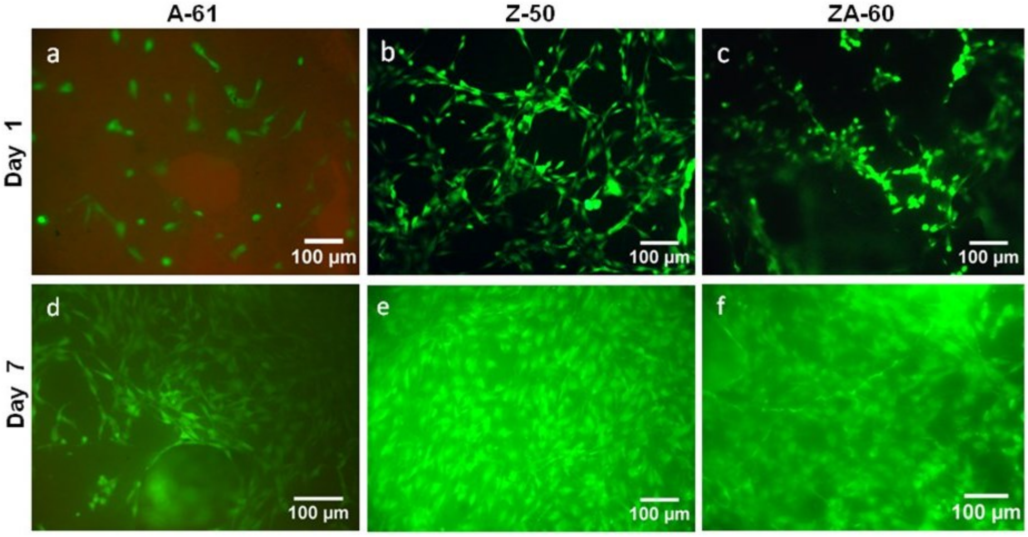

**Figure 4.3. Fluorescent living cell staining of MC3T3 cells cultured on porous alumina, zirconia and alumina/zirconia composite materials.**
Cells were cultured on (a) A-61, (b) Z-50 and (c) ZA-60 for 1 day (top panel) and for 7 days (bottom panel). Significant cell proliferation was observed on day 7 with higher cell densities on Z-50 and ZA-60.

### 4.3.4 SEM analysis of pre osteoblast–ceramic interactions

#### 4.3.4.1 Cell morphology

The morphological appearance of pre-osteoblasts on the different ceramic substrates was investigated by scanning electron microscopy on days 1 and 10 after cell seeding, as shown in Figure 4.4 Figure 4.5. Few cells were observed on the surface on day 1 (Figure 4.4). They were found to have normal osteoblastic morphology and to interact both with the substrate surfaces and with each other, but their appearance depended on the substrate.

On A-61 (Figure 4.4a), cells appeared highly elongated in a spindle-like shape. In contrast, cells on Z-50 (Figure 4.4b) assumed a completely flattened morphology characterized by wide lamellipodia formation, and extensive spreading of the membrane onto the material. Cells on the ZA-60 composite (Figure 4.4c) also appeared flat but exhibited longer cellular extensions than on Z-50. SEM images of MC3T3 cells cultured for 10 days are presented in Figure 4.5, where confluent cell layers can be observed on all materials. Granules on cells appeared, indicating ECM mineralization [94]. On Z-50 (Figure 4.5b,e) and more evidently on ZA-60 (Figure 4.5c,f), cells had formed multilayers on the surface that bridged many large pore areas in a circular growth pattern. The cell matrix was more uniform on Z-50 where individual cells could not be easily identified. On A-61, neither limited cell spreading nor the elongated shape of cells prevented them from reaching confluence but the cell layer was less uniform and did not extent over large pore openings (Figure 4.5a,d).

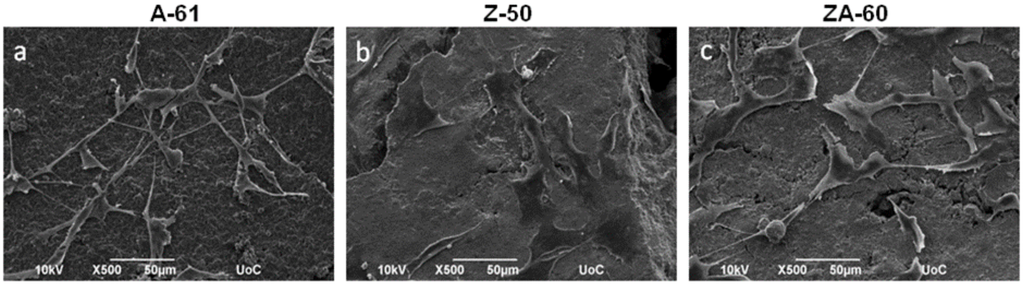

**Figure 4.4. SEM images illustrating MC3T3 cell morphology after 1 day of culture on porous alumina, zirconia and alumina/zirconia composite materials.** (a) A-61, (b) Z-50 and (c) ZA-60. Cells appear elongated and spindle shaped on A-61, unlike Z-50 or ZA-60 on which cells are well spread and flattened. Scale bars represent 50 µm in a 500-fold magnification.

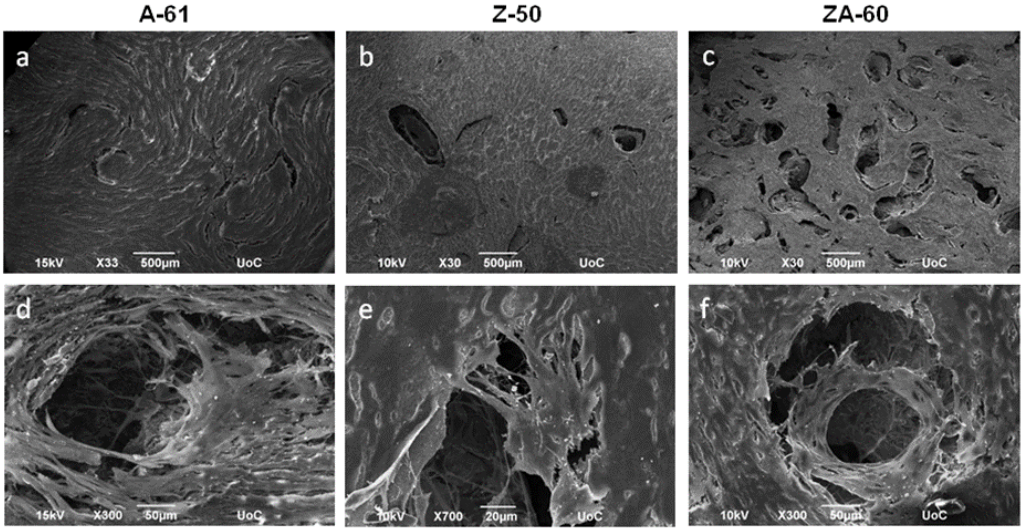

**Figure 4.5. SEM images illustrating cell matrix formation after 10 days of culture on porous alumina, zirconia and alumina/zirconia composite materials.** (a) A-61, (b) Z-50 and (c) ZA-60 at low magnifications (top panel). At higher magnifications (bottom panel) we observe dense cell multi-layers on all three ceramic substrates (d, e, f) and bridging of large pore areas onto Z-50 (e) and ZA-60 (f).

### 4.3.4.2 Cells inside surface pores

On all substrates, cells were observed to have adhered inside pore cavities and proliferated in a very elaborate way. On day 1, individual cells attached to the surface and walls of cavities, aligned to pore openings and even extended invadopodia, as shown in Figure 4.6. Cell-cell as well as cell-surface interactions were evident. It was also observed that cells on ZA-60 were capable of forming complex cell sheets that extended inside large pore cavities or bridged narrower pores (Figure 4.6c,f). Cell growth inside pores was similarly seen on Z-50 (Figure 4.6b,e), but to a much lesser degree on A-61 (Figure 4.6a,d), where fewer cells were observed inside pores.

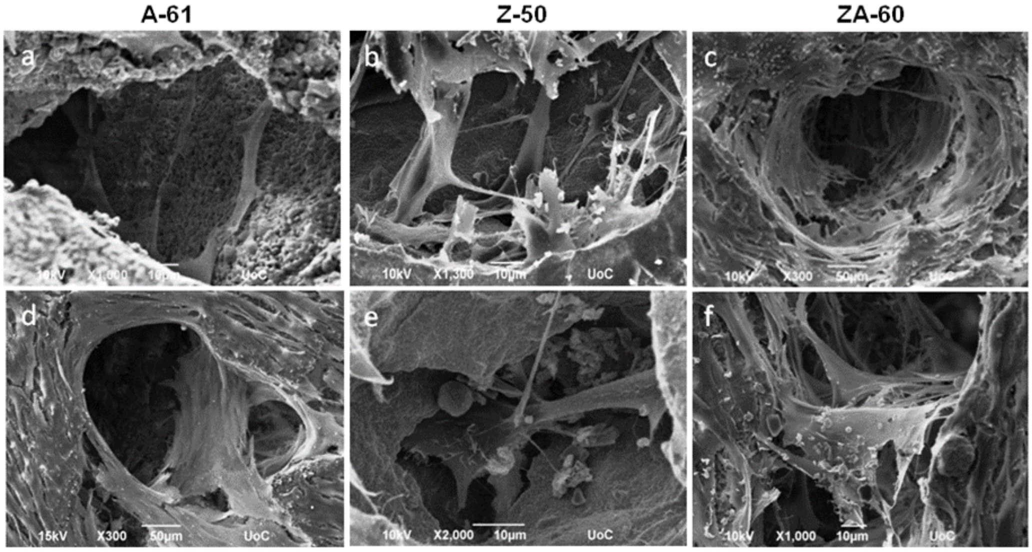

**Figure 4.6. Cells inside pores in all three porous ceramic materials.**
SEM images of MC3T3 cells cultured on A-61 (a,d), Z-50 (b,e) and ZA-60 (c,f) depict cell attachment onto the walls of a pore (a,b), cells growing in a circular mode in the opening of a pore (c,d), cell spreading into a macropore (e), and cells spreading to bridge a narrow pore opening (f).

### 4.3.5 Alkaline phosphatase activity

Alkaline phosphatase (ALP) activity of cells cultured on the different substrates in osteogenic media was measured after 7, 14 and 21 days. As shown in Figure 4.7, ALP activity increased from day 7 to day 14 for all substrates, indicating that the cells had entered the differentiation stage. ALP activity was higher on TCPS control than on ceramics at 7 and 14 days. In cells cultured on A-61, ALP activity increased from day 7 to day 14 and then decreased, following a pattern similar to TCPS. However, on Z-50 or ZA-60, ALP activity increased from day 7 to day 14 and remained at the same levels after 21 days. At this time point the level of ALP activity on Z-50 and ZA-60 was significantly higher than on A-61 or TCPS.

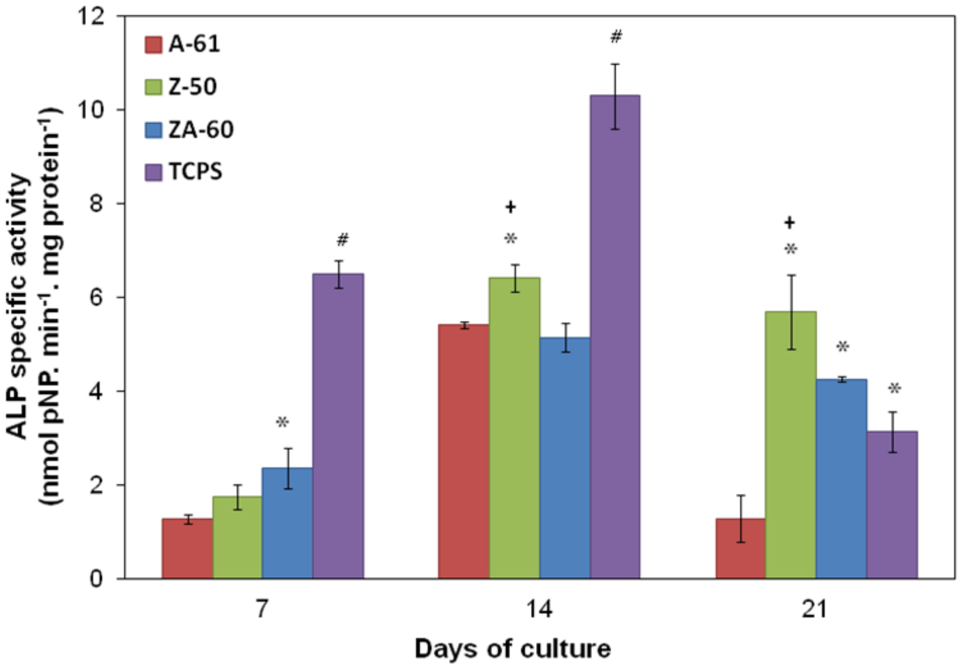

**Figure 4.7. Alkaline phosphatase (ALP) specific activity on the three different ceramic substrates and TCPS after 7, 14 and 21 days in culture.**
Data are expressed as mean of triplicate samples ± SEM, of two independent experiments for day 7 (n=6), and three independent experiments for day 14 and day 21 (n=9). *$p < 0.05$ vs. A-61; +$p < 0.05$ vs. ZA-60; #$p < 0.05$ vs. all ceramic matrices.

## 4.3.6 Collagen production

A feature of osteoblast differentiation is the formation of matrix whose predominant protein is type I collagen. To investigate the effect of porous ceramics on the production of collagen we quantified collagen secreted in culture supernatants at different time intervals, as shown in Figure 4.8, in the presence of exogenous ascorbic acid (AA) which is a co-factor in collagen synthesis [116]. We found that Z-50 and ZA-60 ceramic substrates, enhanced the production of collagen at all-time points relative to control TCPS, and on day 7 this increase was significant. Collagen levels of cells on A-61 were the lowest among the ceramic substrates but still comparable to control TCPS on day 3 and 7, and higher on day 14.

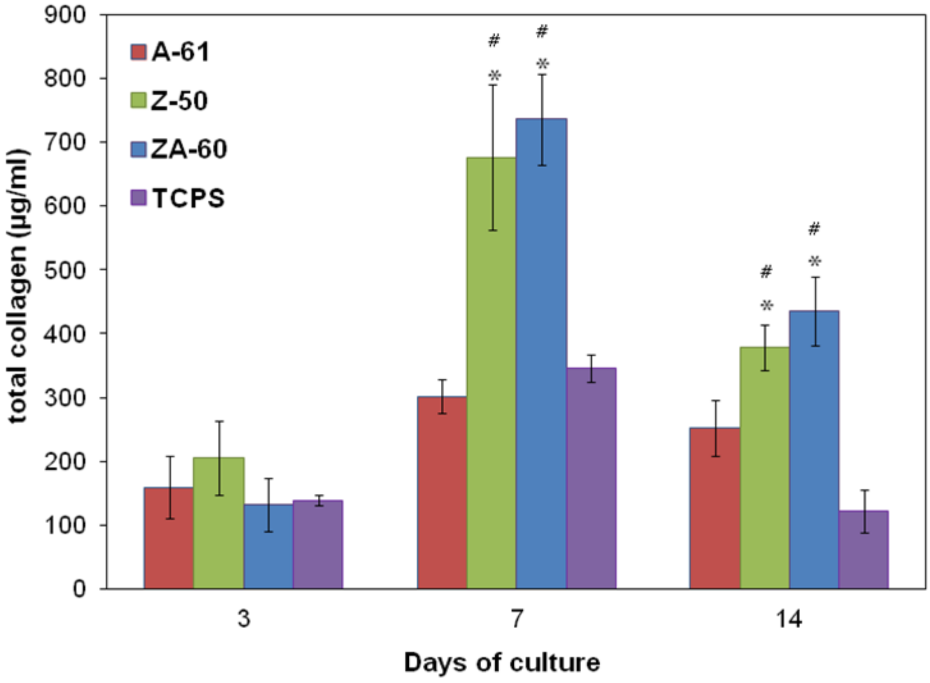

**Figure 4.8. Levels of collagen in the supernatants of MC3T3 cells cultured on three different ceramic substrates and TCPS for 3, 7 and 14 days.**
Levels were determined by the Sirius Red dye binding assay and data are expressed as mean of triplicate samples ± SEM, of two independent experiments for day 3 (n=6), and three independent experiments for day 7 and day 14 (n=9). $^{\#}p < 0.05$ vs. A-61; $^{*}p < 0.05$ vs. TCPS.

## 4.3.7 Matrix mineralization

Calcium deposition through mineralization is a marker of the late differentiation of osteoblasts. We used Alizarin Red to stain calcium deposits in the extracellular matrix after 14 days of culture in osteogenic medium. As shown in Figure 4.9, top, all ceramic disks were positive for Alizarin Red staining. Subsequent extraction of the bound dye revealed almost 2-fold higher mineralization in cells cultured on ceramic substrates than the TCPS control group. The mineralization was highest in cells cultured on ZA-60 composite disks (Figure 4.9, bottom). We sought to normalize calcium deposition to cell number, and for this reason living cell numbers were measured immediately prior to Alizarin Red staining, as described in section 4.2.8, page 95. Average cell numbers of $3.1 \times 10^5$, $3.0 \times 10^5$, $2.1 \times 10^5$ and $2.8 \times 10^5$ were measured on Z-50, ZA-60, A-61 and TCPS respectively. Subsequent normalization of Alizarin units to cell number revealed that the matrix mineralization potential of all ceramic materials was equivalent but higher than TCPS (data not shown).

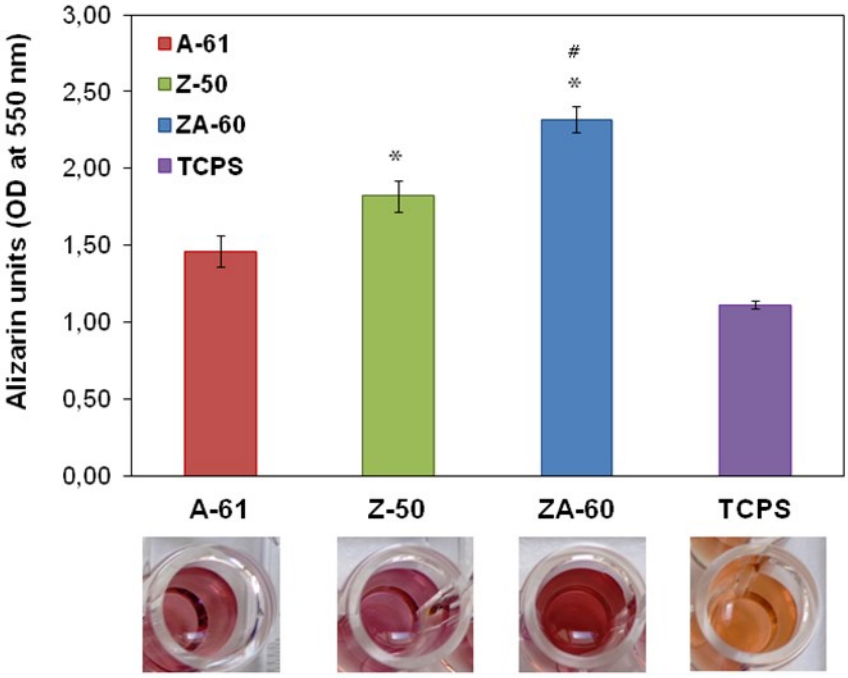

**Figure 4.9. Calcium biomineralization by Alizarin Red S staining of MC3T3 cells cultured for 14 days on ceramic disks and TCPS.**
The graph shows the quantification of the Alizarin Red stain after extraction with cetylpyridinium chloride. Values represent the mean of triplicate samples ± SEM. $^{\#}p < 0.05$ vs. A-61; $^{*}p < 0.05$ vs. TCPS. The images below the graph depict the color of the extracted dye.

# 4.4 Discussion

## 4.4.1 Characteristics of porous ceramics in view of bone applications

Previous studies were mainly focused on HA porous ceramics, and have shown that a porosity threshold of around 60% and a minimum critical pore size of 100 μm are effective to support bone ingrowth [23, 35]. Accordingly, in this study, we investigated the biological response on alumina and zirconia based porous ceramics with total porosities between 50-61% and mean bimodal pore sizes between 0.7-2.1 µm and 141-187 µm. Apart from the total porosity, the open pore volume in porous ceramics is important as it provides a measure of pore interconnectivity. The open pore volumes in the present samples were calculated to be between 84% and 96% of the total porosities indicating that the majority of the pores are interconnected (see Chapter 1, section 1.4.5, page 16 for the calculation method we used). Interconnectivity, which is related to both pore size and the extent of porosity, is necessary to promote body fluid circulation and cell migration to the core of the implant and facilitate the formation of a vascular network, a process that always precedes bone repair [38]. Several reports in the literature stress the importance and benefits of pore interconnections in bone growth and implant fixation [4, 33, 38].

While maintaining a sufficiently open porous structure to promote sustained integration, porous ceramics should also possess mechanical characteristics similar to bone and be appropriate for a variety of clinical situations. Among the three ceramics investigated in this study, highest compressive strengths were achieved in ZA-60 (240 MPa) followed by Z-50 (210 MPa). This was expected as it is known that alumina addition improves the mechanical strength of dense and porous zirconia structures through a mechanism of strengthening and toughening for ceramics [117, 118]. The porous ceramics in our study had high compressive strengths not only due to their medium size pores and porosities, but also due to the intrinsically high strength of the materials and the processing conditions. A good compressive strength of 60 MPa was also achieved for A-61, in agreement with literature on similar porosity alumina ceramics [119]. The compressive strength values measured for all three porous samples closely match the values of human cortical bone (33-193 MPa) [35]. The elastic modulus, a measure of stiffness, varied among the samples between 3 GPa for alumina, 7 GPa for zirconia/alumina and 10 GPa for zirconia, within the mechanical properties reported for cortical bone (3-20 GPa) [94]. Modulus matching is important as it reduces stress-shielding between the implant and the bone in load-bearing applications [120].

### 4.4.2 *In vitro* biological response

The present study clearly indicates that all three porous ceramics are able to support a positive biological interaction with pre-osteoblastic cells. We examined the biological response on these materials using the MC3T3 pre-osteoblastic cell line. The advantage of cell lines for *in vitro* studies is that they are easily obtained and cultured, and in the case of MC3T3-E1 pre-osteoblasts, cells can differentiate into osteoblasts and thus provide information regarding the osteogenicity of the materials [121]. Here, porous zirconia and zirconia/alumina ceramics were found to elicit superior biological responses over porous alumina ceramics with similar porosities. This was assessed qualitatively by SEM cell morphology, fluorescence microscopy and quantitatively using the PrestoBlue® assay. In addition, the ceramic materials displayed good osteogenic response compared to TCPS control. It was not possible to compare the osteogenic response to low porosity zirconia or alumina ceramics (~20%) due to poor cellular growth, which did not allow further investigation (see Chapter 3, section 3.2.4, page 80).

Cellular response onto a material surface begins with adhesion, followed by spreading and eventually, proliferation. Initially, cells undergoing migration move by extending protrusions such as filopodia and lamellipodia, attaching to the surface and retracting their tails [106]. In this study, pre-osteoblasts adhered on all three surfaces but differences in cell morphology after 1 day of culture indicated better spreading and lamellipodia formation on porous Z-50 and ZA-60 rather than A-61, which exhibited mainly spindle, elongated cells. In addition, cell viability measured after 1 day of culture followed the same pattern. These results can be explained mainly on the basis of differences in material chemistry which has been found to govern cell adhesion on biomaterial surfaces [122], but could also be a combination of factors including small variations in scaffold specific surface area [123].

Initial cell adhesion is believed to mediate subsequent events such as proliferation [106], and this was also confirmed by our results. The cell viability data clearly show quantitative differences among the three ceramics regarding pre-osteoblastic cell proliferation up to 21 days of culture. Cells proliferated most rapidly on the porous zirconia Z-50 samples in comparison to the porous zirconia/alumina ZA-60, while the porous alumina A-61 also exhibited growth but had the lowest cell density at all-time points. As zirconia and alumina particles are not cytotoxic, the lowest cell density could be attributed to surface chemical and architectural characteristics that affect initial adhesion. However, once attached, cells proliferated into the pores of the ceramic substrates and therefore more linear growth curves were obtained compared to TCPS. This was also confirmed by SEM and fluorescence microscopy after 7 and 10 days of culture where substantial growth and multilayer formation was observed on the surface as well as inside the cavities of the materials. Interestingly, the differences in appearance and cell morphology of the MC3T3 observed on day 1 SEM examination were retained during proliferation and were also observed on day 10.

Previous reports regarding cell response on porous zirconia or alumina in biomedicine are scarce and have mainly focused on the use of such materials as substrates for coatings or carriers of bioactive agents [4]. Our *in vitro* results show that the porous ceramic samples support cell adhesion and proliferation, but also modulate cell differentiation though to a different extent. This was confirmed initially by an increase in ALP activity, a marker of the early stages of differentiation. Cells on Z-50 and ZA-60 maintained increased levels of ALP up to 21 days unlike A-61, in which ALP levels were reduced following an initial increase. A possible explanation for the maintenance of ALP activity even 21 days after cell seeding, could lie to the fact that cells are still actively proliferating within the pores of Z-50 and ZA-60 scaffolds, as shown by the growth curves (Figure 4.2). Therefore, ALP produced by new pre-osteoblasts could keep ALP levels high for a longer incubation period compare to TCPS, where cell growth had reached a maximum. In addition, extracellular collagen levels increased at the early stages of culture, indicating a healthy ECM matrix formation on the porous ceramics and especially on Z-50 and ZA-60 where levels were the highest. Mineralized matrix formation quantified after 14 days of culture showed almost 2-fold higher calcium deposition within the porous ceramics in comparison to TCPS. Since changes in cell shape that follow cell adhesion on material surfaces affect cell metabolism and differentiation [124], it is possible to link the different levels of osteogenic markers measured among the three porous ceramics to morphological features during initial adhesion.

This study demonstrates the suitability of all three porous ceramic materials for osteoblast proliferation, differentiation and matrix mineralization, with the zirconia-containing materials Z-50 and ZA-60 displaying a better cellular response.

# Chapter 5

# 5 Proliferation and osteogenic response of MC3T3-E1 pre-osteoblastic cells on porous zirconia ceramics stabilized with magnesia or yttria

Chapter based on:

Proliferation and osteogenic response of MC3T3-E1 pre-osteoblastic cells on porous zirconia ceramics stabilized with magnesia or yttria

*Chrystalleni Hadjicharalambous*[1]*, Evdokia Mygdali*[1]*, Oleg Prymak*[2]*, Ales Buyakov*[3]*, Sergey Kulkov*[3] *and Maria Chatzinikolaidou*[1,4]

[1]Dept. of Materials Science and Technology, University of Crete, Heraklion, Greece
[2]Inorganic Chemistry, Center for Nanointegration Duisburg-Essen (CeNIDE), University of Duisburg-Essen, Essen, Germany
[3]Tomsk State University and ISPMS RAS, Tomsk, 634021, Russia
[4]IESL-FORTH, Heraklion, Greece

*Published, J Biomed Mater Res Part A 2015:00A:000–000. DOI: 10.1002/jbm.a.35475*

## 5.1 Introduction

Among zirconia ceramics, the most studied and widely used is yttria-stabilized zirconia (YSZ) with excellent resistance to crack propagation [28, 125]. On the other hand, magnesia-stabilized zirconia (MgSZ) also exhibits high mechanical strength, excellent corrosion resistance and good biocompatibility. Furthermore, it does not experience phase transformation and it has been shown to better resist degradation *in vivo* [126]. Dense yttria- or magnesia-stabilized zirconia ceramics have long been used as bone implants due to their exceptional mechanical performance, but few research groups have investigated the bioactivity of porous zirconia [98], and its potential in biomedicine, as discussed in earlier chapters.

We have shown that cell behavior on zirconia ceramics is influenced by porosity and is superior to alumina of similar porosity. In this chapter, we further look into the effect of material chemistry by investigating differences in *in vitro* cell behavior of two types of porous zirconia ceramics. We have used the 50% porosity, yttria stabilized zirconia substrate and a 57% porosity magnesia stabilized zirconia. For ease of comparison, the materials are termed as YSZ and MgSZ in this chapter. The possible impact of different material chemistry on cell response owning to the presence of either $Y_2O_3$ or MgO as stabilizing agents of zirconia, was investigated through the adhesion, proliferation and differentiation of pre-osteoblastic cells on the materials, which included measurement of gene expression levels of key osteogenic markers. The results were compared to the two-dimensional tissue culture treated polystyrene (TCPS), also seeking to gain greater knowledge on the cell response within porous zirconia scaffolds versus a two dimensional substrate.

## 5.2 Materials and methods

### 5.2.1 Synthesis and characterization of porous ceramics

Two porous zirconia ceramics in which either yttrium oxide ($Y_2O_3$) or magnesium oxide (MgO) was used as dopant at 8% and 3% respectively, were fabricated by sintering, and characterized in terms of porosity, pore size and mechanical properties by the group of Prof. Kulkov at Tomsk State University. Crystallographic characterization by X-ray powder diffraction (XRD) was carried out by Dr Oleg Prymark at the University of Essen. These procedures are described in Appendix I.

### 5.2.2 *In vitro* cell response on YSZ and MgSZ porous ceramics

Experimental procedures followed regarding cell culture maintenance, cell seeding on porous ceramics, assessment of proliferation, and SEM observations are described in Chapter 3, section 3.2, page 79. In addition, the procedures for fluorescent living cell staining and the investigation of osteogenic cell response by means of Alkaline phosphatase (ALP) activity, collagen production and matrix mineralization are described in Chapter 4, sections 4.2, pages 92-96. Statistical analysis was performed using ANOVA (GraphPad Prism 5 software), as described in Chapter 4, section 4.2.9, page 96.

### 5.2.3 RNA extraction and quantitative real-time PCR (qPCR)

Plasmid constructs were employed to serve as external homologous DNA standards of known concentrations and to produce standard curves for each specific gene target and the housekeeping gene. The experimental procedure for the preparation of plasmids, as well as primer sequences of relevant genes are given in Chapter 2, section 2.4.6, pages 52-71.

MC3T3-E1 cells were seeded at $2 \times 10^5$ cells per ceramic disk or control TCPS (24-well plate) and cultured in osteogenic medium for 3 or 7 days. Cells cultured on two ceramic disks or two 24-wells in a TCPS plate were combined into one biological sample, in order to have enough RNA for the experiments. Then, cells were lysed directly on the ceramic disks or TCPS, and total RNA was extracted using the Nucleospin RNA isolation kit (Macherey-Nagel, Germany) according to the manufacturer's protocol.

**Note:** initially, we attempted to extract RNA by first lifting the cells from the ceramic materials using trypsination (with microscopic observation to ensure cells were detached), followed by centrifugation to collect the cells and subsequent processing with Trizol. However, these attempts resulted in low yield and mostly degraded RNA as assessed by agarose gel electrophoresis and UV spectrometry. Higher yield, but yet degraded RNA was collected from cells cultured in TCPS that were also harvested with trypsination prior to Trizol processing, as controls to cells cultured on ceramics. Therefore, this procedure was found inappropriate for isolation of high quality and yield of total RNA required for subsequent qPCR experiments and instead we used an isolation kit which proved to meet the requirements (see Chapter 2, Figure 2.19. Integrity of RNA isolated from cell cultures treated under different conditions., page 63).

Total RNA quantity and purity were determined by UV spectrometry at 260 and 280 nm using a NanoDrop2000 spectrophotometer (Thermo Scientific, USA) as well as 1% agarose gel electrophoresis. Five hundred nanograms of RNA were used for cDNA synthesis by reverse transcription reaction using Superscript II and random primers, according to the manufacturer's protocol (Invitrogen). Real-time quantitative polymerase chain reaction (RT-qPCR) analysis was performed on a CFX Connect Bio-Rad real-time PCR system (Bio-Rad, USA) using KAPA SYBR green Fast Master Mix (KAPA Biosystems, USA) on markers of collagen type I, alpha 1 (*ColI-a1*), alkaline phosphatase (*Alp*), bone sialoprotein (*Bsp*) and runt related transcription factor 2 (*Runx2*), as given in Chapter 2, Table 2.2, page 55. Data were analyzed with the Bio-Rad CFX manager software version 3.0. Relative expression of target genes was calculated using the ΔΔCq (where Cq is the threshold cycle) method after normalization to hypoxanthine phosphoribosyltransferase-1 (*Hprt*) as a housekeeping gene. Triplicate samples from two independent experiments for each time point were analyzed.

## 5.3 Results

### 5.3.1 Structural characteristics of YSZ and MgSZ porous ceramics

The ceramic microstructure was investigated by SEM and is depicted in Figure 5.1. It was mostly granular with small micropores evident on both YSZ and MgSZ ceramics. Doping zirconia by MgO was found to result in a brain-like microstructure that interrupted the otherwise granular microstructure of the ceramic.

The phase composition of the produced samples was investigated by XRD (see Appendix I for details). Briefly, it was found that both ceramics consisted mainly of monoclinic phase $ZrO_2$. It was shown that the MgSZ ceramic consisted of about 62 wt% monoclinic $ZrO_2$ phase and 33 wt% magnesia stabilized cubic MgZrO phase as well as 5 wt% $MgAl_2O_4$ arising from a small amount of Al from powder impurities. The YSZ-sample consisted of approximately equal amounts of $ZrO_2$ and yttria stabilized tetragonal phases (approx. 49:51 wt%). The amount of incorporated Mg-atoms or Y-atoms in the ceramics, corresponded well to the previously used amount of mixing MgO and $Y_2O_3$ powders (3 and 8 wt% respectively).

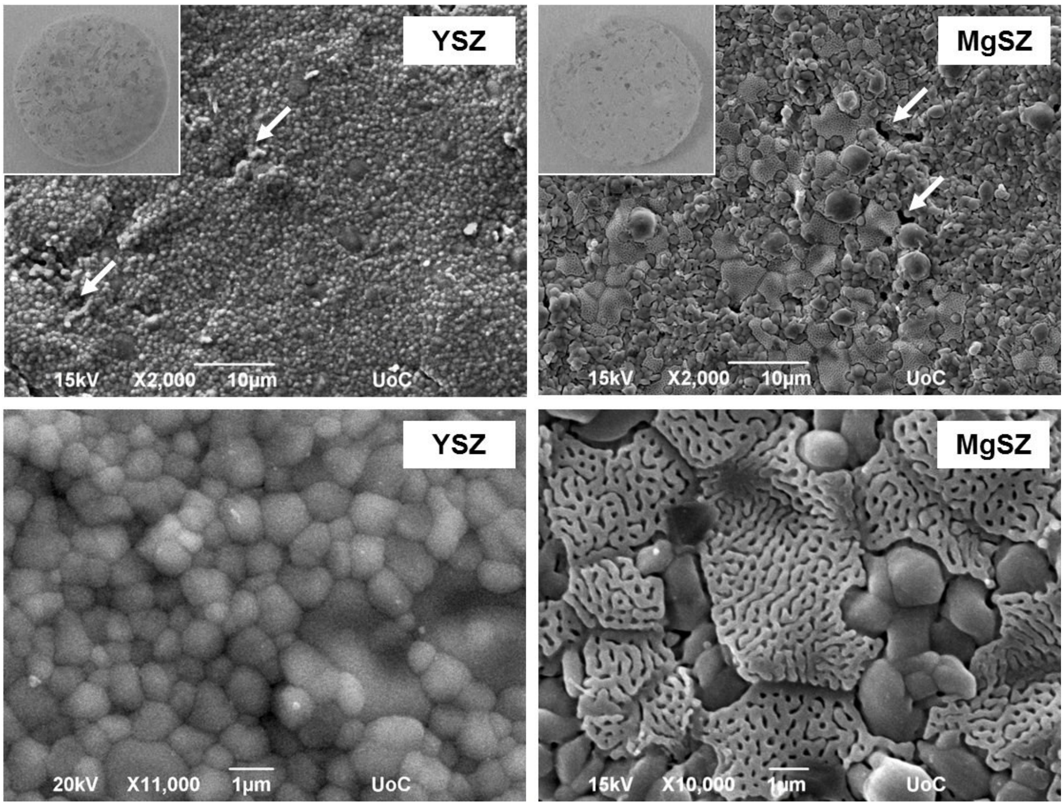

**Figure 5.1. Scanning electron micrographs showing the microstructure of YSZ and MgSZ samples.**
The porosity is interconnected (small pores are shown by arrows) and the structure is characterized by a high degree of surface topography. Original magnifications are ×2,000 (top panel). The microstructures of YSZ and MgSZ are shown at ×11,000 and ×10,000 (bottom panel). The insets depict a general view of the actual ceramics.

Pore size, porosity and mechanical characteristics of porous YSZ and MgSZ ceramics are provided in Table 5.1. Both materials are bimodal-pore ceramics with two distinctive size ranges of 0.7 µm (small) and 167 µm (large) pores for YSZ and 1.1 µm (small) and 144 µm (large) pores for MgSZ. The largest pores are about 280 µm in YSZ and 246 µm in MgSZ. The ceramics also show a high degree of open porosity, at 84% for YSZ and 89% for MgSZ respectively, which results into very good pore interconnectivity. The compressive strength values of the ceramics are similar to the values of human cortical bone (33-193 MPa) [35]. The elastic modulus, a measure of stiffness, was measured at 10 GPa for YSZ and 6 GPa for MgSZ alumina, also within the mechanical properties reported for cortical bone (3-20 GPa) [94].

**Table 5.1. Microstructural characteristics of YSZ and MgSZ porous scaffolds**

| Sample | Chemical composition | Total Porosity (%) | Open Porosity (%) | Small pore mean size (μm) | Large pore mean size (μm) | Compressive strength (MPa) | Young's modulus (GPa) |
|---|---|---|---|---|---|---|---|
| YSZ | $Zr(Y)O_2$ | 50 | 42 | 0.7±0.3 | 167±113 | 210 ± 30 | 10 ± 3 |
| MgSZ | $Zr(Mg)O_2$ | 57 | 51 | 1.1±0.5 | 144±102 | 120 ± 30 | 6 ± 2 |

# 5.4 *In vitro* cell investigation

## 5.4.1 Scanning electron microscopy analysis

Pre-osteoblastic cell adhesion on YSZ and MgSZ porous scaffolds was investigated by scanning electron microscopy on days 1 and 10 after cell seeding, and is depicted in Figure 5.2. Images on day 1 show that a high number of cells adhered on the surface of either YSZ or MgSZ ceramics, and the cells exhibited distinct morphological characteristics. On YSZ, cells were principally flat with wide lamellipodia and good spreading of the cell membrane. Cells on MgSZ also appeared round and flat, but exhibited several finger-like membrane protrusions, resembling filopodia.

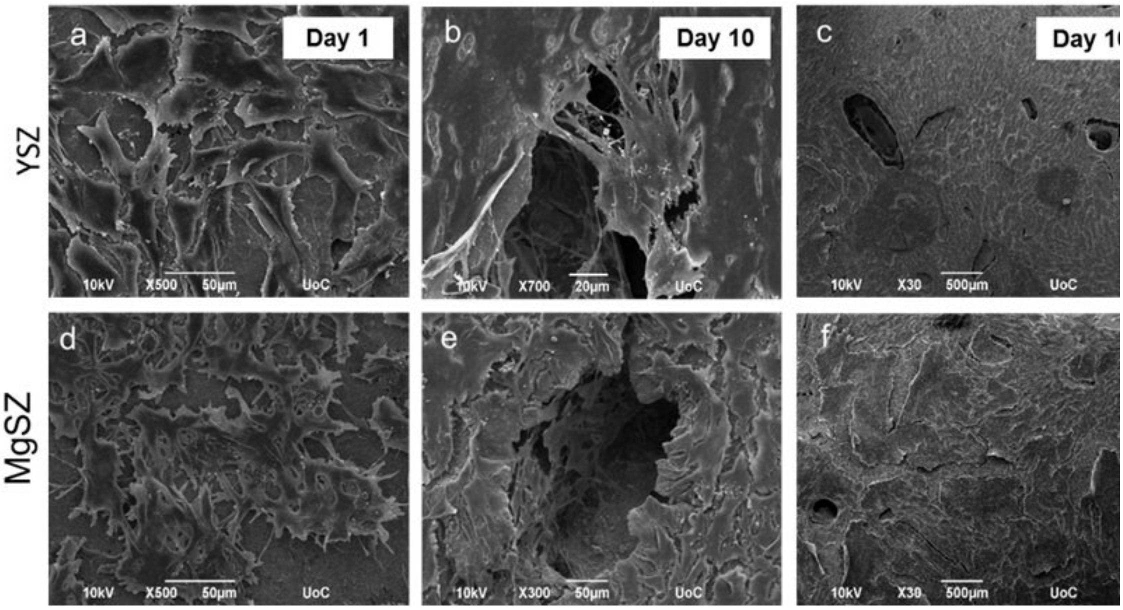

**Figure 5.2. SEM images illustrating MC3T3 cell adhesion and growth on YSZ and MgSZ ceramics.**
SEM images illustrating MC3T3 cell adhesion and growth on YSZ and MgSZ ceramics. After 1 day of seeding, cells appeared much flatter and spread out on (a) YSZ as compared to (d) MgSZ. At 10 days of culture, cells grew well on both (b, c) YSZ and (e, f) MgSZ substrates covering the outer surface as well as the pores. Original magnifications are ×500, except for ×300 (e) and ×700 (b).

After 10 days of culture, the pre-osteoblastic cells showed extensive proliferation and coverage of the experimental surface on both ceramics. As shown by SEM, cells formed a dense layer that could also bridge some pore openings. The cell matrix was more uniform on YSZ than MgSZ (Figure 5.2 c, f), consistent with the initial cell morphology on day 1. Granules on cell matrix appeared, indicating mineralization of the ECM on porous scaffolds [94].

## 5.4.2 Cell proliferation

Proliferation of pre-osteoblasts on the porous ceramics was qualitatively assessed following living cell staining with CFSE, as shown by images in Figure 5.3. On day 1, living cells stained in green color and showed adhesion on both ceramics whereas cell densities appeared comparable. After 7 days of culture, cells had significantly proliferated and formed a confluent living cell layer on both YSZ and MgSZ.

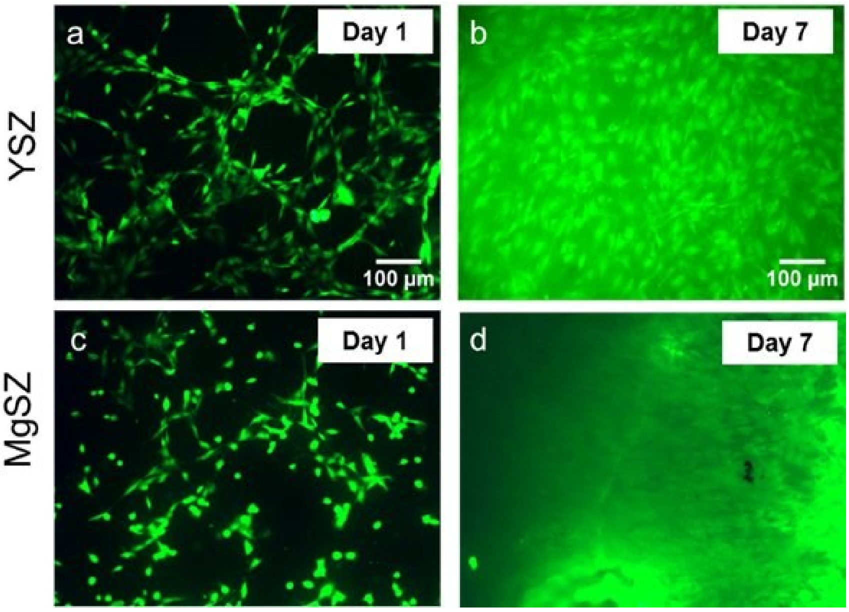

**Figure 5.3. Fluorescent living cell staining of MC3T3 cells on YSZ and MgSZ ceramics.**
Cells were cultured for 1 or 7 days on (a, b) YSZ and (c, d) MgSZ ceramics. Original magnification is ×10. Significant cell proliferation was observed on day 7 with high cell densities occurring on both substrates. Scale bar represents 100 µm.

Moreover, the growth of cells on ceramic scaffolds was quantitatively determined by the colorimetric PrestoBlue® assay up to 21 days of culture and compared to tissue culture treated polystyrene (TCPS) as reference material (Figure 5.4.). Compared to porous scaffolds, the number of viable cells (indicated by fluorescence units) was significantly higher on TCPS at every time point except for day 21, when cell numbers were similar for TCPS and YSZ. Between YSZ and MgSZ, viable cell numbers were higher on YSZ for the entire culture period. Calculating the growth rate (number of doublings that occur per unit of time) of the cells on each substrate we found that the pre-osteoblasts proliferated at a higher growth rate on the porous scaffolds (0.16 for YSZ and 0.14 for MgSZ) than on TCPS (0.08). The growth rate was calculated for a period up to 8 days of culture, during which, cell numbers were increasing on all substrates.

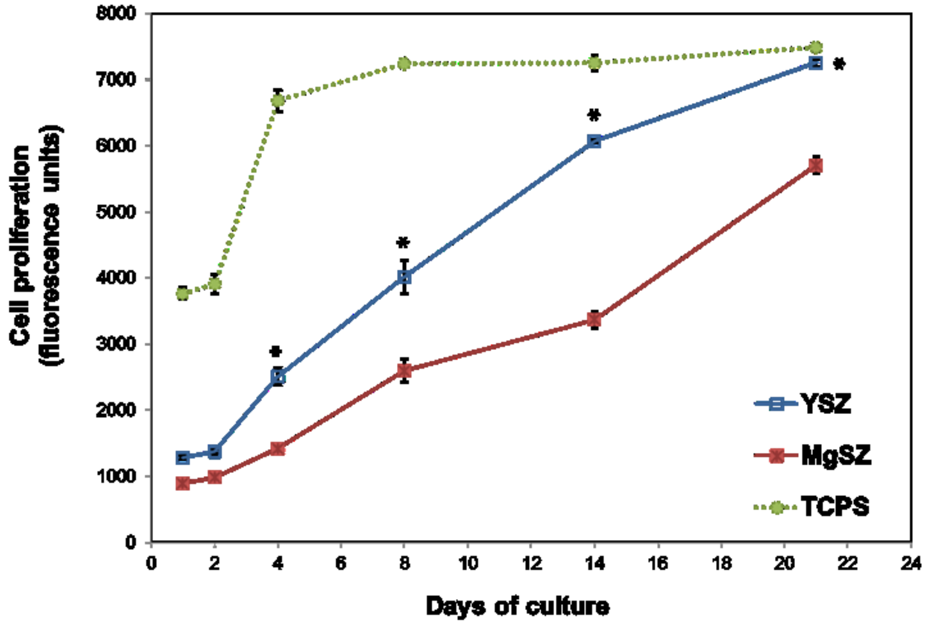

**Figure 5.4. Presto Blue proliferation assay showing growth of MC3T3 cells cultured on either YSZ or MgSZ porous scaffolds, or control TCPS.**
Data are shown as mean ± SEM of triplicates in two independent experiments (n=6). The porous scaffolds, had similar growth rates but higher cell numbers were detected on YSZ with $^{*}p < 0.001$ vs. MgSZ at most time points.

## 5.4.3 Alkaline phosphatase activity

The osteogenic potential of the pre-osteoblastic cells on porous YSZ and MgSZ was characterized using the alkaline phosphatase (ALP) activity as an early phase osteogenic marker. ALP activity of cells cultured on the porous scaffolds was normalized to protein concentration and plotted in Figure 5.5. After 2 weeks, an evident increase in ALP activity on both porous scaffolds was observed. At this point, the ALP activity was significantly higher on the YSZ compared to MgSZ scaffolds. While ALP measurements show an increase in the enzyme specific activity on both porous scaffolds up to 3 weeks, no significant differences were found between the two scaffolds at this time point. Unlike porous ceramics, ALP activity on TCPS controls, peaked on day 14, followed by a sharp decrease on day 21.

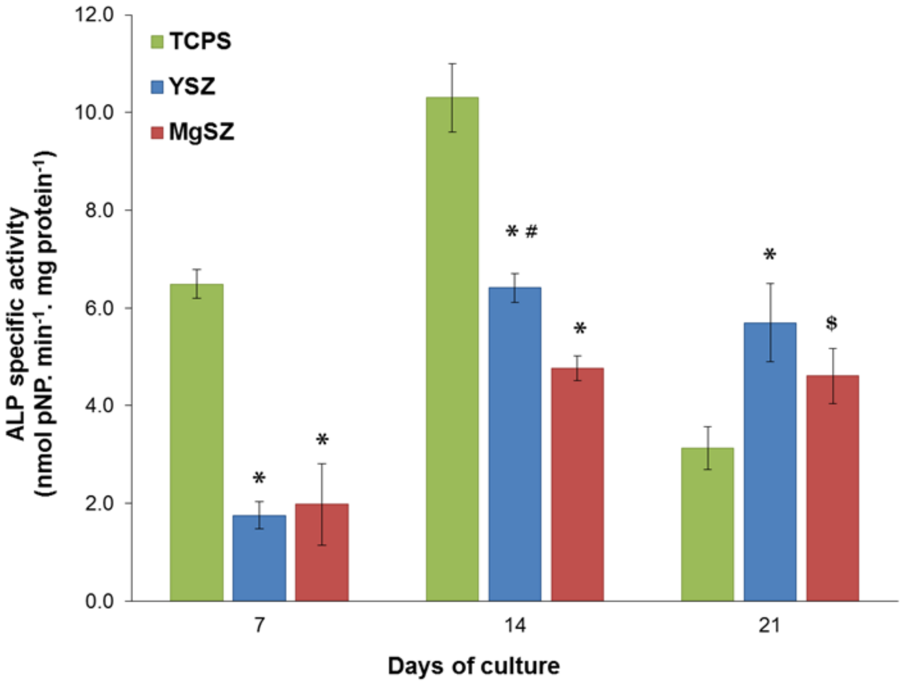

**Figure 5.5. Pre-osteoblast alkaline-phosphatase activity after 7, 14 and 21 days of culture on YSZ, MgSZ and polystyrene control (TCPS).**
The results are presented as ALP specific activity and expressed as nmol.min$^{-1}$.mg$^{-1}$ of total protein (mean ± SEM) of triplicates in two-three independent experiments, n=6-9; $^{\#}p < 0.001$ vs. MgSZ; $^{*}p < 0.001$ vs. TCPS; $^{\$}p < 0.01$ vs. TCPS.

## 5.4.4 Collagen secretion

To investigate if the ceramic scaffolds affect collagen production, we quantified the secreted collagen in the supernatant of cultures at different incubation intervals (Figure 5.6). We found that, between 5-7 days, pre-osteoblasts cultured on YSZ ceramic scaffolds had a collagen production that was 70% higher than that of cells on MgSZ or TCPS control. This production was 150% higher in the interval between 12-14 days. Collagen levels of MgSZ cultured cells were similar to those cultured on TCPS.

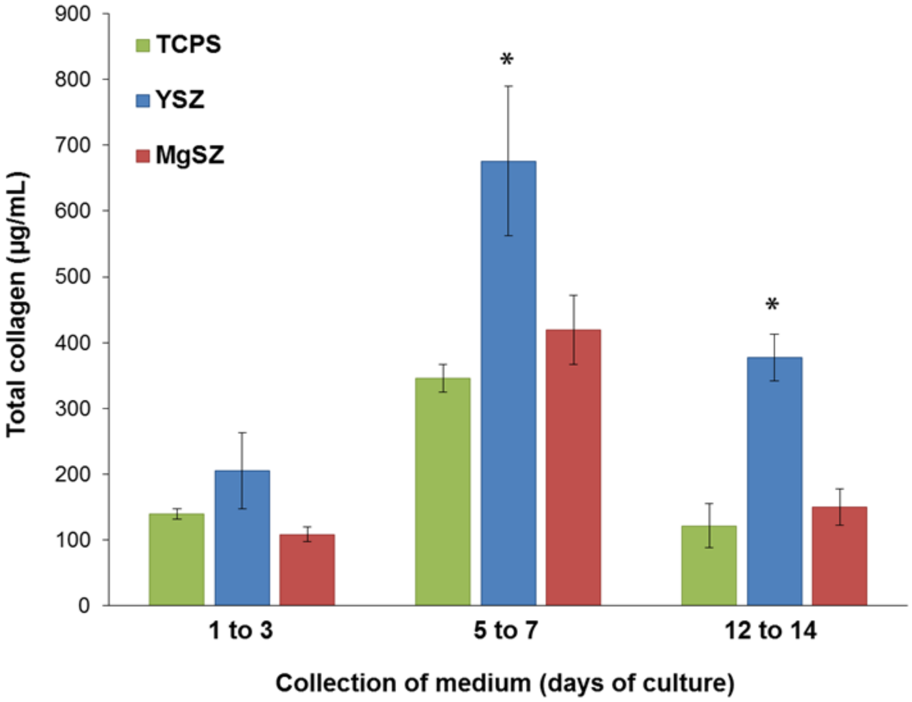

**Figure 5.6. Levels of collagen secreted in the medium of MC3T3 cells cultured on porous ceramics or TCPS control, as determined by the Sirius red dye binding assay.**
Values are expressed as mean ± SEM of triplicates of two independent experiments (n=6); *p < 0.001 vs. TCPS or MgSZ.

### 5.4.5 Bone-related gene expression

We evaluated the mRNA expressions of *Alp*, *Runx2*, *ColIa1* and *Bsp* bone-related genes, after the MC3T3-E1 cells were cultured on ceramics or TCPS for 3 or 7 days. Data analyzed from quantitative real time PCR (Figure 5.7) show that gene expression of *Bsp* is significantly increased in cells cultured on either YSZ (14-fold) or MgSZ (3-fold) compared to the polystyrene control. Between the two ceramics, *Bsp* mRNA expression is markedly higher on YSZ than on MgSZ at 5-fold on day 3 and 2.7-fold on day 7. Moreover, after 3 days, the expression level of *ColIa1* was significantly higher on YSZ than on MgSZ, or control. After 7 days, no statistical difference was found in *ColIa1* mRNA levels between the ceramic scaffolds or control.

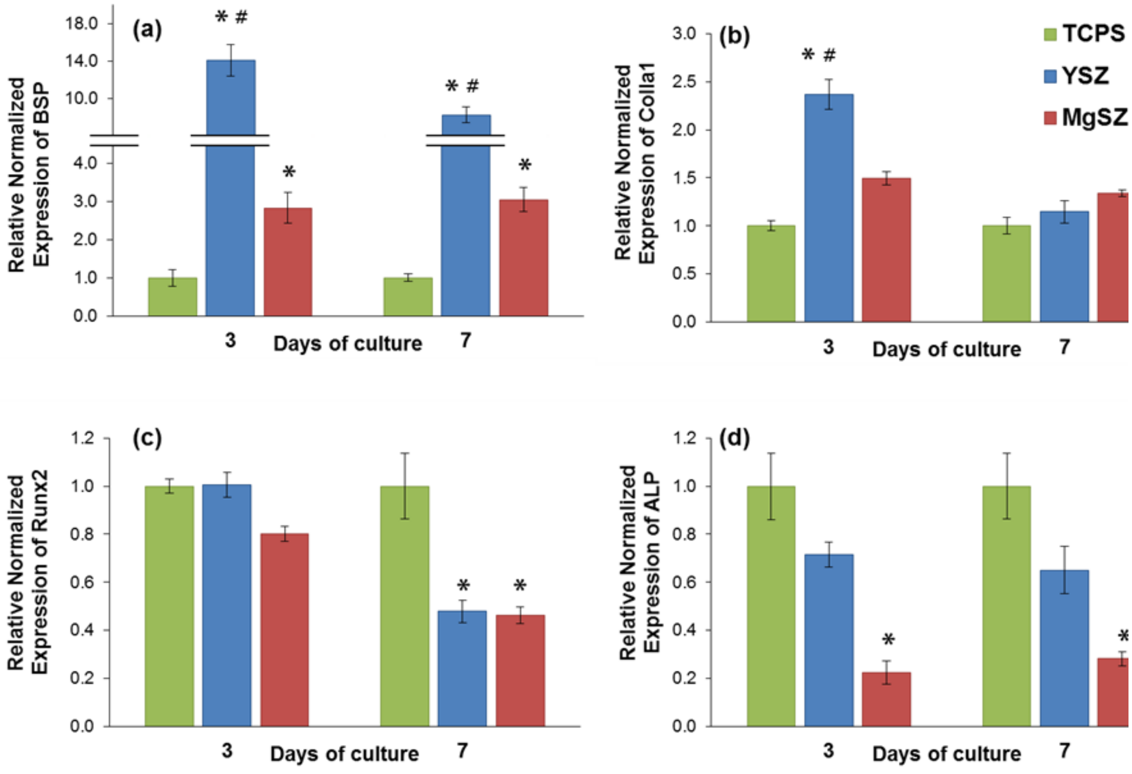

**Figure 5.7. mRNA expression levels of (a) *Bsp*, (b) *CollaI*, (c) *Runx2* and (d) *Alp* in cells cultured on ceramic substrates or TCPS control for 3 or 7 days.** Expression levels were normalized to the *Hprt* housekeeping gene. Each bar represents the mean ± SEM, of triplicate technical and duplicate biological samples in two independent experiments n=12; ${}^{\#}p < 0.001$ vs. MgSZ; ${}^{*}p < 0.001$ vs. TCPS.

*Runx2* mRNA expression was comparable on day 3 among all samples, but on day 7 changes were significant, showing a decreased expression on porous scaffolds. The levels of *Alp* expression in the porous scaffolds were decreased relative to expression levels on TCPS, but this difference was significant only for MgSZ.

## 5.4.6 Calcium mineralization

Calcium deposition through mineralization is a marker of the late differentiation of osteoblasts. We used Alizarin Red to stain calcium deposits in the extracellular matrix after 21 days of culture in the presence of osteogenic medium. As shown in Figure 5.8, the extracted calcium-dye complex by cetylpyridinium chloride was high for both ceramic materials. Normalized calcium deposition was similar for both substrates and overall higher than on TCPS control.

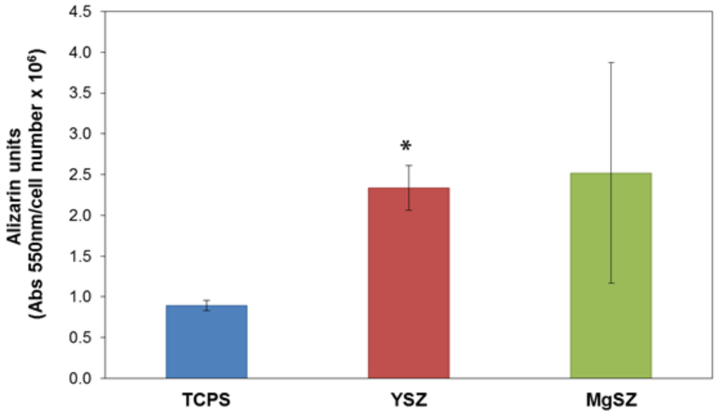

**Figure 5.8. Calcium mineralization by Alizarin Red S staining of MC3T3 cells cultured on ceramic scaffolds or control TCPS for 21 days.**
The calcium-dye complex was extracted into a cetylpyridinium chloride solution and quantified. It is expressed as units of Alizarin red (1 unit is equivalent to 1 optical density unit at 550 nm), normalized to cell number. Each bar represents the mean ± SEM of triplicate samples (n=3); $*p < 0.05$ vs. TCPS.

## 5.5 Discussion

In the present study, we studied two porous zirconia ceramics in which either yttrium oxide ($Y_2O_3$) or magnesium oxide (MgO) was used as dopant. Their microstructure was mostly granular, interrupted by small (~1 µm) and large pores (~150 µm), and showed a high degree of surface topography. In this study, MgSZ porous scaffolds were found to exhibit a “brain-like” microstructure, as previously observed [127], unlike YSZ which was mostly granular. Both porous scaffolds displayed a high degree of open porosity and good interconnectivity believed to be beneficial to cell migration and growth, as it facilitates fluid circulation and nutrient supply. This is supported by several previous studies on hydroxyapatite (HA) and calcium phosphate ceramics, which stress the pivotal role of an open porous structure to implant fixation [4, 33, 38]. The porous YSZ and MgSZ ceramics exhibit good mechanical properties in relation to bone; the elastic modulus values of YSZ and MgSZ match those of cortical bone (3-20 GPa) [94]. Modulus matching is important as it reduces stress-shielding between the implant and the bone in load-bearing applications [120]. Between the two ceramics, YSZ had the highest compressive strength at 240 MPa versus 120 MPa for MgSZ. This is expected due to the intrinsically higher strength of yttria stabilized zirconia [128]. These values are also substantially higher than those previously reported for highly porous (74-87% porosity) zirconia scaffolds (7-9 MPa) [98], which were used as framework for HA coating, resulting in increased mechanical properties compared to an all HA scaffold.

The biological performance of the zirconia ceramics was evaluated in terms of their ability to support cell attachment, proliferation and osteogenic response, as compared to tissue culture treated polystyrene (TCPS). Specifically, MC3T3-E1 pre-osteoblasts were used to investigate the adhesion morphology, growth, alkaline phosphatase activity, collagen secretion and expression profile of four genes involved in bone metabolism, of cells seeded on porous ceramics. The clonal mouse pre-osteoblastic MC3T3-E1 cell line was selected for this study, as it is an excellent model for osteogenic differentiation studies, due to its ability to differentiate and form a well mineralized matrix containing bone markers, such as collagen type I, alkaline phosphatase and bone sialoprotein [66].

Initial cell adhesion is essential to subsequent proliferation [106], whereas cellular morphology affects the osteogenic differentiation of bone cells and it can be even useful in evaluating osteogenic potential [129]. Pre-osteoblastic cell adhesion on YSZ and MgSZ porous scaffolds was found to be supported by both materials, however with distinct morphological characteristics and notably, the presence of a high number of spindle-like filopodia on cells grown on MgSZ in comparison with cells on YSZ which attached tightly and appeared more flattened. The transformation of a cell from spherical to spread-out shape, observed on both ceramics, is important for cell survival and it is acknowledged that cells undergo significant changes when attaching and spreading on substrates [105]. However, bivalent trace metals in the microenvironment of biomaterial surfaces influence initial cell-surface interactions and may also affect the responsiveness of osteoblasts to microtopography, as it has been shown for zinc ions [130]. In addition, Mg ions play important roles in the binding interactions of fibronectin and vitronectin, which may explain the different morphology of cells cultured on MgSZ [131].

A fully spread, flat cell morphology, was reported to be better with respect to cell proliferation and differentiation [107]. The Presto Blue cell proliferation assay results showed that despite initial cell morphological differences, both porous scaffolds promoted proliferation, but cell numbers were higher on YSZ. Growth on porous ceramics was also confirmed qualitatively by CFSE living cell staining, whereas SEM results showed the formation of a smoother, more uniform ECM on YSZ as compared with MgSZ, after 10 days of culture. When comparing proliferation results, the higher cell numbers measured on TCPS, are consistent with previous reports on osteoblast growth on two-dimensional implant materials and porous scaffolds [93, 101]. This may be explained by the permeability of porous scaffolds, which allows some cells to adhere to the underlying well surface, thereby reducing the initial cell number attaching to the scaffolds. However, following the initial cell adhesion, pre-osteoblasts proliferated at a higher growth rate on the porous scaffolds than on TCPS. Similar results have also been reported in previous studies [93], and may be attributed to the greater available space for cell growth provided by the porous interconnected structure.

The ability of porous YSZ and MgSZ to promote osteogenic differentiation was a major focus of this study. Early-phase cell differentiation, as observed by the significant increase in ALP activity, was positively impacted by cell interactions with both YSZ and MgSZ scaffolds. In spite of a higher ALP activity on YSZ on day 14, there was no difference between the two materials on day 21. Furthermore, ALP activity on day 21 was higher on porous scaffolds than on TCPS. In comparison, the pattern of ALP activity on TCPS controls, consisted of a significantly higher activity on day 14, followed by a considerable decrease on day 21, which is typical of the ALP expression during the early stages of differentiation [99]. This is also in agreement with another report [132] demonstrating higher ALP activity of osteoblast-like HOS cells on a highly porous zirconia scaffold versus TCPS after 3 weeks of culture. However, only day 21 results were reported in that study.

Collagen accumulation in the extracellular environment of the cells is a hallmark of osteoblast differentiation. It takes place during an intermediate phase in osteoblast differentiation, and contributes to the formation of extracellular matrix in which mineralization can occur [75]. The quantification of secreted collagen in the supernatant of cells grown on YSZ and MgSZ revealed a positive impact by MgSZ (as compared to TCPS) and a substantial enhancement by YSZ. Together, these results suggest that besides an increase in alkaline phosphatase activity, the high collagen secretion within the porous ceramics would allow for mineralization to occur, as it is necessary to phosphorylate the collagen molecule to allow for calcium deposition [133].

Real-time qPCR analysis of markers of *Alp*, *Runx2*, *CollaI* and *Bsp* was carried out to evaluate the impact of the porous scaffolds on the osteogenic gene expression. BSP is one of the most important non-collagenous proteins of bone. It is a highly glycosylated and sulphated phosphoprotein found almost exclusively in mineralized connective tissues [134] and its expression coincides with *de novo* mineralization. The Runt-related transcription factor 2 (RUNX2) protein has been shown to be an essential transcription factor for osteoblast differentiation, regulating the expression of major bone matrix genes during the early stage of osteoblast differentiation, but RUNX2 is not essential to maintain these gene expressions in mature osteoblasts [135]. *Runx2* gene expression is up-regulated in immature osteoblasts, but down-regulated in mature osteoblasts as RUNX2 inhibits osteoblast maturation and mature bone formation. ALP has a primary biological function in bone formation by its ability to catalyze the hydrolysis of organic phosphate esters, thereby providing inorganic phosphate, or by removing the inorganic pyrophosphate that inhibits calcification at the site of active mineralization [136]. It is known that type I collagen synthesis and collagen accumulation are uncoupled in the developing osteoblast [137]. The collagen gene *CollaI* (a1 chains of type I collagen) is moderately expressed at the beginning of the culture (peaks at day 3), but the levels gradually decrease during differentiation of MC3T3 cells. Instead, as collagen biosynthesis is diminishing, matrix accumulates maximally after 7 days of culture.

Interestingly, our results showed a strong increase in *Bsp* mRNA expression as early as day 3 on both porous scaffolds, with highest levels on YSZ. At the same time, the decrease detected in *Runx2* expression, along with a small decrease in *CollaI* expression on day 7, confirm that both porous YSZ and MgSZ ceramics were able to stimulate osteogenic differentiation of MC3T3 pre-osteoblasts in culture medium supplemented with ascorbic acid and glycerophosphate. *Alp* expression was found unchanged from day 3 to day 7 on either TCPS or porous scaffolds, and mRNA levels were lower in MgSZ. It was previously reported that *Alp* mRNA expression in MC3T3 osteoblasts increases later in culture, which may be an explanation [138].

# Chapter 6

## 6 The potential of calcium phosphate nanoparticles carrying phBMP-7 DNA to transfect MC3T3-E1 pre-osteoblasts and induce an osteogenic response

Chapter based on:

Calcium phosphate nanoparticles carrying BMP-7 plasmid DNA induce an osteogenic response in MC3T3-E1 pre-osteoblasts

*Chrystalleni Hadjicharalambous,[1] Diana Kozlova,[2] Viktoriya Sokolova,[2] Matthias Epple,[2] and Maria Chatzinikolaidou[1,3]*

[1]Dept. of Materials Science and Technology, University of Crete, Heraklion, Greece
[2]Inorganic Chemistry, Center for Nanointegration Duisburg-Essen (CeNIDE), University of Duisburg-Essen, Essen, Germany
[3]IESL-FORTH, Heraklion, Greece

*Published, J Biomed Mater Res Part A, 06/2015; DOI:10.1002/jbm.a.35527*

## 6.1 Introduction

Calcium phosphates constitute a major class of compounds for synthetic bone substitution materials, due to their chemical similarity to bone mineral. During the last decade, calcium phosphate nanoparticles are being explored for biomedical applications, as transfection agents, as drug delivery systems, or as bone substitution materials as discussed in Chapter 1, section 1.5.2.

In this study, we used calcium phosphate nanoparticles that carry plasmid DNA which encodes for human bone morphogenetic protein 7 (hBMP-7), for transfection of pre-osteoblasts. As an osteoinductive growth factor, BMP-7 is in the focus of current research to enhance the bioactivity of bone grafts [139]. Local gene delivery can induce the production of specific proteins (in this case an osteogenic growth factor) by surrounding cells, typically in the environment of the implantation site. The processes of bone growth are subsequently activated by transfected cells that produce these proteins.

The calcium phosphate nanoparticles CaP/PEI/phBMP-7/$SiO_2$-SH were prepared by the group of Prof. Epple at the University of Duisburg-Essen, and for the *in vitro* studies, we employed the mouse calvarial embryonic pre-osteoblastic cell line MC3T3-E1. Our focus was on the transfection efficiency, its duration and also on the ability of the nanoparticles to induce characteristic osteogenic markers in the pre-osteoblastic cells MC3T3-E1.

## 6.2 Materials and Methods

Details on the nanoparticle preparation procedures are described in Appendix II.

### 6.2.1 Transfection of MC3T3-E1 cells with CaP/PEI/phBMP-7/$SiO_2$-SH

Cell culture materials and maintenance of MC3T3-E1 cells are described in Chapter 3, section 3.2.2, page 79. In order to evaluate the transfection efficiency and the effects of calcium phosphate nanoparticle transfection on MC3T3-E1 proliferation and osteogenic response, cells were harvested from tissue culture treated flasks (Corning) and seeded at a density of $25 \times 10^3$ cells per well (96-well plate) or $10^5$ cells per well (24-well plate) or

$5 \times 10^5$ cells per well (6-well plate). Cells were allowed to adhere in primary culture medium (α-MEM with 10% FBS) for 24 h. The medium in each well was replaced with fresh primary medium containing CaP/PEI/phBMP-7/$SiO_2$-SH nanoparticles (pDNA concentration was 50 µg $mL^{-1}$). The total added volumes of medium containing nanoparticle dispersion were 108 µL, 540 µL and 864 µL for the 96-, 24-, and 6-well plates, respectively. The amount of pDNA per well was 0.4 µg, 2.0 µg and 3.2 µg for the 96-, 24-, and 6-well plates, respectively. Seven hours later, the transfection solution was replaced with primary culture medium. As controls, we used cells incubated with calcium phosphate nanoparticles without DNA (CaP/PEI/$SiO_2$-SH) as well as cells cultured in either primary or osteogenic medium (primary medium supplemented with 10 mM *β*-glycerophosphate and 50 µg $mL^{-1}$ ascorbic acid) alone.

The transfection efficiency was determined by fluorescence microscopy, using cells transfected with CaP/PEI/pEGFP/$SiO_2$-SH nanoparticles in 24-well plates. The transfection efficiency was computed by visually counting the proportion of green fluorescing cells in the case of EGFP in fluorescence microscopic images. The concentrations of secreted hBMP-7 in the cell culture medium at 1, 3 and 5 days following transfection were measured with an ELISA kit (Abcam, UK).

### 6.2.2 Scanning electron microscopy

Calcium phosphate nanoparticles attaching on the membrane of MC3T3-E1 cells were incubated with nanoparticles for 3 hours and visualized by scanning electron microscopy (SEM), following fixation, dehydration, drying and gold sputter-coating, as described in Chapter 3, section 3.2.5, page 81.

### 6.2.3 Cell viability and proliferation assay

The cell metabolic activity of MC3T3-E1 pre-osteoblasts following transfection with calcium phosphate nanoparticles was assessed with the PrestoBlue® assay (Invitrogen, USA). Cells were seeded into 96-well plates and transfected with calcium phosphate nanoparticles as given above. At each time point (1, 3 and 7 days after transfection), the

PrestoBlue® reagent was added directly to the wells (1:10 ratio in culture medium) and incubated at 37 °C for 60 min, before measuring the absorbance (570/600 nm) in a spectrophotometer (SpectraMax M2, Molecular Devices Inc., USA). All values were corrected for background absorbance of the reagent which had not been exposed to cells (blank). Then, the PrestoBlue® reagent was removed from the wells and replaced with fresh culture medium before further incubation of the plates at 37 °C. For each experiment three replicates were used (*n*=3). Data were averaged as standard error of the mean (SEM) for each time point.

## 6.2.4 Osteogenic response assays

### 6.2.4.1 Alkaline phosphatase (ALP) activity

To measure alkaline phosphatase (ALP) activity, the cells were seeded into 96-well plates and transfected with nanoparticles as given above. At 3 and 7 days after transfection, cell layers were lysed and the specific ALP enzyme activity was determined as described in Chapter 4, section 4.2.6, page 94.

### 6.2.4.2 Alizarin Red staining

Calcium-rich deposits representing the final stage of mineralization were stained with Alizarin Red S and quantified by dye extraction. MC3T3-E1 cells in 24-well plates were transfected with nanoparticles and cultured for 14 days as given above. Then, the cells were rinsed twice with PBS and fixed in 4% (*v*/*v*) paraformaldehyde (Sigma-Aldrich) for 20 min, rinsed three times with excess $H_2O$ and stained with 300 µL of 2% (*w*/*v*) Alizarin Red S (pH = 4.1) for 20 min. The stained cells were rinsed six times with $H_2O$ to remove excess stain. The stained cell layers were observed by optical microscopy by means of a Zeiss Axiovert 200 microscope using objective lenses for 10-fold magnifications. To quantify the accumulation of calcium containing deposits in the extracellular matrix, 300 µL 10% (*w*/*v*) cetylpyridinium chloride (CPC) in 10 mM sodium phosphate buffer solution (pH = 7.0) were added to the wells for 1 h under shaking. Aliquots (200 µL) of the dye extract were transferred to a 96-well plate and read in duplicates at 550 nm (SpectraMax M2, Molecular Devices Inc., USA). The Alizarin Red stain released into solution was expressed as units of Alizarin Red (1 unit is equivalent to 1 unit optical density at 550 nm) and normalized to cell number, determined by the PrestoBlue® assay immediately prior to Alizarin Red staining.

#### 6.2.4.3 RNA extraction and quantitative real-time PCR (qPCR)

MC3T3-E1 cells were seeded at a density of 5 × $10^5$ cells in 6-well plates, transfected with nanoparticles and cultured for 1 or 3 days as given above (subsection: *Transfection of MC3T3-E1 cells with CaP/PEI/phBMP-7/$SiO_2$-SH*). Total RNA extraction, cDNA synthesis and real-time quantitative polymerase chain reaction (RT-qPCR) analysis on markers of collagen type I, alpha 1 (*ColI-a1*), alkaline phosphatase (*Alp*), bone sialoprotein (*Bsp*) and runt related transcription factor 2 (*Runx2*) were performed as described in Chapter 5, section 5.2.3, page 113. Expression of each target gene in cells transfected with nanoparticles was calculated relative to the respective untreated control (cells in primary medium) after normalization to hypoxanthine phosphoribosyltransferase (*Hprt*) as housekeeping gene. Triplicate biological and triplicate technical samples were analyzed.

### 6.2.5 Statistical analysis

Values of cellular ALP activity and Alizarin Red staining are presented as mean ± standard error of the mean (SEM). Statistical analysis was performed using the student's *t*-test (GraphPad Prism 5 software). The statistical significance was defined as $p < 0.05$.

## 6.3 Results

Results on the characterization of the nanoparticles are described in Appendix II.

### 6.3.1 Transfection of MC3T3-E1 pre-osteoblasts and hBMP-7 production

To evaluate the ability of pDNA-loaded nanoparticles to transfect MC3T3-E1 cells, we used CaP/PEI/pEGFP/$SiO_2$-SH nanoparticles. A successful transfection was detected by the synthesis of enhanced green fluorescent protein (EGFP) by transfected cells, 2 and 3 days after the transfection experiment [52]. Figure 6.1 (top) shows the EGFP fluorescence of MC3T3 cells that was visible in about 25% of the cells 3 days after the transfection. The expression of EGFP significantly decreased after 5 days with only 2-3 cells per field of view showing a green fluorescence. At this time point, counting individual cells was not possible anymore due to cell proliferation and the formation of multilayers, but an important reduction in the number of transfected cells was observed (microscopic observation). This result indicates a transient transfection induced by the nanoparticles with DNA.

Next, we studied whether the transfected cells would produce human BMP-7 protein and how long this genetic manipulation would last. Figure 6.1 (bottom) clearly shows that the MC3T3-E1 cells transfected with CaP/PEI/phBMP-7/$SiO_2$-SH nanoparticles started to produce hBMP-7 protein almost immediately after transfection at day 1. High hBMP-7 levels were observed at days 1 and 3, but the production dropped remarkably on day 5. This correlates to the microscopic observations of cells following transfection with EGFP, shown in Figure 6.2. The background level of hBMP-7 detected in non-transfected cells or cells transfected with control nanoparticles was very close to the background level (blank), as expected and reported in an earlier publication by one of the coauthors [139].

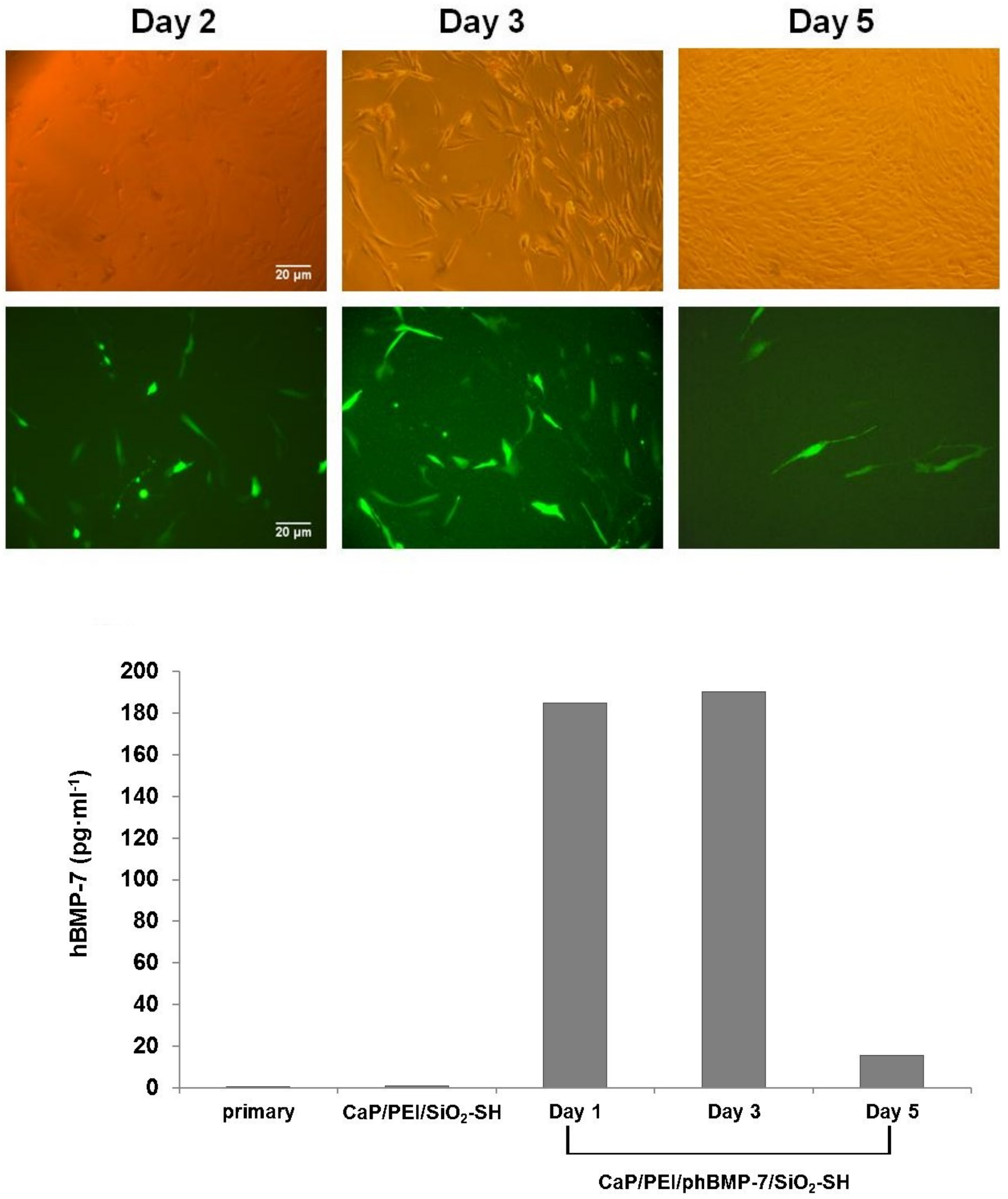

**Figure 6.1. Transfection of MC3T3-E1 cells with CaP/PEI/pDNA/SiO2-SH nanoparticles**

(A) Light microscopy (upper row) and EGFP fluorescence microscopy (lower row) of MC3T3-E1 cells at 2, 3 and 5 days after transfection with CaP/PEI/pEGFP/SiO2-SH nanoparticles (the day of transfection is considered as Day 0). Transfected cells appear green due to expression of EGFP. The number of transfected cells decreased after 5 days, indicating a transient transfection. (B) Expression of hBMP-7 in MC3T3-E1 cells in the cell culture medium after transfection with CaP/PEI/phBMP-7/SiO2-SH nanoparticles. The levels of secreted hBMP-7 were also reduced after 5 days. As controls, we used untreated cells and cells incubated with CaP/PEI/SiO2-SH (day 3). Each bar represents the mean ± SEM of duplicate wells from two experiments.

The accumulation of the nanoparticles on the surface of cells was visualized by scanning electron microscopy (SEM). The SEM images in Figure 6.2 show that a large number of nanoparticles is present at the cell membrane after 3 h incubation.

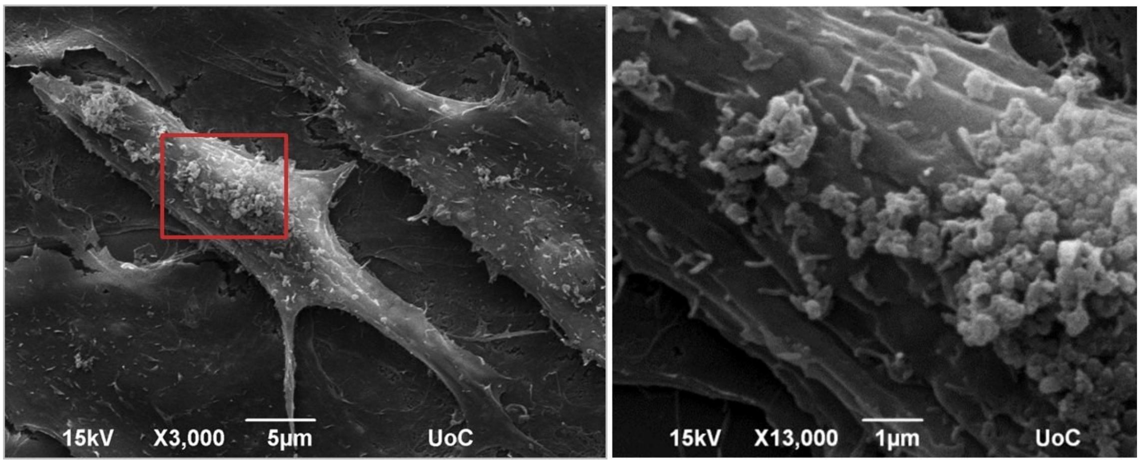

**Figure 6.2. Scanning electron micrographs of CaP/PEI/phBMP-7/$SiO_2$-SH nanoparticles on MC3T3-E1 cells.**
Images are taken after 3 h incubation and thorough washing to remove dispersed or weakly adhering nanoparticles. The image on the right is a magnification of the selected (enclosed in the square) area of the image on the left.

### 6.3.2 Cell viability and proliferation

The metabolic activity of MC3T3-E1 cells following transfection was monitored for 7 days. As shown in Figure 6.3, the nanoparticles did not interfere with cell proliferation. The viability of the cells transfected with nanoparticles loaded with pDNA was comparable with the thiol-functionalized calcium phosphate nanoparticles without pDNA.

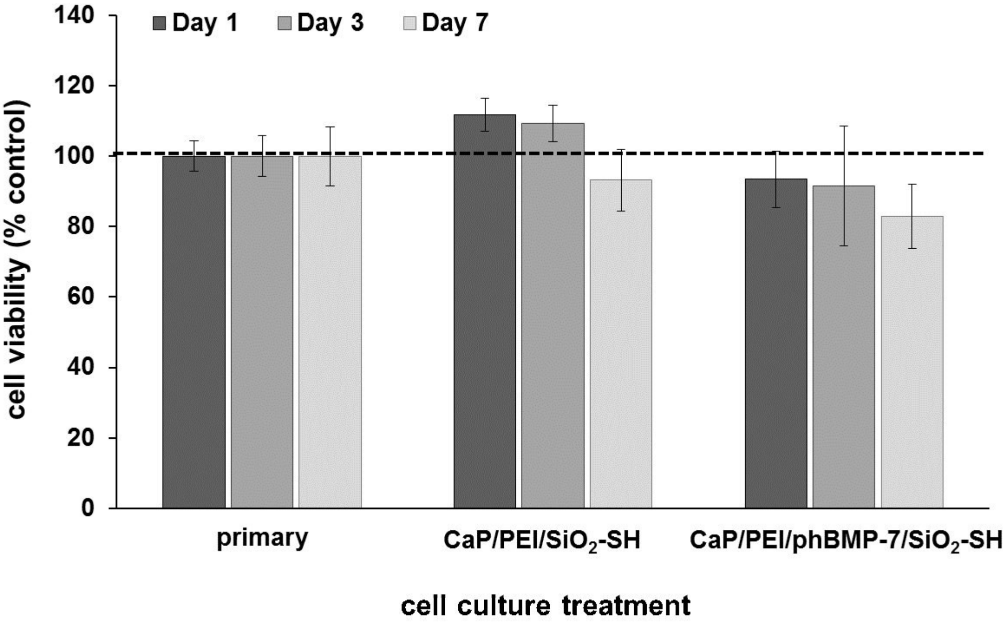

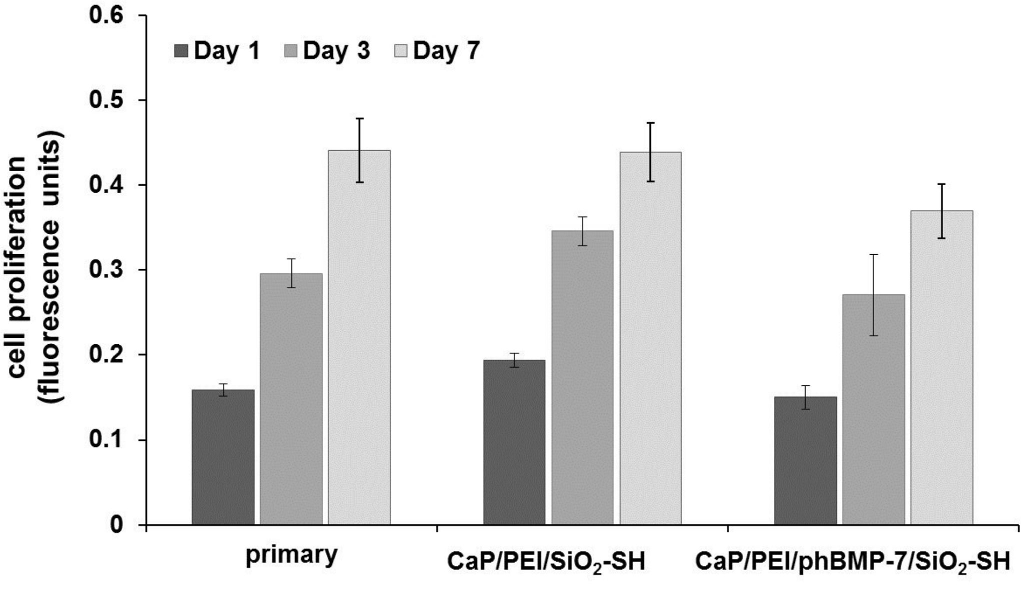

**Figure 6.3. (Top) Cell proliferation and (Bottom) viability of MC3T3-E1 cells after transfection with CaP/PEI/phBMP-7/SiO2-SH nanoparticles.**
At each time point, cell viability was calculated following normalization of fluorescence units to non-treated cells (control) and expressed as a percentage to control (100%). Non-treated cells were cultured in primary (α-MEM with 10% FBS) culture medium. Cells transfected with CaP/PEI/SiO$_2$-SH nanoparticles were used for comparison. Each bar represents the mean ± SEM of triplicate wells from three to five independent experiments.

## 6.3.3 Osteogenic response

We determined the osteogenic responses to CaP/PEI/phBMP-7/$SiO_2$-SH nanoparticle transfection by quantifying alkaline phosphatase (ALP) activity and calcium phosphate deposition as well as by investigating the early mRNA expression levels of different osteogenic markers. CaP/PEI/phBMP-7/$SiO_2$-SH-transfected MC3T3-E1 cells, cultured for 3 days after transfection, showed a significant increase (22 %) in the ALP activity compared to those incubated with CaP/PEI/$SiO_2$-SH control nanoparticles and approximately a 30% increase as compared to non-transfected cells in primary medium (Figure 6.4). On the other hand, ALP activity after 7 days of culture was comparable in nanoparticle-treated as well as in untreated cells.

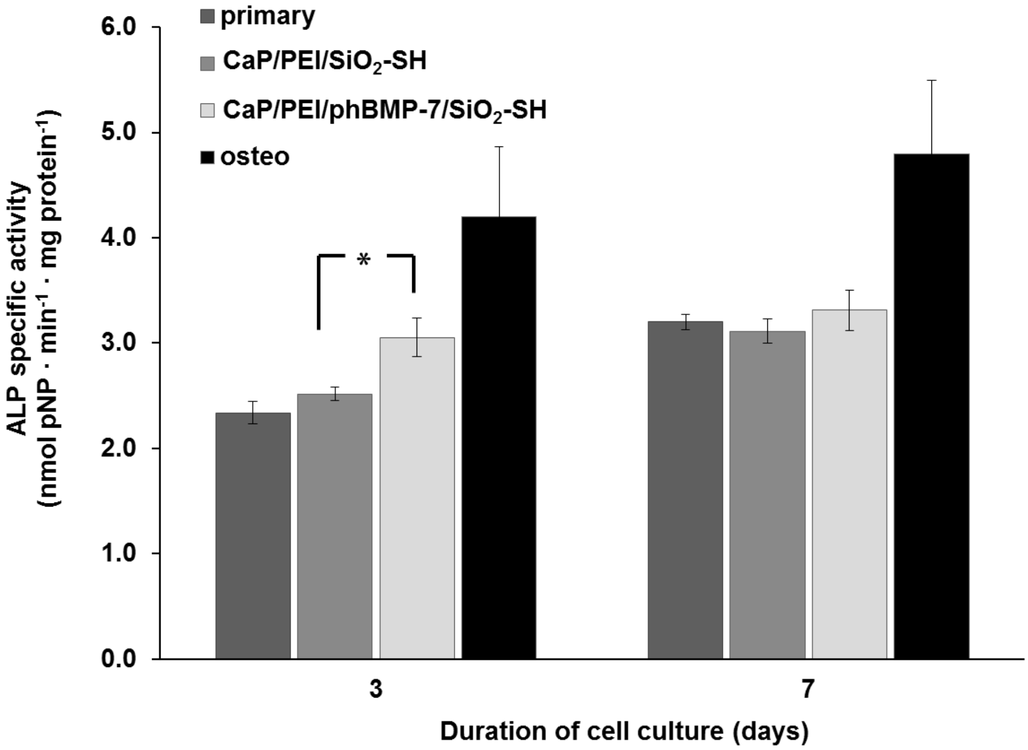

**Figure 6.4. Alkaline phosphatase (ALP) specific activity in nanoparticle treated cultures in primary medium or in non-treated cells (primary).**
Cells cultured in osteogenic media in the absence of nanoparticles (osteo), served as positive control. ALP activity was measured after 3 and 7 days of culture and expressed as nmol min-1 mg protein-1. Each bar represents the mean ± SEM of triplicate wells from three to five independent experiments. An asterisk (*) denotes a significant difference ($p < 0.05$)

To investigate the effect of CaP/PEI/phBMP-7/$SiO_2$-SH transfection to calcium deposition in MC3T3-E1 cells, Alizarin Red staining was used after 14 days of culture. Figure 6.5 shows that CaP/PEI/phBMP-7/$SiO_2$-SH nanoparticles have a positive impact on calcium deposition in cell culture. Their effect is comparable to the effect of osteogenic culture medium (osteo) and about 25% higher than that of nanoparticles without DNA (CaP/PEI/$SiO_2$-SH). Calcium deposition in cell cultures transfected with CaP/PEI/$SiO_2$-SH nanoparticles served as an indicator for possible calcium background from the nanoparticles themselves.

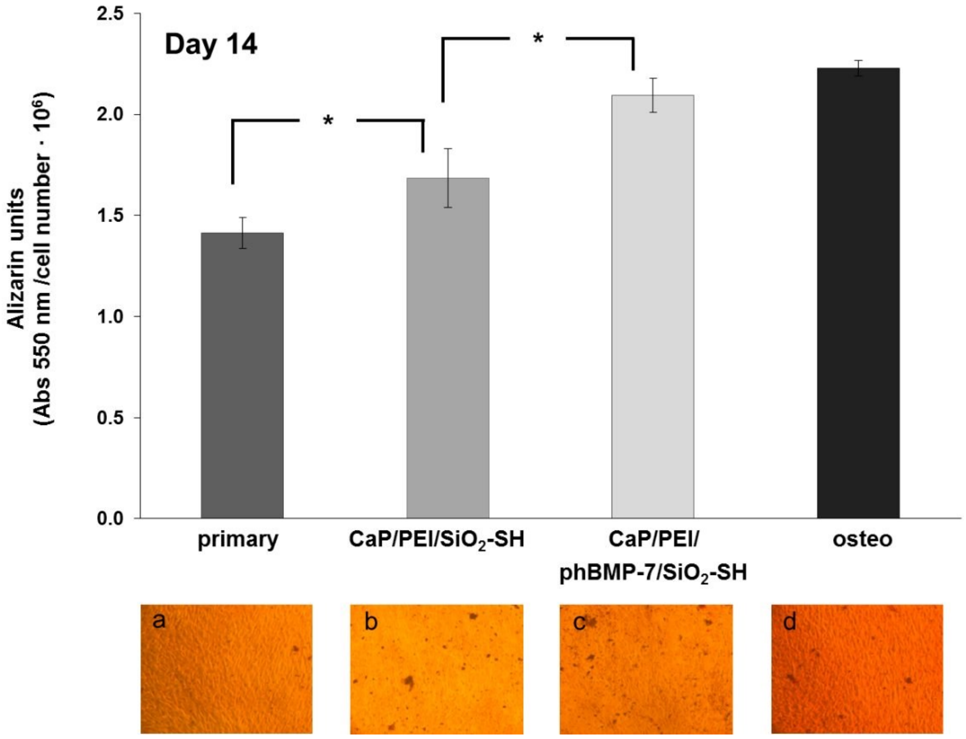

**Figure 6.5. Accumulation of calcium containing deposits in the extracellular matrix of MC3T3E1 cells was determined using the Alizarin Red S assay after 14 days of culture in primary medium in the presence or absence of nanoparticles.** Cells cultured in osteogenic media served as positive control (osteo). The amount of Alizarin Red released in the supernatant of cells was expressed as units of Alizarin Red (1 unit is equivalent to 1 optical density unit at 550 nm), and was normalized to the cell number. Each bar represents the mean ± SEM of triplicate wells from two to four independent experiments. An asterisk (*) denotes significant differences ($p < 0.05$). The micrographs at the bottom of the graph are representative optical microscope images of stained cells before the extraction of Alizarin Red stain; (a) cells in primary medium, cells transfected with (b) CaP/PEI/$SiO_2$-SH or (c) CaP/PEI/phBMP-7/$SiO_2$-SH nanoparticles, and (d) cells in osteogenic medium.

In order to evaluate the bone-related gene expression, we quantified the mRNA expressions of *Alp*, *Runx2*, *CollaI* and *Bsp* genes at 1 or 3 days following transfection of MC3T3-E1 cells with CaP/PEI/phBMP-7/SiO$_2$-SH nanoparticles, control CaP/PEI/SiO$_2$-SH nanoparticles as well as in cells cultured in primary or osteogenic medium. Quantitative real time PCR showed that the expression levels of *Alp*, *Runx2*, *CollaI* and *Bsp* target genes were comparable for the different samples, suggesting that neither up-regulation nor down-regulation occurred (data not shown).

## 6.4 Discussion

In this study, we investigated the transfection and osteogenic response of pre-osteoblastic MC3T3-E1 cells using calcium phosphate nanoparticles as carriers of plasmid human DNA. For this purpose, we employed previously prepared polyethylenimine -stabilized calcium phosphate nanoparticles. The nanoparticles were coated with a shell of silica and covalently functionalized by silanization with thiol groups. Between the calcium phosphate surface and the outer silica shell, plasmid DNA which encoded either for bone morphogenetic protein 7 (BMP-7) or for enhanced green fluorescent protein (EGFP) was incorporated as cargo.

The *in vitro* results showed that such nanoparticles can effectively transfect MC3T3-E1 cells. Transfection experiments employing fluorescence microscopy, showed that the expression of EGFP in cells transfected with nanoparticles, which carry plasmid DNA encoding for EGFP, decreases sharply 5 days post transfection (Figure 6.1). A similar pattern was detected for secreted human BMP-7 protein quantified by ELISA, following cell transfection with CaP/PEI/phBMP-7/SiO$_2$-SH nanoparticles. It was important to analyze the levels of secreted hBMP-7 in the cell culture supernatant, because synthesis of BMPs in bone tissue is associated with secretion of mature BMPs in the extracellular matrix, where they are temporarily stored and released during bone repair and remodeling. Upon release, BMPs trigger a sequential cascade of events leading to osteogenesis by binding two different types of receptors (I and II) on the cell surface that can activate the Smad cytoplasmic proteins [59]. Clearly, *both fluorescence microscopy and ELISA results confirm that the foreign gene is not stably expressed*. In contrast, it is expressed for a limited time (between 1 and 5 days), demonstrating that it is not permanently integrated into the cell genome and that a *transient transfection* had occurred. After all, for a clinical application, a permanent or stable transfection would be undesirable for safety reasons, as introduced genetic materials are integrated into the host genome and may sustain transgene expression even in daughter cells.

Notably, cell metabolic activity experiments showed that the nanoparticles did not interfere with cell proliferation, regardless of the presence of plasmid DNA as a cargo. This result is in agreement with the low inherent toxicity of calcium phosphate nanoparticles, as previously reported [5]. Following transfection with CaP/PEI/phBMP-7/$SiO_2$-SH nanoparticles, the hBMP-7 protein detected in cell culture supernatants was found to induce an osteogenic response as evidenced by the increased alkaline phosphatase (ALP) activity and increased calcium deposition. The role of ALP enzyme as an early marker for osteogenic activity has been consistently confirmed by numerous reports [80]. On the other hand, qPCR experiments showed an absence of early gene expression regulation, which may be explained by the relatively low levels of hBMP-7 secreted in cell culture supernatants of transfected cells. Exogenous human BMP7 added to MC3T3-E1 cultures, has been previously shown to induce the expressions of *Alp*, *Runx2*, and *ColIa1* markers in a dose- and time-dependent manner [62]. However, the range of concentrations in which the induction potential of hBMP-7 was investigated (10-400 ng $mL^{-1}$) in a previously published study [62], was much higher than the concentration measured in the transfected cell culture supernatants in our experiments (200 pg $mL^{-1}$). This difference may explain why we did not observe an increased gene expression in cells transfected with CaP/PEI/phBMP-7/$SiO_2$-SH nanoparticles. In addition, in the present study, ascorbic acid or β-glycerophosphate were not included in nanoparticle treated cell cultures in order to capture solely the effect of hBMP-7 produced after transfection. In contrast, osteogenic conditions were used in previous studies alongside exogenous addition of BMP-7 [62]. The use of osteogenic medium (i.e. primary medium supplemented with ascorbic acid and β-glycerophosphate) may have enhanced the observed effect [62], since a synergistic effect between ascorbic acid and BMP-7 was reported to stimulate osteoblast-gene expression, specifically osteocalcin (*Ocn*) and bone sialoprotein (*Bsp*) mRNA levels [140].

With the aim to stimulate bone regeneration, future work is necessary to enhance the transfection efficiency and to achieve higher levels of hBMP-7 produced by transfected cells. Such results would allow the realization of the full potential of functionalized calcium phosphate nanoparticles as transfection agents to improve bone regeneration.

# Chapter 7

# 7 Conclusions & Perspectives

The objective of this thesis was to investigate the *in vitro* cell-material interactions between macroporous (pore size >50 nm) zirconia and alumina ceramics as well as to investigate calcium phosphate nanoparticles and gain insight into their potential as new biomaterials for bone repair applications.

Initially, we studied the effect of porosity on pre-osteoblastic cell adhesion and growth on zirconia and alumina ceramics. We employed ceramics of increasing porosity (17%, 32% and 61% for alumina) and (19%, 32% and 50% for zirconia) and showed that improved adhesion and enhanced proliferation of MC3T3 pre-osteoblasts was achieved by increasing substrate porosity in zirconia ceramics. Our results showed that a *50% porosity and a pore size of 150 µm is beneficial to cellular growth*. This suggests that porosity is an important factor in zirconia ceramics, which can be exploited to render an otherwise bio-inert material into a cell-supporting scaffold. Also, our findings showed that *50% porous zirconia was superior to 61% porous alumina* as it favored better cell spreading, pore infiltration and higher growth.

Focusing on this, we sought to further investigate pre-osteoblastic cell behavior on 50% zirconia and 61% alumina and questioned whether a longer term cellular growth could be sustained (*in vitro* systems can be usually extended up to 3-4 weeks at the maximum, whereas many literature reports depict cellular growth studies on biomaterials that usually extend up to 1 week) inside the porous scaffolds and if it was possible to induce and observe an osteogenic response. Simultaneously, a third material was included: an 80% zirconia-20% alumina composite ceramic of similar porosity (60%), which represents the latest advancement in ceramic biomaterials in terms of mechanical behavior. All materials featured bimodal pore distributions with the Young's modulus and compressive strength values in the range of 3-10 GPa and 60-240 MPa respectively, similar to those of human cortical bone. Therefore, applications in load-bearing sites such as the femur can be envisaged.

Cell attachment was found to be higher on zirconia and the composite material than on alumina, and was associated with a fully flattened cell morphology. This better adhesion was correlated to significantly higher living cell densities on the above materials than on porous alumina, up to 21 days in culture. However, measurements of ALP activity, collagen production and matrix mineralization revealed that *all three porous substrates support in vitro osteogenic response of pre-osteoblasts, though to a different extent*. We conclude that among the three porous ceramics, the zirconia-containing materials display a stronger *in vitro* cellular response.

Considering the clearly observed effect of material chemistry, with porous zirconia displaying superior response, we further investigated zirconia ceramics. Zirconia is usually stabilized with yttria or magnesia as discussed in Chapter 1, and both materials have been used as hip implant components. However, cell behavior on their porous counterparts remains largely unknown. The present study revealed that both porous YSZ (50% porosity) and MgSZ (57% porosity) with similar pore sizes, allow the adhesion, proliferation and stimulate the osteogenic response of MC3T3-E1 cells. We found that viable cell number, collagen secretion, ALP production and gene expression of *BSP* were better on YSZ; however no significant differences were found between the ability of MgSZ and YSZ to regulate the gene expression of *Runx2*, whose levels decreased with culture time indicating a shift towards osteoblast maturation. Apparently, surface chemical differences between porous YSZ and MgSZ exerted an influence over pre-osteoblastic cell attachment, morphology, and their overall capacity for proliferation and differentiation. Despite this, both porous ceramics elicit good biological responses and bear mechanical properties similar to cortical bone, suggesting their potential as scaffolding materials for bone regeneration.

Even though there have been separate studies on alumina and zirconia in the past, to our knowledge, this is the first time these materials are compared in a single study, alongside with the gold standard of cell culture; the TCPS. This has allowed us to conclude that, *concerning pre-osteoblastic cell proliferation and differentiation, zirconia containing porous scaffolds are superior to porous alumina*. In addition, it was confirmed that the beneficial effect of porosity on cell response, as previously well investigated in hydroxyapatite ceramics, also applies to zirconia. Furthermore, due to the inherent stronger mechanical properties of zirconia in comparison to hydroxyapatite (e.g. compressive strength values for dense zirconia and HA are >2000 MPa and 500 MPa, respectively), the medium porosity (50-60%) scaffolds used in this study are profoundly stronger than their hydroxyapatite counterparts: the porous zirconia ceramics used in our study had compressive strengths of about 200 MPa similar to cortical bone, whereas porous HA has strength values of 2-6 MPa, similar to trabecular bone. Therefore, it is suggested that the porous zirconia investigated in this PhD thesis, may be useful as a non-degradable, osteoconductive material for load bearing usage in segmental bone defects.

Research on the biomedical applications of porous (or macroporous as often named) ceramics, similar to the ones investigated in this thesis, is in the early stages. With more knowledge in this area, superior osteoconductivity of various porous ceramics can be achieved more easily, while retaining the appropriate level of mechanical properties to allow optimal performance of the materials. In addition to bone implant applications, porous ceramics may find applications as matrices for cell culture applications as their pores and interconnections favor rapid cell growth. In another approach, porous zirconia could be used as a cell supporting scaffold before implantation into the injury site. Inclusion of bioactive components such as bone morphogenetic proteins could further enhance bone regeneration. Thus, there is much room for the study of porous ceramics and future advances are expected to expand their applications in the biological field.

At the same time, the concept of using ceramic nanoparticles as DNA carriers to positively affect the process of bone formation is gaining new grounds. In this thesis, calcium phosphate nanoparticles loaded with plasmid human DNA that encodes for the formation of BMP-7 were used for transfection of the pre-osteoblastic MC3T3-E1 cells. The cationic nanoparticles showed *high transfection efficiency together with low cytotoxicity*. Following transfection, we showed that hBMP-7 is synthesized and secreted in the cell culture supernatant. As a result, increased levels of alkaline phosphatase and increased calcium deposition in the extracellular matrix of MC3T3-E1 cells were detected. The *cell transfection proved transient*, which is a desirable aspect for temporary gene expression.

We conclude that the nanoparticles used in this study represent a promising tool for therapeutic approaches in the context of bone regeneration. Nevertheless, for gene-based therapy with calcium phosphate nanoparticles to be made available in the clinical setting, major considerations need to be addressed in a multidisciplinary approach [49]. Future studies should expand our knowledge on the metabolism of calcium phosphate nanoparticles in the cells and its interference with physiological reactions. Also, for *in vivo* applications the issue of changing the dispersion medium to blood or tissue needs to be considered, as agglomeration can occur if electrostatic repulsion between the particles decreases due to increased solution ion strength. Overall, calcium phosphate nanoparticles have significant advantages as highly biocompatible systems for gene delivery, and they are expected to play a major role in the future of nanomedicine.

Finally, as biomaterials science is an interdisciplinary field, in which many experts (e.g. mechanical engineers, material scientists, chemists, biologists, medical doctors, and surgeons) collaborate, our knowledge about material properties such as composition, microstructure, and biological performance as well as the ability to control these characteristics is rapidly expanding. It is possible that combinations of different materials, improved in their biomechanical and biological performance, will provide new solutions. A toolbox of procedures and suitable scaffolds as well as growth factor delivery platforms should be made available to the surgeon, to guide the ultimate choice according to the clinical situation.

# 8 Appendices

## 8.1 Appendix I

In this section, the fabrication and characterization of the porous samples used in this PhD, is given in more detail. All ceramic samples were fabricated by sintering and were characterized in terms of porosity, pore size and mechanical properties by the group of Prof. Kulkov at Tomsk State University. Crystallographic characterization by X-ray powder diffraction (XRD) was carried out by Dr Oleg Prymark at the University of Essen.

### 8.1.1 Fabrication of porous ceramics

The ceramic materials used for this study were obtained from powders of $Al_2O_3$, $ZrO_2(MgO)$, or $ZrO_2(Y_2O_3)$ (Siberian Enterprise Chemical Group). In zirconia ceramics, either yttrium oxide ($Y_2O_3$) or magnesium oxide (MgO) was used as dopant at 8% and 3% respectively. Particles were composed of grains of 10-20 nm, and the average particle size was 500 nm. To fabricate the porous zirconia/alumina composite (ZA-60, 80 wt% $ZrO_2$–20 wt% $Al_2O_3$), alumina and zirconia powders were mixed by ball milling for 25 hours to reduce agglomeration and enhance homogeneity. The milled powders were made into slurries using oleic acid as dispersant. To create macroporosity, organic material particles (polyethylene beads of 90-250 µm with a mean size of 150 µm and molar mass

$2.3\times10^6$) were added as pore formers into the powder mixtures at 20 vol.%. These were extracted by burning in an air furnace at 300 ºC for 3 hours (heating rate of 200 ºC/h), generating the desired pores within the microstructure. The ceramic powders were pressed on a hydraulic press under 100 MPa pressure in steel die molds in order to obtain cylindrical (15 mm in diameter, 5 mm in height) forms. Finally, the compacted powder samples (green bodies) were sintered in air at a temperature of 1450 °C in LHT 02/17 High-Temperature Furnaces (Nabertherm) with an isothermal exposure time of 1 or 2 hours depending on sample. During fabrication, it was not possible to absolutely control the level of shrinkage and therefore small variations in porosity were expected.

### 8.1.2 Characterization of porous ceramics

A scanning electron microscope (Philips SEM-515) with an accelerating voltage of 15 kV was used to observe pore morphology and determine pore size distributions on fracture surfaces of the three different ceramics. This quantitative stereology method provides reasonable quantitative information on the pore size of three-dimensional ceramics based on the interpretation of measurements made on two-dimensional planar sections of the material [141]. The pore size distributions were measured using cross-section of images obtained at different magnifications [142] with more than 500 values measured. The total porosity of the samples was calculated by dividing the scaffold density ($\rho_{scaffold}$) by the theoretical material density ($\rho_{material}$) and subtracting the result from one [34, 35]:

$P_{total} = (1-\rho_{scaffold}/\rho_{material}) \times 100.$

The scaffold density was determined by dividing the weight by the volume of the scaffold and the material density is the density of the material of which the scaffold is fabricated (the average densities of fully dense polycrystalline zirconia and alumina are 6.05 g/cm$^3$ and 3.96 g/cm$^3$ respectively). The open porosity, which is the porosity accessible to a liquid, was measured in water using the Archimedes' principle. Ten specimens were measured for each material. Compression tests for mechanical strength were carried out using an Instron-1185 Universal Testing Machine with 100 kN capacity at a strain rate of $3\text{x}10^{-4}$ s$^{-1}$. The stress-strain plots, derived from load displacement data recorded during compression testing, were used to calculate Young's modulus and the compressive strength of samples. At least 5 samples of cylindrical forms of 12 mm in diameter and 15 mm in height were tested for the compression tests. Compression strength values were calculated as the maximum load divided by the cross-sections of the samples. A straight-line segment of the "stress-strain" curves from the compression tests which corresponded to elastic deformation was defined as Effective Young's modulus (E), i.e. it corresponds to the angle of a tangent line slope to a straight-line segment of the «σ-ε» function curve. The accuracy of load detection was better than 10 N, which implies that for test samples with a cross-section of about 100 mm$^2$ the stress determination accuracy was better than 0.1 MPa.

X-ray diffraction (XRD) analysis was used for phase identification and evaluation of coherently diffracted domains (CDD) in the sintered bodies (Figure 8.1). The crystallographic characterization of alumina A-61, zirconia Z-50 and the composite ZA-60 ceramic samples by means of X-ray powder diffraction (XRD) was carried out on a DRON-07 (St. Peterburg Burevestnik production) unit with Cu Kα radiation (λ: 1.5418 Å; 40 kV and 20 mA). The samples were investigated in the range from 10 to 90° 2θ with a step size of 0.02° 2θ with a counting time of 2 sec. As a reference the patterns of $Al_2O_3$ (No: 43-1484) and $ZrO_2$ (No: 79-1764) from the ICDD database were used.

The phase composition of the YSZ and MgSZ samples described in Chapter 5, was investigated by XRD (Figure 8.2). X-ray powder diffraction (XRD) was carried out on a Bruker D8 Advance instrument in Bragg-Brentano mode with Cu Kα radiation (λ: 1.5418 Å; 40 kV and 40 mA). The samples were investigated in the range from 10 to 90° 2θ with a step size of 0.01° 2θ with a counting time of 0.6 s. Rietveld refinement with the program package TOPAS 4.2 from Bruker was performed to determine the weight amount of crystalline phases, their lattice parameters and percentage of substitution, average crystallite size and the crystallographic density. The pattern of monoclinic $ZrO_2$ (#83-0940), cubic $Mg_{0.2}Zr_{0.8}O_{1.8}$ (#75-0345), cubic $MgAl_2O_4$ (#77-1203) and tetragonal phase $Zr_{0.9}Y_{0.1}O_{1.95}$ (#82-1241) from the ICDD database were used as reference. For each Rietveld refinement, the instrumental correction, as determined with a standard powder sample $LaB_6$ from NIST (National Institute of Standards and Technology) as standard reference material (SRM 660b; a($LaB_6$)=4.15689 Å), was taken into account.

It was found that both ceramics consist of monoclinic phase $ZrO_2$. Additionally, yttrium stabilized tetragonal phase $Zr_{0.89}Y_{0.11}O_{1.95}$ was observed in the YSZ sample (Fig. 2A), whereas magnesia stabilized cubic $Mg_{0.2}Zr_{0.8}O_{1.8}$ and $MgAl_2O_4$ phases were identified in the MgSZ sample (Figure 8.2). These phases were formed during the solid state reactions initiated by the heat treatment. Additionally, a small amount of Al (from EDS) resulted in the building of spinel structure $MgAl_2O_4$.

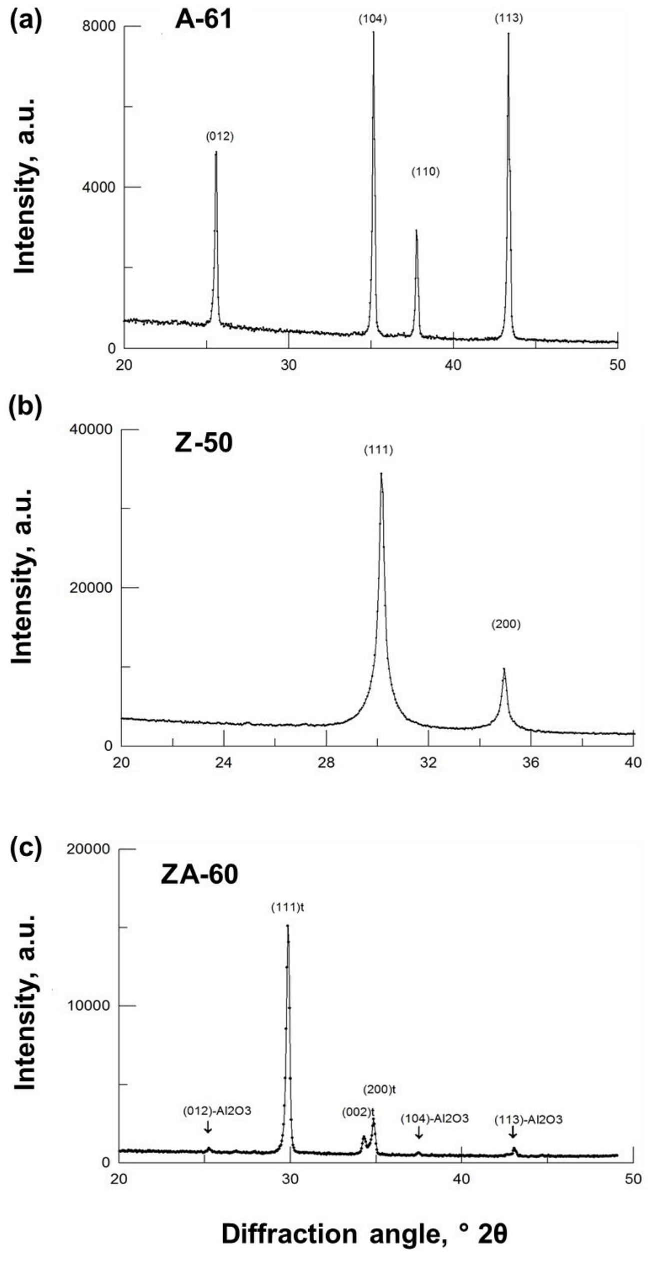

**Figure 8.1. XRD patterns of alumina, zirconia and zirconia-alumina composite ceramics.**
(a) A-61, (b) Z-50 and (c) ZA-60. In the planes (111)t, (002)t and (200)t in (c), t symbolizes the tetragonal structure of the $ZrO_2$ phase, whereas the $Al_2O_3$ designated planes correspond to the corundum phase of alumina.

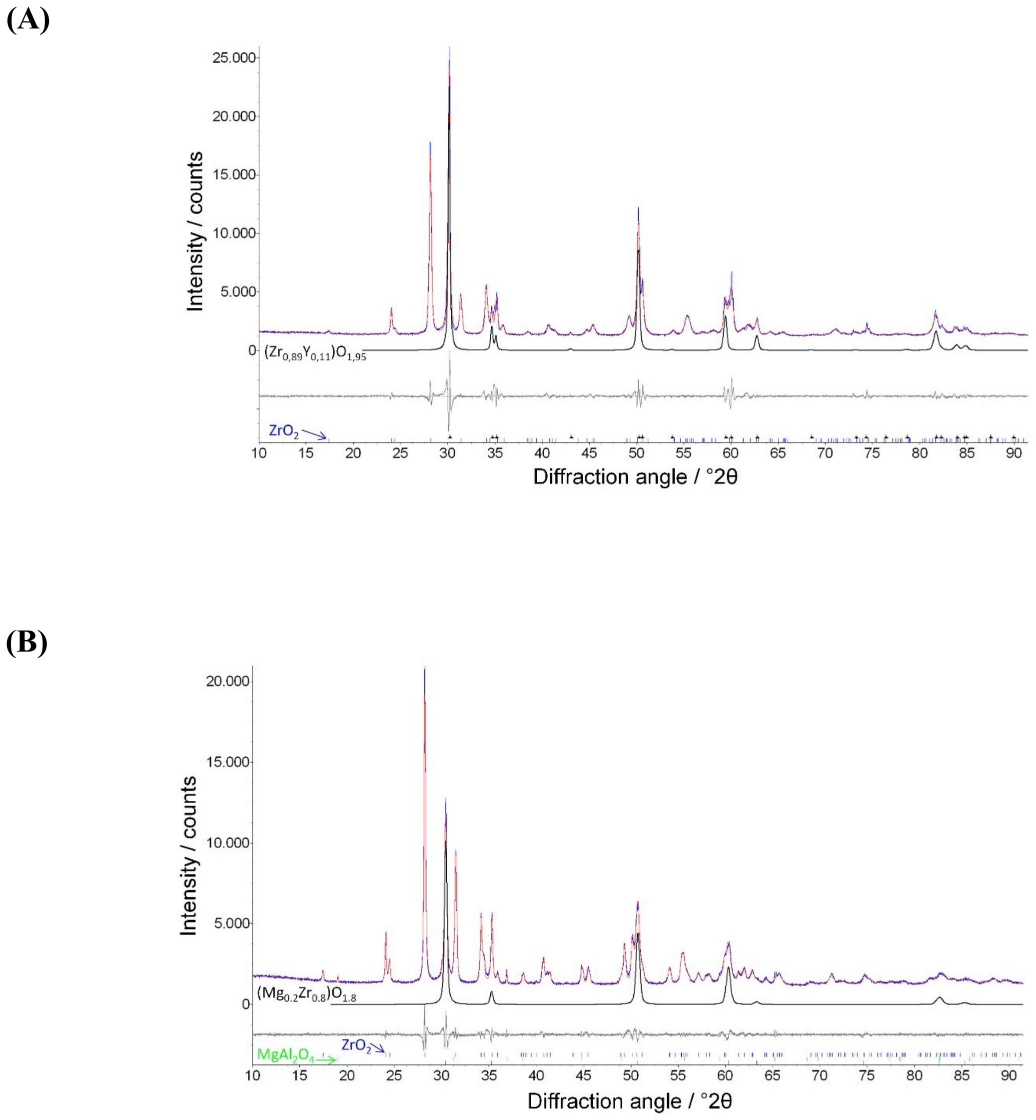

**Figure 8.2. XRD patterns of yttria-stabilized and magnesia-stabilized zirconia ceramics.**

X-ray diffractograms of YSZ and MgSZ ceramics (A) YSZ ceramic (with profile and difference plot from Rietveld refinement, Rwp =6.2) with additionally denoted tetragonal phase $Zr_{0.89}Y_{0.11}O_{1.95}$ and (B) MgSZ ceramic (with profile and difference plot from Rietveld refinement, Rwp = 4.1) with additionally denoted cubic phase $Mg_{0.2}Zr_{0.8}O_{1.8}$.

## 8.2 Appendix II

In this section, the preparation and characterization procedures for the nanoparticles used in this PhD thesis, are given in more detail. These experiments were carried out by the research group of Prof. Matthias Epple at the University of Duisburg-Essen, Germany.

### 8.2.1 Preparation and characterization of functionalized calcium phosphate nanoparticles

Thiol-functionalized calcium phosphate nanoparticles were loaded with either human plasmid-BMP-7 or with plasmid-EGFP as reported earlier [143]. Aqueous solutions of calcium lactate (18 mM, pH=10, p.a., Merck), diammonium hydrogen phosphate $(NH_4)_2HPO_4$ (10.8 mM, pH=10, p.a., Merck), and PEI (2 g $L^{-1}$, $M_W$=25 kDa, Aldrich) were simultaneously pumped in a volume ratio of 5 mL : 5 mL : 7 mL into a stirred glass vessel containing 20 mL of ultrapure water during 1 min. After the stabilization with polyethylenimine (PEI), 3.6 mL of the nanoparticle dispersion was mixed with 400 µL of aqueous solutions of either plasmid-human BMP-7 (1 mg $mL^{-1}$) or plasmid-EGFP (1 mg $mL^{-1}$) under stirring, followed by stirring for 30 min at room temperature. For coating with a silica shell, 4 mL of the nanoparticles dispersion with or without plasmid were added to a mixture of 16 mL ethanol, 20 µL tetraethyl orthosilicate (TEOS, Sigma-Aldrich) and 11 µL of aqueous ammonia solution (30-33 wt% $NH_3$). This reaction mixture was then stirred at room temperature for 16 h. The particles were isolated by ultracentrifugation at 66,000 g for 30 min and redispersed in 4 mL of water (the original volume) under ultrasonication (UP50H, Hielscher, Ultrasound Technology; sonotrode 7, cycle 0.8, amplitude 70%, 4 s). For further functionalization with thiol groups, 4 mL of silica-modified nanoparticle dispersion either with or without plasmid, was added to a mixture of 16 mL ethanol and 20 µL (3-thiol propyl) trimethoxysilane (MPS, Sigma-Aldrich) or stirred at room temperature for another 8 h. Then, the dispersion was purified by ultracentrifugation and the nanoparticles were redispersed by ultrasonication with the same parameters as given above (UP50H, Hielscher, Ultrasound Technology; sonotrode 7, cycle 0.8, amplitude 70%, 4 s).

For storage and transport, the dispersions were freeze-dried. 20 mg of D-(+)-trehalose dihydrate (Aldrich) was added to 1 mL of the nanoparticle dispersion (either CaP/PEI/pEGFP/$SiO_2$-SH, CaP/PEI/phBMP-7/$SiO_2$-SH or CaP/PEI/$SiO_2$-SH), which was then shock-frozen with liquid nitrogen. The solid material was then lyophilized at 0.31 mbar and -7 °C for 72 h [144].

Ultrapure water (Purelab ultra instrument, ELGA) was used for all preparations. All formulations were prepared and analyzed at room temperature. The morphological characteristics of the particles were obtained by scanning electron microscopy (ESEM Quanta 400) with gold/palladium-sputtered samples. Dynamic light scattering and zeta potential determinations were performed with a Zetasizer Nano Series instrument (Malvern Nano-ZS, $\lambda$ = 532 nm). The particle size data refer to scattering intensity distributions (z-average).

The particle size distribution of the nanoparticles either with or without DNA, was investigated with dynamic light scattering. The calcium phosphate nanoparticles without DNA had an average diameter of about 160 nm. The diameter of pDNA-loaded nanoparticles was 262 nm (phBMP-7-loaded) and 289 nm (pEGFP-loaded), respectively. The zeta-potential of thiol-functionalized calcium phosphate nanoparticles (both with and without DNA) was +24 mV (cationic).

Scanning electron micrographs of the nanoparticles are shown in Figure 3. The nanoparticles had a spherical shape with a core diameter up to 150 nm. Note that in SEM, the hydration layer of functionalized nanoparticles is not visible, therefore the particles are smaller than when measured by dynamic light scattering (DLS). However, the factor 2 difference between the hydrodynamic diameter as determined by DLS and the diameter of the solid core as determined by SEM, suggests that some agglomeration of the nanoparticles occurs in aqueous dispersion.

The inorganic part of the calcium phosphate nanoparticles was determined by measuring the calcium concentration in the dispersion by atomic absorption spectroscopy. For the calculation of the concentration of calcium phosphate in the dispersion, we used the stoichiometry of hydroxyapatite, $Ca_5(PO_4)_3(OH)$ as the most common calcium phosphate [145]. The concentration of calcium phosphate in the dispersion was 177 $\mu g\ mL^{-1}$, 132 µg mL$^{-1}$ and 145 µg mL$^{-1}$ for nanoparticles without DNA, nanoparticles with phBMP-7 and nanoparticles with pEGFP, respectively. In order to estimate the number of nanoparticles per volume and per cell during the transfection experiments, we first calculated the number of nanoparticles in 1 mL of colloid. Taking the average primary particle diameter of 120 nm from the scanning electron microscopy data, we computed a particle concentration of $6.2 \times 10^{10}$ mL$^{-1}$ for nanoparticles without DNA and $4.6 \times 10^{10}$ mL$^{-1}$ and $5.1 \times 10^{10}$ mL$^{-1}$ for nanoparticles with phBMP-7 and pEGFP, respectively. The average number of nanoparticles per cell after dilution in the well was $5.0 \times 10^4$ for nanoparticles without DNA, and $3.7 \times 10^4$ and $4.1 \times 10^4$ for calcium phosphate nanoparticles with phBMP-7 and pEGFP, respectively. The number of nanoparticles per cell computed in this way is different than the number of nanoparticles that were effectively taken up by each cell.

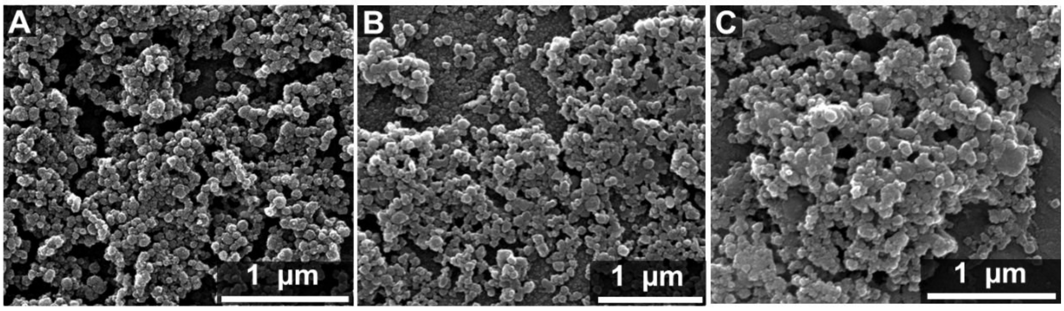

**Figure 8.3. Scanning electron micrographs of calcium phosphate nanoparticles.** (**A**) without pDNA or (**B**) with pEGFP or (**C**) with phBMP-7 encoding DNA.

# 9 Scientific Contributions

## Publications

**Chrystalleni Hadjicharalambous**, Ales Buyakov, Svetlana Buyakova, Sergey Kulkov and Maria Chatzinikolaidou. Porous alumina, zirconia and alumina/zirconia for bone repair: Fabrication, mechanical and *in vitro* biological response.
*Published, Biomed. Mater. 10 (2015) 025012.*

**Chrystalleni Hadjicharalambous**, Evdokia Mygdali, Oleg Prymak, Ales Buyakov, Sergey Kulkov and Maria Chatzinikolaidou. Proliferation and osteogenic response of MC3T3-E1 pre-osteoblastic cells on porous zirconia ceramics stabilized with magnesia or yttria.
*Published, J Biomed Mater Res Part A 2015:00A:000–000. DOI: 10.1002/jbm.a.35475*

**Chrystalleni Hadjicharalambous**, Diana Kozlova, Viktoriya Sokolova, Matthias Epple, and Maria Chatzinikolaidou. Calcium phosphate nanoparticles carrying BMP-7 plasmid DNA induce an osteogenic response in MC3T3-E1 pre-osteoblasts.
*Published, J Biomed Mater Res Part A, 06/2015; DOI:10.1002/jbm.a.35527*

**Chrystalleni Hadjicharalambous**, Oleg Prymak, Kateryna Loza, Sergey Kulkov and Maria Chatzinikolaidou. A porosity effect on the adhesion and proliferation of pre-osteoblasts on alumina and zirconia ceramics.
*Manuscript to be submitted*

# Conference presentations

**Chrystalleni Hadjicharalambous**, Victoria Sokolova, Diana Kozlova, Matthias Epple and Maria Chatzinikolaidou. Calcium phosphate nanoparticles carrying BMP-7 plasmid DNA induce osteogenic differentiation of MC3T3-E1 pre-osteoblasts. 26th European Conference on Biomaterials, Sept. 2014, Liverpool, UK.

**Chrystalleni Hadjicharalambous**, Vladimir Promakhov, Svetlana Buyakova, Sergey Kulkov and Maria Chatzinikolaidou. Adhesion, Growth and Differentiation of Pre-osteoblasts on Novel Porous Magnesia- and Yttria-Stabilized Zirconia Ceramics. 26th European Conference on Biomaterials, Sept. 2014, Liverpool, UK.

**Chrystalleni Hadjicharalambous**, Vladimir Promakhov, Svetlana Buyakova, Sergey Kulkov and Maria Chatzinikolaidou. Mechanical and Biological Characteristics of New Porous Magnesia- and Yttria-Stabilized Zirconia Ceramics. World Congress on Biomechanics, July 2014, Boston, MA, U.S.A

**Chrystalleni Hadjicharalambous**, Maria Kissamitaki, Maria Vamvakaki and Maria Chatzinikolaidou. Initial in vitro interaction of pre-osteoblastic cells on two types of glycopolymer brushes: the influence of chemistry and nanotopography. 3rd International Conference on Tissue Engineering *(ICTE),* June 2013, Leiria, Portugal.

**Chrystalleni Hadjicharalambous**, Vladimir Promakhov, Svetlana Buyakova, Sergey Kulkov and Maria Chatzinikolaidou. A porosity effect on the adhesion and proliferation of pre-osteoblasts on sintered zirconia ceramics.19th Congress of the European Society of Biomechanics, August 2013, Patras, Greece.

**Chrystalleni Hadjicharalambous**, Vladimir Promakhov, Svetlana Buyakova, Sergey Kulkov and Maria Chatzinikolaidou. Enhanced *in vitro* biological response of a new porous alumina-zirconia composite for bone repair. 25th European Conference on Biomaterials, Sept. 2013, Madrid, Spain.

**Chrystalleni Hadjicharalambous**, A. Mateescu, U. Jonas, M. Chatzinikolaidou. Viability and osteogenic response of pre-osteoblastic cells on poly(N-isopropylacrylamide) functionalized with bone morphogenetic protein 2 (BMP-2). World Conference on Regenerative Medicine, Leipzig 2011, Germany.

# 10 References

1. Brydone, A.S., D. Meek, and S. Maclaine, *Bone grafting, orthopaedic biomaterials, and the clinical need for bone engineering.* Proceedings of the Institution of Mechanical Engineers, Part H: Journal of Engineering in Medicine, 2010. **224**(12): p. 1329-1343.
2. Chevalier, J. and L. Gremillard, *Ceramics for medical applications: A picture for the next 20 years.* Journal of the European Ceramic Society, 2009. **29**(7): p. 1245-1255.
3. Singhatanadgit, W., *Biological Responses to New Advanced Surface Modifications of Endosseous Medical Implants.* Bone and Tissue Regeneration Insights, 2009. **2**(1566-BTRI-Biological-Responses-to-New-Advanced-Surface-Modifications-of-Endosseo.pdf): p. 1-11.
4. Lew, K.S., et al., *Macroporous bioceramics: a remarkable material for bone regeneration.* J Biomater Appl, 2012. **27**(3): p. 345-58.
5. Sokolova, V. and M. Epple, *Inorganic Nanoparticles as Carriers of Nucleic Acids into Cells.* Angewandte Chemie International Edition, 2008. **47**(8): p. 1382-1395.
6. Kozlova, D., et al., *Cell targeting by antibody-functionalized calcium phosphate nanoparticles.* Journal of Materials Chemistry, 2012. **22**(2): p. 396.
7. Pilia, M., T. Guda, and M. Appleford, *Development of Composite Scaffolds for Load-Bearing Segmental Bone Defects.* BioMed Research International, 2013. **2013**: p. Article ID 458253, 15 pages.
8. *Cancellous bone.* Encyclopaedia Britannica. , 2015: p. Retrieved from http://www.britannica.com/EBchecked/topic/92222/cancellous-bone.
9. Boskey, A.L., *Bone composition: relationship to bone fragility and antiosteoporotic drug effects.* BoneKEy Rep, 2013. **2**.
10. Follet, H., et al., *The degree of mineralization is a determinant of bone strength: a study on human calcanei.* Bone, 2004. **34**(5): p. 783-789.
11. Nakamura, H., *Morphology, Function, and Differentiation of Bone Cells.* Journal of Hard Tissue Biology, 2007. **16**(1): p. 15-22.
12. Manolagas, S.C., *Birth and Death of Bone Cells: Basic Regulatory Mechanisms and Implications for the Pathogenesis and Treatment of Osteoporosis1.* Endocrine Reviews, 2000. **21**(2): p. 115137.
13. Williams, D., *Essential Biomaterials Science.* Cambridge University Press, 2014.

14. Deschaseaux, F., L. Sensébé, and D. Heymann, *Mechanisms of bone repair and regeneration.* Trends in molecular medicine, 2009. **15**(9): p. 417-429.
15. Gaston, M.S. and A. Simpson, *Inhibition of fracture healing.* Journal of Bone & Joint Surgery, British Volume, 2007. **89**(12): p. 1553-1560.
16. Gallagher, J.C. and A.J. Sai, *Molecular biology of bone remodeling: implications for new therapeutic targets for osteoporosis.* Maturitas, 2010. **65**(4): p. 301-307.
17. Meling, T., K. Harboe, and K. Søreide, *Incidence of traumatic long-bone fractures requiring in-hospital management: A prospective age- and gender-specific analysis of 4890 fractures.* Injury, 2009. **40**(11): p. 1212-1219.
18. (US)., O.o.t.S.G., *Bone Health and Osteoporosis: A Report of the Surgeon General. Rockville (MD): Office of the Surgeon General (US); The Frequency of Bone Disease. Available from: http://www.ncbi.nlm.nih.gov/books/NBK45515/.* 2004.
19. Kaveh, K., et al., *Bone grafting and bone graft substitutes.* J Anim Vet Adv, 2010. **9**(6): p. 1055-1067.
20. Hench, L.L., *The future of bioactive ceramics.* Journal of materials science. Materials in medicine, 2015. **26**(2): p. 5425.
21. Seebach, C., et al., *Comparison of six bone-graft substitutes regarding to cell seeding efficiency, metabolism and growth behaviour of human mesenchymal stem cells (MSC) in vitro.* Injury, 2010. **41**(7): p. 731-738.
22. Bongio, M., et al., *Development of bone substitute materials: from 'biocompatible'to 'instructive'.* Journal of Materials …, 2010.
23. Hing, K.A., *Bioceramic Bone Graft Substitutes: Influence of Porosity and Chemistry.* International Journal of Applied Ceramic Technology, 2005. **2**(3): p. 184-199.
24. Huebsch, N. and D.J. Mooney, *Inspiration and application in the evolution of biomaterials.* Nature, 2009. **462**(7272): p. 426-432.
25. Bauer, S., et al., *Engineering biocompatible implant surfaces.* Progress in Materials Science, 2013. **58**(3): p. 261326.
26. Rahman, H.S.A., et al., *In vivo and in vitro outcomes of alumina, zirconia and their composited ceramic-on-ceramic hip joints.* Journal of the Ceramic Society of Japan, 2013. **121**(1412): p. 382-387.
27. Hernigou, P. and T. Bahrami, *Zirconia and alumina ceramics in comparison with stainless-steel heads.* The Journal of Bone and Joint Surgery, 2003. **85**(4): p. 504509.
28. Manicone, P.F., P. Rossi Iommetti, and L. Raffaelli, *An overview of zirconia ceramics: basic properties and clinical applications.* J Dent, 2007. **35**(11): p. 819-26.
29. Chevalier, J., *What future for zirconia as a biomaterial?* Biomaterials, 2006. **27**(4): p. 535-43.
30. Azaa, A.H.D., et al., *Crack growth resistance of alumina, zirconia and zirconia toughened alumina ceramics for joint prostheses.* Biomaterials, 2002. **23**(3): p. 937-945.
31. Palmero, P., et al., *Surface Coating of Oxide Powders: A New Synthesis Method to Process Biomedical Grade Nano-Composites.* Materials, 2014. **7**(7).
32. K, K., K. H, and M. T, *Phase change and mechanical properties of ZrO2-Y2O3 solid electrolyte after ageing.* Solid State Ionics, 1981. **3**: p. 489-495.
33. Bignon A, C.J., Chevalier J, Fantozzi G, Carret JP, Chavassieux P, Boivin G, Melin M, Hartmann D., *Effect of micro- and macroporosity of bone substitutes on their mechanical properties and cellular response.* J Mater Sci Mater Med, 2003. **14**(12): p. 1089-1097.
34. Galmarini, S., *Ceramics: Sintering and Microstructure.* Work practices "Ceramics Process": TP3 Sintering, 2011: p. 1-15.
35. Karageorgiou, V. and D. Kaplan, *Porosity of 3D biomaterial scaffolds and osteogenesis.* Biomaterials, 2005. **26**(27): p. 5474-91.
36. Masters, K.S. and K.S. Anseth, *Cell–Material Interactions.* Advances in Chemical Engineering, 2004. **29**: p. 7-46.

37. Thakur, S., et al., *Depth matters: cells grown on nano-porous anodic alumina respond to pore depth.* Nanotechnology, 2012. **23**(25): p. 255101.
38. Lu, J., et al., *Role of interconnections in porous bioceramics on bone recolonization in vitro and in vivo.* Journal of materials science. Materials in medicine, 1999. **10**(2): p. 111-120.
39. Dehestani, M., L. Ilver, and E. Adolfsson, *Enhancing the bioactivity of zirconia and zirconia composites by surface modification.* J Biomed Mater Res B Appl Biomater, 2012. **100**(3): p. 832-40.
40. Mieszawska, A.J. and D.L. Kaplan, *Smart biomaterials - regulating cell behavior through signaling molecules.* BMC Biology, 2010. **8**(1): p. 59.
41. Tautzenberger, A., A. Kovtun, and A. Ignatius, *Nanoparticles and their potential for application in bone.* International Journal of Nanomedicine, 2012. **7**.
42. Panyam, J. and V. Labhasetwar, *Biodegradable nanoparticles for drug and gene delivery to cells and tissue.* Advanced Drug Delivery Reviews, 2003. **55**(3).
43. Mieke, H., et al., *Gene therapy used for tissue engineering applications.* Journal of Pharmacy and Pharmacology, 2007. **59**(3): p. 329-350.
44. Ojea-Jimenez, I., et al., *Engineered nonviral nanocarriers for intracellular gene delivery applications.* Biomed Mater, 2012. **7**(5): p. 054106.
45. Kofron, M.D., X. Li, and C.T. Laurencin, *Protein- and gene-based tissue engineering in bone repair.* Current opinion in biotechnology, 2004. **15**(5): p. 399-405.
46. Kovtun, A., R. Heumann, and M. Epple, *Calcium phosphate nanoparticles for the transfection of cells.* Bio-medical materials and engineering, 2009. **19**(2-3): p. 241-247.
47. Nadav, K., et al., *Review: Gene- and Stem Cell–Based Therapeutics for Bone Regeneration and Repair.* Tissue Engineering, 2007.
48. Jin, S., J. Leach, and K. Ye, *Nanoparticle-Mediated Gene Delivery*, in *Micro and Nano Technologies in Bioanalysis*, R.S. Foote and J.W. Lee, Editors. 2009, Humana Press. p. 547-557.
49. Cai, Y. and R. Tang, *Calcium phosphate nanoparticles in biomineralization and biomaterials.* Journal of Materials Chemistry, 2008. **18**(32): p. 3775.
50. Cao, X., et al., *Encapsulation of plasmid DNA in calcium phosphate nanoparticles: stem cell uptake and gene transfer efficiency.* Int J Nanomedicine, 2011. **6**: p. 3335-49.
51. FL, G. and V.d.E. AJ, *A new technique for the assay of infectivity of human adenovirus 5 DNA.* Virology 1973. **52**: p. 456-467.
52. Sokolova, V.V., et al., *Effective transfection of cells with multi-shell calcium phosphate-DNA nanoparticles.* Biomaterials, 2006. **27**(16): p. 3147-53.
53. Pedraza, C.E., et al., *The importance of particle size and DNA condensation salt for calcium phosphate nanoparticle transfection.* Biomaterials, 2008. **29**(23): p. 3384-3392.
54. Delphine Lechardeur, A.S. Verkman, and G.L. Lukacs, *Intracellular routing of plasmid DNA during non-viral gene transfer.* Advanced Drug Delivery Reviews, 2005. **57**(5): p. 755767.
55. Sokolova, V., et al., *Mechanism of the uptake of cationic and anionic calcium phosphate nanoparticles by cells.* Acta biomaterialia, 2013. **9**(7): p. 7527-7535.
56. Maitra, A., *Calcium phosphate nanoparticles: second-generation nonviral vectors in gene therapy.* Calcium phosphate nanoparticles: second-generation nonviral vectors in gene therapy, 2005.
57. Urist, M.R., *Bone: Formation by Autoinduction.* Science, 1965. **150**(3698): p. 893-899.
58. Giannoudis, P.V. and C. Tzioupis, *Clinical applications of BMP-7.* Injury, 2005. **36**(3).
59. Carreira, A.C., et al., *Bone Morphogenetic Proteins: Facts, Challenges, and Future Perspectives.* Journal of Dental Research, 2014. **93**(4): p. 335345.

60. Qiao, C., et al., *Using poly(lactic-co-glycolic acid) microspheres to encapsulate plasmid of bone morphogenetic protein 2/polyethylenimine nanoparticles to promote bone formation in vitro and in vivo.* Int J Nanomedicine, 2013. **8**: p. 2985-95.
61. Krebs, M.D., et al., *Calcium phosphate-DNA nanoparticle gene delivery from alginate hydrogels induces in vivo osteogenesis.* Journal of biomedical materials research. Part A, 2010. **92**(3): p. 1131-1138.
62. Zhang, F., et al., *The optimal dose of recombinant human osteogenic protein-1 enhances differentiation of mouse osteoblast-like cells: an in vitro study.* Archives of oral biology, 2012. **57**(5): p. 460-468.
63. Griffith, D.L., et al., *Three-dimensional structure of recombinant human osteogenic protein 1: structural paradigm for the transforming growth factor beta superfamily.* Proceedings of the National Academy of Sciences, 1996. **93**(2): p. 878-883.
64. Shore, E.M. and F.S. Kaplan, *Inherited human diseases of heterotopic bone formation.* Nature reviews. Rheumatology, 2010. **6**(9): p. 518-527.
65. Sudo H, et al., *In vitro differentiation and calcification in a new clonal osteogenic cell line derived from newborn mouse calvaria.* J Cell Biol., 1983. **96**: p. 191-8.
66. Wang, D., et al., *Isolation and characterization of MC3T3 E1 preosteoblast subclones with distinct in vitro and in vivo differentiation/mineralization potential.* Journal of Bone and Mineral Research, 1999. **14**(6): p. 893-903.
67. Kodama, H., Amagai, Y., Sudo, H., Yamamoto, S, *Establishment of a clonal osteogenic cell line from newborn mouse calvaria.* Jpn J Oral Biol 1981. **23**: p. 899-901.
68. Gordon;, J.A.R., et al., *Bone sialoprotein expression enhances osteoblast differentiation and matrix mineralization in vitro.* Bone, 2007. **41**(3): p. 462473.
69. Lonnie D. Shea, et al., *Engineered Bone Development from a Pre-Osteoblast Cell Line on Three-Dimensional Scaffolds.* Tissue Engineering, 2000. **6**(6): p. 605617.
70. Vicky Kartsogiannis and K.W. Ng, *Cell lines and primary cell cultures in the study of bone cell biology.* Molecular and Cellular Endocrinology, 2004. **228**(1-2): p. 79102.
71. Lodish H, Berk A, and Zipursky SL, *Molecular Cell Biology, Section 22.3, Collagen: The Fibrous Proteins of the Matrix. .* 4th edition. New York: W. H. Freeman, 2000. **Available from: http://www.ncbi.nlm.nih.gov/books/NBK21582/**.
72. Ricard-Blum, S. and F. Ruggiero, *The collagen superfamily: from the extracellular matrix to the cell membrane.* Pathol Biol (Paris), 2005. **53**(7): p. 430-42.
73. Weizhuo Wang, et al., *Collagen XXIV (Col24α1) promotes osteoblastic differentiation and mineralization through TGF-β/Smads signaling pathway.* International journal of biological sciences, 2012. **8**(10): p. 1310-1322.
74. Kliment, C.R., et al., *A novel method for accurate collagen and biochemical assessment of pulmonary tissue utilizing one animal.* Int J Clin Exp Pathol, 2011. **4**(4): p. 349-55.
75. Quarles, L.D., et al., *Distinct proliferative and differentiated stages of murine MC3T3-E1 cells in culture: An in vitro model of osteoblast development.* Journal of Bone and Mineral Research, 2009. **7**(6): p. 683692.
76. Keira SM, F.L., Gragnani A, Duarte IS, Barbosa J., *Experimental model for collagen estimation in cell culture* Acta Cir Bras, 2004. **19**: p. 17-22.
77. Junqueira, L.C., G. Bignolas, and R.R. Brentani, *Picrosirius staining plus polarization microscopy, a specific method for collagen detection in tissue sections.* Histochem J, 1979. **11**(4): p. 447-55.
78. Tullberg-Reinert, H. and G. Jundt, *In situ measurement of collagen synthesis by human bone cells with a sirius red-based colorimetric microassay: effects of transforming growth factor beta2 and ascorbic acid 2-phosphate.* Histochem Cell Biol, 1999. **112**(4): p. 271-6.

79. Lareu, R.R., et al., *Essential modification of the Sircol Collagen Assay for the accurate quantification of collagen content in complex protein solutions.* Acta Biomaterialia, 2010. **6**(8): p. 3146-3151.
80. Golub, E.E. and K. Boesze-Battaglia, *The role of alkaline phosphatase in mineralization.* Current Opinion in Orthopaedics, 2007. **18**(5): p. 444448.
81. Millan, J.L., *Alkaline Phosphatases.* Purinergic Signalling, 2006. **2**(2): p. 335-341.
82. Hoemann, C.D., H. El-Gabalawy, and M.D. McKee, *In vitro osteogenesis assays: influence of the primary cell source on alkaline phosphatase activity and mineralization.* Pathol Biol (Paris), 2009. **57**(4): p. 318-23.
83. Gregory;, C.A., et al., *An Alizarin red-based assay of mineralization by adherent cells in culture: comparison with cetylpyridinium chloride extraction.* Analytical Biochemistry, 2004. **329**(1): p. 7784.
84. Heather D. VanGuilder, Kent E. Vrana, and W.M. Freeman, *Twenty-five years of quantitative PCR for gene expression analysis.* BioTechniques, 2008. **44**(5): p. 619-626.
85. Michael Keeney, et al., *The ability of a collagen/calcium phosphate scaffold to act as its own vector for gene delivery and to promote bone formation via transfection with VEGF(165).* Biomaterials, 2010. **31**(10): p. 2893-2902.
86. Stephan Pabingera, et al., *A survey of tools for the analysis of quantitative PCR (qPCR) data.* Biomolecular Detection and Quantification, 2014. **1**(1).
87. Barber, R.D., et al., *GAPDH as a housekeeping gene: analysis of GAPDH mRNA expression in a panel of 72 human tissues*. Vol. 21. 2005. 389-395.
88. Hakki, S.S., et al., *Osteogenic differentiation of MC3T3-E1 cells on different titanium surfaces.* Biomedical materials (Bristol, England), 2012. **7**(4): p. 45006.
89. Omar F. Zouani, et al., *Differentiation of pre-osteoblast cells on poly(ethylene terephthalate) grafted with RGD and/or BMPs mimetic peptides.* Biomaterials, 2010. **31**(32): p. 8245-8253.
90. Michael W. Pfaffl, et al., *Determination of stable housekeeping genes, differentially regulated target genes and sample integrity: BestKeeper – Excel-based tool using pair-wise correlations.* Biotechnology Letters, 2004. **26**(6): p. 509515.
91. Alexey Larionov, A. Krause, and W. Miller, *A standard curve based method for relative real time PCR data processing.* BMC Bioinformatics, 2005. **6**(1): p. 62.
92. CR, P., *Fluorescent dyes for lymphocyte migration and proliferation studies.* Immunology and Cell Biology, 1999. **77**(6): p. 9.
93. St-Pierre, J.-P., et al., *Three-dimensional growth of differentiating MC3T3-E1 pre-osteoblasts on porous titanium scaffolds.* Biomaterials, 2005. **26**(35): p. 73197328.
94. Balla, V.K., et al., *Porous tantalum structures for bone implants: fabrication, mechanical and in vitro biological properties.* Acta Biomater, 2010. **6**(8): p. 3349-59.
95. Eckert, K.L., et al., *Preparation and in vivo testing of porous alumina ceramics for cell carrier applications.* Biomaterials, 2000. **21**(1): p. 63-69.
96. Karlsson, M., et al., *Initial in vitro interaction of osteoblasts with nano-porous alumina.* Biomaterials, 2003. **24**(18): p. 3039-3046.
97. Walpole, A.R., et al., *A novel nano-porous alumina biomaterial with potential for loading with bioactive materials.* Journal of biomedical materials research. Part A, 2009. **90**(1): p. 46-54.
98. Kim, H.W., et al., *Bone formation on the apatite-coated zirconia porous scaffolds within a rabbit calvarial defect.* J Biomater Appl, 2008. **22**(6): p. 485-504.
99. Beck, G.R., et al., *Relationship between alkaline phosphatase levels, osteopontin expression, and mineralization in differentiating MC3T3-E1 osteoblasts.* Journal of Cellular Biochemistry, 1998. **68**(2): p. 269-280.
100. Ni, S., et al., *Understanding improved osteoblast behavior on select nanoporous anodic alumina.* International Journal of Nanomedicine, 2014: p. 3325.

101. Roualdes, O., et al., *In vitro and in vivo evaluation of an alumina-zirconia composite for arthroplasty applications.* Biomaterials, 2010. **31**(8): p. 2043-54.
102. Franks, G.V. and Y. Gan, *Charging Behavior at the Alumina–Water Interface and Implications for Ceramic Processing.* Journal of the American Ceramic Society, 2007. **90**(11): p. 3373-3388.
103. Lohmann, C.H., et al., *Ceramic and PMMA particles differentially affect osteoblast phenotype.* Biomaterials, 2002. **23**(8): p. 1855-63.
104. Song, Y.-G. and I.-H. Cho, *Characteristics and osteogenic effect of zirconia porous scaffold coated with β-TCP/HA.* The Journal of Advanced Prosthodontics, 2014. **6**(4): p. 285.
105. Andersen, L.K., et al., *Cell volume increase in murine MC3T3-E1 pre-osteoblasts attaching onto biocompatible tantalum observed by magnetic AC mode atomic force microscopy.* European cells & materials, 2005. **10**: p. 61.
106. Anselme, K., *Osteoblast adhesion on biomaterials.* Biomaterials, 2000. **21**(7): p. 667-681.
107. Xia, L., et al., *Proliferation and osteogenic differentiation of human periodontal ligament cells on akermanite and β-TCP bioceramics.* European cells & materials, 2011. **22**: p. 68.
108. Benzaid, R., et al., *Fracture toughness, strength and slow crack growth in a ceria stabilized zirconia-alumina nanocomposite for medical applications.* Biomaterials, 2008. **29**(27): p. 3636-41.
109. Chevalier, J., et al., *On the kinetics and impact of tetragonal to monoclinic transformation in an alumina/zirconia composite for arthroplasty applications.* Biomaterials, 2009. **30**(29): p. 5279-5282.
110. Kimura, Y., et al., *Initial attachment of human oral keratinocytes cultured on zirconia or titanium.* Dental Materials Journal, 2012. **31**(3): p. 346-353.
111. John P . Fisher , Antonios G . Mikos , and J.D. Bronzino, *Tissue Engineering*. 2007, Florida,USA: CRC Press.
112. Kong, Y.M., et al., *Improvement in biocompatibility of ZrO2-Al2O3 nano-composite by addition of HA.* Biomaterials, 2005. **26**(5): p. 509-17.
113. Afzal, M.A.F., et al., *Functionally graded hydroxyapatite-alumina-zirconia biocomposite: Synergy of toughness and biocompatibility.* Materials Science and Engineering: C, 2012. **32**(5): p. 1164-1173.
114. He, X., et al., *Zirconia toughened alumina ceramic foams for potential bone graft applications: fabrication, bioactivation, and cellular responses.* J Mater Sci Mater Med, 2008. **19**(7): p. 2743-9.
115. Kohal, R.J., et al., *In vitro reaction of human osteoblasts on alumina-toughened zirconia.* Clin Oral Implants Res, 2009. **20**(11): p. 1265-71.
116. Pinnell, S.R., *Regulation of collagen biosynthesis by ascorbic acid: a review.* Yale J Biol Med, 1985. **58**(6): p. 553-559.
117. Miao, X., et al., *Hydroxyapatite coating on porous zirconia.* Materials Science and Engineering: C, 2007.
118. Fabbria, P., et al., *Lifetime estimation of a zirconia–alumina composite for biomedical applications.* Dental Materials, 2013.
119. Byung-Ho, Y., et al., *Aligned porous alumina ceramics with high compressive strengths for bone tissue engineering.* Scripta Materialia, 2008. **58**.
120. Ryan, G., A. Pandit, and D. Apatsidis, *Fabrication methods of porous metals for use in orthopaedic applications.* Biomaterials, 2006. **27**(13): p. 2651-2670.
121. Thibault, R., A. Mikos, and F. Kasper, *Scaffold/Extracellular matrix hybrid constructs for bone-tissue engineering.* Advanced healthcare materials, 2013. **2**(1): p. 13-24.
122. Wirth, C., et al., *Biomaterial surface properties modulate< i> in vitro</i> rat calvaria osteoblasts response: Roughness and or chemistry?* Materials Science and Engineering: C, 2008. **28**(5): p. 990-1001.

123. Murphy, C., M. Haugh, and F. O'Brien, *The effect of mean pore size on cell attachment, proliferation and migration in collagen-glycosaminoglycan scaffolds for bone tissue engineering.* Biomaterials, 2010. **31**(3): p. 461-466.
124. Meyer, U., et al., *Basic reactions of osteoblasts on structured material surfaces.* European cells and materials, 2005. **9**: p. 39-49.
125. Zhou, J. and C.-A. Wang, *Porous yttria-Stabilized Zirconia Ceramics Fabricated by Nonaqueous-Based Gelcasting Process with PMMA Microsphere as Pore-Forming Agent.* Journal of the American Ceramic Society, 2013. **96**(1): p. 266-271.
126. Roy, M.E., et al., *Not all zirconia femoral heads degrade in vivo.* Clinical orthopaedics and related research, 2007. **465**: p. 220-226.
127. Brito-Chaparro, J.A., et al., *Elucidating of the microstructure of ZrO2 ceramics with additions of 1200°C heat treated ultrafine MgO powders: Aging at 1420°C.* Materials Chemistry and Physics, 2007. **106**(1): p. 4553.
128. Rahaman, M.N., et al., *Functionally graded bioactive glass coating on magnesia partially stabilized zirconia (Mg-PSZ) for enhanced biocompatibility.* J Mater Sci Mater Med, 2008. **19**(6): p. 2325-33.
129. Matsuoka, F., et al., *Morphology-Based Prediction of Osteogenic Differentiation Potential of Human Mesenchymal Stem Cells.* PLoS ONE, 2013. **8**(2).
130. Dorst, K., et al., *The Effect of Exogenous Zinc Concentration on the Responsiveness of MC3T3-E1 Pre-Osteoblasts to Surface Microtopography: Part I (Migration).* Materials, 2013. **6**(12).
131. Cho, L.R., et al., *Bone response of Mg ion-implanted clinical implants with the plasma source ion implantation method.* Clinical Oral Implants Research, 2010. **21**(8): p. 848-856.
132. Kim, H.-W., et al., *Porous ZrO2 bone scaffold coated with hydroxyapatite with fluorapatite intermediate layer.* Biomaterials, 2003. **24**(19): p. 3277-3284.
133. Valerio, P., et al., *The effect of ionic products from bioactive glass dissolution on osteoblast proliferation and collagen production.* Biomaterials, 2004. **25**(15): p. 29412948.
134. Ganss, B., R.H. Kim, and J. Sodek, *Bone Sialoprotein.* Critical Reviews in Oral Biology & Medicine, 1999. **10**(1): p. 79-98.
135. Komori, T., *Regulation of osteoblast differentiation by Runx2.* Adv Exp Med Biol, 2010. **658**: p. 43-9.
136. Kim, Y.-J., et al., *Bone Morphogenetic Protein-2-induced Alkaline Phosphatase Expression Is Stimulated by Dlx5 and Repressed by Msx2.* Journal of Biological Chemistry, 2004. **279**(49): p. 50773-50780.
137. Franceshi, R.T. and B.S. Iyer, *Relationship between collagen synthesis and expression of the osteoblast phenotype in MC3T3-E1 cells.* Journal of Bone and Mineral Research, 1992. **7**(2): p. 235246.
138. Nakamura-Ota, M., et al., *A new murine osteoblastic cell line immortalized with the SV40 large T antigen.* Cell and Tissue Banking, 2013. **15**(3): p. 373380.
139. Chernousova, S., et al., *A genetically active nano-calcium phosphate paste for bone substitution, encoding the formation of BMP-7 and VEGF-A.* RSC Advances, 2013. **3**(28): p. 11155.
140. Xiao, G., et al., *Bone Morphogenetic Proteins, Extracellular Matrix, and Mitogen-Activated Protein Kinase Signaling Pathways Are Required for Osteoblast-Specific Gene Expression and Differentiation in MC3T3-E1 Cells.* Journal of Bone and Mineral Research, 2002. **17**(1): p. 101-110.
141. Underwood, E.E., *Quantitative Stereology* Addison-wesley Series in Metallurgy and Materials. 1970: Addison-Wesley Educational Publishers Inc.

142. *Stereometrische Metallographie. von S. A. Saltykov. 1. Auflage, VEB Deutscher Verlag für Grundstoffindustrie, Leipzig 1974, 397 Seiten, 205 Bilder, 63 Tabellen, Ln. 55,— DM.* Materialwissenschaft und Werkstofftechnik, 1975. **6**(6): p. 216.
143. Kozlova, D., et al., *Cell targeting by antibody-functionalized calcium phosphate nanoparticles.* J. Mater. Chem., 2012. **22**: p. 396-404.
144. Klesing, J., S. Chernousova, and M. Epple, *Freeze-dried cationic calcium phosphate nanorods as versatile carriers of nucleic acids (DNA, siRNA).* J. Mater. Chem., 2012. **22**: p. 199-204.
145. Dorozhkin, S.V. and M. Epple, *Biological and medical significance of calcium phosphates.* Angew. Chem. Int. Ed., 2002. **41**: p. 3130-3146.